IKE Institut für Kernenergetik
und Energiesysteme

Temporary Melt Retention in the Reactor Pit of the European Pressurized Water Reactor (EPR)

vorgelegt von

Dipl.-Ing.
Markus Nie

geboren in Münster/Westfalen

Universität Stuttgart

Abstract

The EPR is provided with a core catcher to preserve the integrity of the containment also in case of a postulated severe accident with core melting. The principal conceptual idea behind the core catcher is to spread the melt on a large area located lateral to the reactor pit and to cool it at both, the melt upper and lower surface.

A key element with respect to achieving a coolable melt configuration in the spreading area is the temporary melt retention in the reactor pit. This measure aims to decouple the long-term stabilisation from in-vessel processes, RPV failure mode and corresponding melt discharge as well as associated uncertainties. Its specific objectives are (i) to accumulate the melt in cases of sequential melt releases and (ii) to unify and to condition the spectrum of in-vessel melt characteristics at the time of and for spreading. The temporary melt retention is achieved by layers of sacrificial concrete attached to the sidewalls of the pit and placed on top of the melt gate, through which the melt must erode. Temporary melt retention terminates after the melt contacts and opens the melt gate, which blocks the access to the spreading area.

The principal objective of this work is to provide evidence that the goals of the temporary melt retention can be adequately fulfilled. Given this focus, the MCCI programme COSACO is developed to analyse the interactions between the core melt and sacrificial concrete. The innovative phenomenological approach underlying to COSACO constitutes a coherent description of the mutual dependency between thermal hydraulics and thermochemical phenomena. Modelling of these phenomena employs real solution thermochemistry.

The validation of the program against representative experiments proofs the suitability of the new approach on the basis of adequately reproducing the principal experimental data. Notably, the agreement was obtained without employing additional parameters adjustable to experiments.

The analysis of the temporary melt retention exploits the inherent characteristic of the MCCI pool to establish a coupled system with the bottom structures of the RPV due to exchange of radiant heat. In parallel, the effect of different initial amounts of melt involved in the initial melt pour as well as of the decay heat level is parametrically investigated. The analyses has identified that the ablation front progression is inherently self-regulating, as it adapts to the amount of released melt and to the actual decay heat level. Given these characteristics, it is demonstrated that an effective accumulation of the melting core in the pit is achieved independent of the scenario.

The refractory layer backing the walls of sacrificial concrete and the fixed position of the melt gate constitute a geometrical constraint for melt front progression in sideward and downward direction. This constraint restricts the ablatable amount of concrete as well as the surface/volume ratio of the melt. Thanks to this characteristic, the terminal spectrum of melt compositions and melt states is predicted to be highly unified. At the same time, these states exhibit properties which are well-suited for melt spreading.

Zusammenfassung

Der EPR verfügt über ein Kernschmelzerückhaltesystem zur Gewährleistung der Integrität des Sicherheitsbehälters im Falle eines Kernschmelzunfalls. Das Funktionsprinzip beruht auf einer großflächigen Ausbreitung und beidseitigen Kühlung der Schmelze auf einer seitlich zur Reaktorgrube angeordneten Fläche.

Ein wesentlicher Aspekt zur Erreichung einer kühlbaren Schmelzekonfiguration stellt die zeitlich befristete Rückhaltung der Schmelze in der Reaktorgrube dar. Mit Hilfe dieser Maßnahme soll eine Entkopplung der langfristigen Schmelzestabilisierung von den innerhalb des Reaktordruckbehälters ablaufenden Prozessen einschließlich der Freisetzungscharakteristik der Schmelze sowie den damit verbundenen Unsicherheiten erreicht werden. Die spezifischen Ziele der zeitweiligen Rückhaltung umfassen (i) die Sammlung der sequentiell aus dem Reaktordruckbehälter austretenden Schmelze sowie (ii) die Vereinheitlichung und Konditionierung der Schmelzenzustände im Hinblick auf den Ausbreitvorgang. Die Rückhaltung wird durch auf die Seitenwände der Grube sowie das Schmelztor aufgebrachte Schichten aus Opferbeton erreicht, durch die die Schmelze erodiert. Sie ist beendet, wenn die Schmelze das den Zugang zum Ausbreitraum versperrende Schmelztor kontaktiert und öffnet.

Die Aufgabe dieser Arbeit ist die Nachweisführung der mit der zeitweiligen Rückhaltung verbundenen Ziele. Zu diesem Zweck wurde das Rechenprogramm COSACO zur Simulation der Wechselwirkung zwischen Kernschmelze und Opferbeton entwickelt. Der dem Programm zugrunde liegende innovative Modellierungsansatz beruht auf der Beschreibung der gegenseitigen Abhängigkeit zwischen thermochemischen Phänomenen sowie der Thermohydraulik des Schmelzesees. Die Modellierung der thermochemischen Aspekte berücksichtigt Eigenschaften realer Lösungen.

Die Validierung von COSACO anhand repräsentativer Experimente zeigt gute Ergebnisse und belegt damit die Eignung des innovativen Ansatzes. Dabei ist anzumerken, dass dieses Resultat ohne die Einführung zusätzlicher, an experimentelle Ergebnisse anpassbare Parameter erzielt wurde.

Die Nachweisführung basiert auf einer parametrischen Untersuchung des Einflusses der anfänglich in der Reaktorgrube vorhandenen Schmelzemasse sowie der Nachwärmeleistung. Daneben wird eine wichtige Eigenschaft der zeitweiligen Schmelzenrückhaltung ausgenutzt, nämlich die Bildung eines kohärenten Systems zwischen der Schmelze in der Reaktorgrube und den unteren Strukturen des Reaktordruckbehälters aufgrund von Wärmestrahlung. Es zeigt sich, dass sich die Erosionsgeschwindigkeit selbstregelnd an die Schmelzemenge und die Nachwärmeleistung anpasst. Gemeinsam mit der Ausbildung des kohärenten Systems führt diese Charakteristik dazu, dass das Kernschmelzinventar unabhängig vom Szenario in der Reaktorgrube gesammelt wird.

Hinter dem Opferbeton vorgesehene Schutzschichten sowie das Schmelztor begrenzen die Betonerosion in lateraler Richtung bzw. nach unten und damit die Masse erodierbaren Betons sowie das Oberfläche/Volumen-Verhältnis der Schmelze. Dadurch stellen sich eine Vereinheitlichung der Zusammensetzungen sowie für den Ausbreitvorgang günstige Eigenschaften der Schmelze ein.

Content

Nomenclature

General Notation

a	-	Activity
A	m^2	Surface
c	J/kgK	Specific heat
c_p	J/kgK	Specific heat of a gas at constant pressure
e	J/kg	Specific enthalpy
Δe	J/kg	Change of specific enthalpy due to phase transitions
Δe_{dec}	J/kg	Concrete decomposition enthalpy
Δe_w	J/kg	Heat of evaporation
E	J	Enthalpy
ΔE	J	Change of enthalpy within a time interval
f	-	Fraction (general variable)
g	m/s^2	Gravitional acceleration
G_m^o	J/mol	Molar free enthalpy of a pure substance at standard pressure
G	J	Total free enthalpy
ΔG_m^o	J/mol	Molar free reaction enthalpy at standard pressure
j	m/s	Superficial gas velocity
h	W/m^2K	Heat transfer coefficient
$\bar{h}$	W/m^2K	Serial connection of heat transfer coefficients
k	W/mK	Thermal conductivity
K	-	Equilibrium constant
l	m	Distance, length
L	m	Laplace constant
m	kg	Mass
Δm	kg	Change of mass within a time interval
$\dot{m}$	kg/s	mass flow
$\dot{m}''$	kg/m^2s	Mass flow density
M	kg/mol	Molar weight
MT	-	General notation for metals
MT_xO_y	-	General notation for oxides
n	-	Number of moles
Nu	-	Nusselt-number
p	Pa	Pressure
p_i	Pa	Partial pressure of a component
Pr	-	Prandtl-number
$\dot{q}''$	W/m^2	Heat flux density
$\dot{q}'''$	W/m^3	Volumetric heat source

Q	J	Amount of sensible heat
$\dot{Q}$	W	Heat flux
R_m	J/molK	Ideal gas constant
r	m	Radius
Ra'	-	Internal Raleigh-number
R_1, R_2	-	Dimensionless radius
SF	-	Safety margin
t	s	Time
Δt	s	Time interval
T	K, °C	Temperature
ΔT	K, °C	Temperature difference
U_t	m/s	Terminal bubble rise velocity
V	m^3	Volume
w		Slope
x	-	Generalised variable for melt composition
z_{Cc}	m	Position of the ablation front
z_1, z_2, z_3	-	Viscosity evaluation parameters
α	-	Void fraction
β	1/K	Thermal expansion coefficient
γ	-	Activity coefficient of a mixture component
δ	m	Thickness
ε	-	Emissivity
η	Pas	dynamic viscosity
λ	-	Partition coefficient
μ	m^2/s	kinematic viscosity
ν	-	Stochiometric coefficient
ξ	-	Mass fraction
ρ	kg/m^3	Density
σ_{blz}	W/m^2K^4	Boltzmann-constant
σ	N/m	Surface tension
φ	-	Viewfactor
ψ	-	Molar fraction
ζ	-	Volumetric fraction

Subscripts/Superscripts

°	Standard state
0	Refers to the initial state
add	Refers to FeO and SiO_2
amb	Ambient
AS	Auxilliary Surface
B	Bulk of the melt
boil	Boiling
BT	RPV-Bottom

By	Boundary
Cc	Concrete
cd	Conduction
Cr	Crust
dec	Refers to the decomposing concrete surface
DH	Decay heat
dn	In downward direction
ec	Escape
eq	Equivalent
et	Enter
film	Film boiling
fl	Flat
G	Gas
g	Gaseous State
HR	Heavy reflector
I	Interface
id	Ideal
l	Liquid State
liq	Refers to the liquidus line
M	Refers to the considered melt
m	Molar
Met	Metallic Melt
MG	Melt Gate
mod	Modified
mp	Melting point
mx	Refers to the state of mechanically mixed melts
ND	Node
out	Refers to the conditions at the outer side of the pool boundary
Ox	Oxide component/Oxidic melt
rad	Refers to thermal radiation
rd	In radial direction
res	Residual
RV	Reactor pressure vessel
S	Melt free surface
s	Solid state
sat	State of saturation of water
S-j_{AS}	Between melt free surface and the considered auxiliary surface
S-j_{ND}	Between melt free surface and the considered node of the concrete walls
Sl	Slag
sol	Refers to the solidus line
SP	Lower core support plate
S-RV	Between melt free surface and reactor pressure vessel
su	Slurry

tot	Total
UO_2-ZrO_2	Refers to the UO2-ZrO_2 system
up	In upward direction
V	Vapour
W	Water
xs	Excess
ZrO_2-FeO	Refers to the ZrO_2-FeO system
ZrO_2-SiO_2	Refers to the ZrO_2-SiO_2 system

Indices

i	Component index
h, j	Index for surfaces and corresponding heat fluxes
k	Index for a cooling step
n	Time discretisation
Φ	Phase index

Abbreviations and Names

ACE	**A**dvanced **C**ontainment **E**xperiments
AP 600	**A**dvanced **P**ressurised Water Reactor with 600 MWe
BALI	Experimental programme investigating convection phenomena
BETA	Experiments investigating molten core concrete interactions
BWR	**B**oiling **W**ater **R**eactor
CHEMAPP	Thermochemical equilibrium solver
CIT	**C**orium **I**nteraction and **T**hermochemistry
CORCON	Computer programme for the analyis of molten core concrete interactions
CORESA	Experimental Programme on **Cor**ium Interactions with **Re**fractory and **Sa**crificial layers
CORFLOW	Computer programme for analysing melt spreading
CORIUM	Oxidic melt evolving from melting of the core
COSACO	**C**orium on **Sa**crificial **Co**ncrete
COSCHEM	**COS**ACO **Chem**istry
EPR	**E**uropean **P**ressurised Water **R**eactor
EU	**E**uropean **U**nion
FOREVER	**F**ailure **o**f **Re**actor **Ve**ssel **Re**tention
GEMINI	**G**ibbs **E**nergy **Mini**miser
KATS	**Ka**rlsruher **T**hermit-Schmelzen **S**preading Experimente
LBLOCA	**L**arge **B**reak **Lo**ss of **C**oolant **A**ccident
LCS	**L**imestone **C**ommon **S**and concrete
MAAP	**M**odular **A**ccident **A**nalysis **P**rogram
MACE	**M**elt **A**ttack and **C**oolability **E**xperiments
MCCI	**M**olten **C**ore **C**oncrete **I**nteractions
MELCOR	Computer code for nuclear severe accident source term and risk assessment analyses
PWR	**P**ressurised **W**ater **R**eactor
RPV	**R**eactor **P**ressure **V**essel

SBLOCA	**S**mall **B**reak **Lo**ss of **C**oolant **A**ccident
SCDAP/RELAP	Computer code for analysing overall reactor coolant system response, core damage progression and fission product release during severe accidents
SCRAM	Denotes shut-down of the reactor
SGTE	**S**cientific **G**roup **T**hermodata **E**urope
SURC	Experiments investigating molten core concrete interactions
SWR 1000	**S**iede**w**asser**r**eaktor (Boiling Water Reactor) with 1000 MWe
TDBCR	**T**hermo**d**ynamic **D**atabase **C**orium
WALTER	**Wal**l **Te**mperatu**r**es, code for investigating 1D thermal conduction problems
WECHSL	Computer programme for the analysis of molten core concrete interactions

Chapter 1
Introduction

In the light of global warming and of an energy-hungry world, nuclear power is forecast to continue growing as a clean and reliable contributor to the world energy needs.

However, public acceptance significantly suffered from the accidents of Three Mile Island in 1979 and Chernobyl in 1986. The conclusion from these accidents was, that for new-built plants the radiological consequences of severe accidents must be further reduced and ultimately restricted to the direct ambient of the site to make evacuations unnecessary.

It is evident that such a goal can only be achieved if the long-term integrity of the containment is warranted also for a severe accident involving melting of the core.

In spite of their fairly low probability, events can take place in light water reactors which lead to melting of the core due to the loss of the cooling function of the reactor cooling system in combination with failure of all succeeding emergency measures to reestablish sufficient cooling.

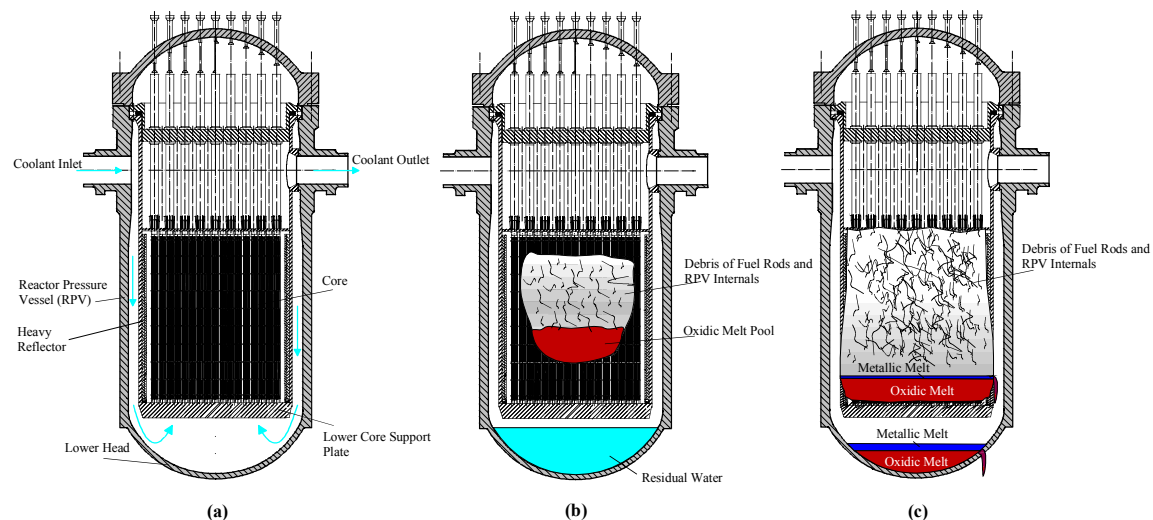

Fig. 1-1: *In-vessel accident progression as assumed for the EPR: (a) intact core, (b) early phase characterised by a partially degraded core, (c) late phase characterised by a completely degraded core, two melt pools and an open lower head*

Once lost, the water left in the RPV starts to evaporate due to the decay heat generated in the core. The steam passing along the fuel rods is insufficient to sustain cooling without reaching conditions that damage the core and ultimately lead to its degradation as sketched in Fig. 1-1.

After reaching a temperature of ~1200°C, the fuel cladding made of zirconium starts to interact highly exothermical with steam and consequently accelerates the originally decay heat-driven heat-up of the core. The products of this reaction are hydrogen and zirconia (ZrO_2). While hydrogen is released into the atmosphere of the containment, ZrO_2 melts and mixes with the melting UO_2 pellets of the fuel and with unoxidised Zr, thus creating a sub-stochiometric oxidic molten pool. Eventually, a temporarily stable pool develops on the lower core support plate due to the heavy reflector which stops further widening of the pool for a limited time. As the heat flux is highest along the vertical boundaries of the pool, the melt penetrates the heavy reflector before the lower support plate fails. Consequently, the entire part of the molten pool located above the breach region relocates into the lower head. Afterwards, the remaining melt gradually relocates as the breach location widens due to continuous melting. Aside from oxides, the relocating melt additionally consists of metals predominantly stemming from the heavy reflector. Following relocation, the melt first quenches in the residual water and then evaporates it. Afterwards, the solidified melt remelts and forms a second pool which attacks the walls of the lower head. Ultimately, the lower head fails and thus opens the path for the melt to discharge into the containment.

If no design measures are implemented, the melt pours onto the concrete basemat and initiates molten core concrete interactions, commonly abbreviated MCCI. The MCCI challenges the integrity of the containment, as the heat-generating melt may completely penetrate through the containment basemat and, in consequence, result in contaminating the soil and ground water underneath. Additionally, the MCCI generates substantial amounts of H_2O as well as of the non-condensable gases CO_2, CO and hydrogen. While H_2O and CO_2 only contribute to pressure build-up in the containment, hydrogen and CO may also form explosive mixtures with the air of the containment atmosphere. The combination of both effects may lead to non-tolerable loads on the containment and thus to a release of significant amounts of radioactivity into the environment.

To effectively prevent interactions between core melt and the concrete basemat, the majority of the advanced light water reactor designs, e.g. Framatome's PWR EPR [Bittermann 2001] and BWR SWR 1000 [Brettschuh 2001] and Westinghouse's advanced PWR AP 600 [IAEA 1995] incorporate specific design measures. The SWR 1000 and AP 600 pursue melt retention and stabilisation in the RPV due to their relatively low power density. In contrast, the EPR incorporates a core catcher located ex-vessel, since the high power density would call any type of in-vessel melt retention into question.

The principal idea behind the EPR core catcher is to spread the molten core on a large area lateral to the RPV. This measure transfers the core melt in a coolable configuration by significantly increasing the surface/volume ratio of the melt. The decay heat is removed by flooding and quenching the melt from the top and at the same time by extracting heat through the bottom via a dedicated cooling structure located underneath the spreading area, see Fig. 1-2.
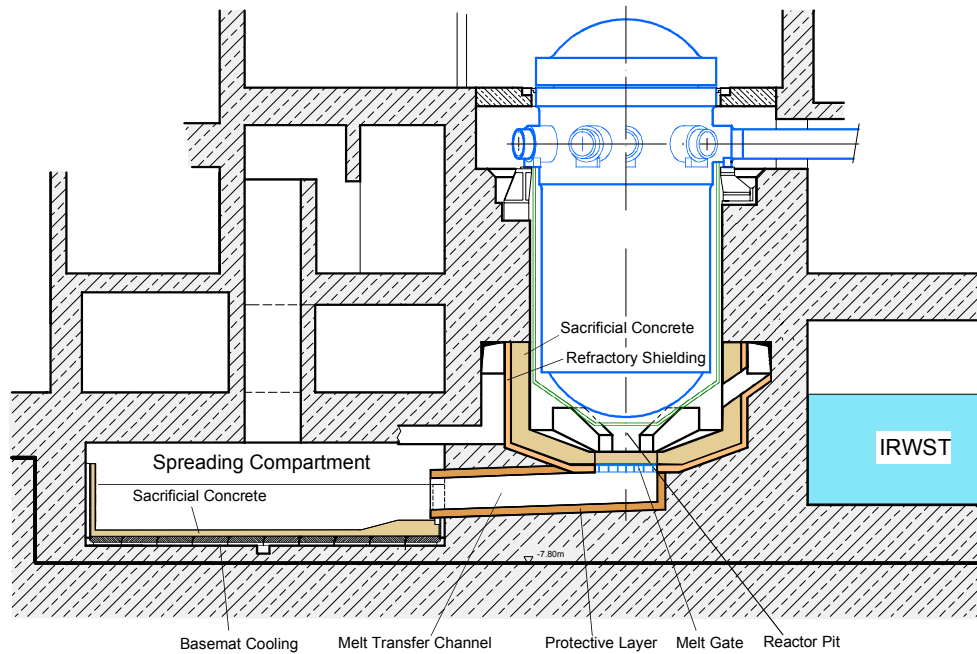
Fig. 1-2: *Cross-section showing the main components of the core catcher of the EPR [Fischer 2003]*

In response to a potential stepwise melt release from the RPV, the overall conceptual approach includes a temporary melt retention in the reactor pit. The objective of this retention is to accumulate the melt inventory before discharging it into the spreading compartment in one event. The retention is achieved by providing a layer of sacrificial concrete through which the melt must erode. It is terminated when the melt contacts and destroys the melt gate, see Fig. 1-2 and, by this, opens the path to the spreading area.

Complete melt accumulation and spreading in one event are of particular importance, since these measures decouple the long-term stabilisation from the inherent uncertainties associated with in-vessel melt formation and the mode of melt release from the RPV. At the same time, the interaction of the melt with the sacrificial concrete is expected (i) to provide melt initial conditions that ensure a successful spreading and (ii) to condense the spectrum of melt states resulting from in-vessel processes into unified melt characteristics at the time of spreading.

Conversely, if the melt was spread into the spreading compartment as it was released from the RPV, the conditions for coolability of the melt would be indeterminate.

The strategy to use concrete as sacrificial material is based on the expectancy that the molten core concrete interactions involve specific phenomena which are essential with respect to fulfilling the goals of the temporary melt retention and to demonstrating its inherently safe operation.

To date, this expectancy predominantly rests on experimental observations and is not yet supported by analytical models that would allow a satisfying transfer of these characteristics to reactor conditions.

This holds true, though, in the past, substantial effort was devoted to the development of MCCI models, i.e. the German computer programme WECHSL [Foit 1995] and the US

programme CORCON [Cole 1984], as a valuable contribution for risk-oriented analyses of severe accidents in operating plants. While focussing on thermal hydraulics, these codes widely neglect the prevailing thermochemical phenomena of the molten pool as well as the mutual dependency of these two aspects.

Therefore, the predictive capability of these codes particularly in terms of MCCI pools involving oxidic melts is limited. In consequence, additional parameters for heat transfer were introduced which are adjustable to individual MCCI experiments. Consequently, reasonable agreement is obtained with those experiments the parameters were adjusted to. On the other hand, the agreement with the results of other tests can diminish if these parameters are left unchanged.

As therefore the existing MCCI codes (i) involve the burden of a proper selection of parameters and (ii) due to this only offer a limited potential to confirm the expected favourable specific characteristics of the MCCI, they were judged inadequate for validating the temporary melt retention in the reactor pit.

The essential step towards a plausible proof of the temporary melt retention is to develop a new MCCI model which consistently takes into account the mutual dependency between the prevailing thermochemical phenomena and the heat transfer characteristics in the molten pool. The principal motivation behind such an approach is to make adjustable parameters obsolete due to adequately describing the phenomenology of the MCCI.

Necessarily, the development of such a new code is accompanied by an extensive testing and validation against representative MCCI experiments involving metallic and, even more important, oxidic melts. This exercise is particularly useful as it helps to demonstrate that the new model is suitable to predict the principal behaviour and thus to identify and quantify the expected inherent characteristics of the MCCI. Additionally, the validation increases the level of confidence when the model is applied to reactor specific conditions.

The validated code is then used to conduct the principal task of this work, namely to provide evidence that the temporary melt retention inherently functions and thus adequately fulfils the goals associated with it.

Chapter 2
Aspects of the temporary melt retention in the reactor pit

2.1 Principal philosophy

The general objective for melt stabilisation is to transfer a core melt from an uncoolable to a coolable state. In terms of the EPR core catcher, this translates into spreading of the melt on a large area located laterally to the pit. Since the oxidic melt generates most of the decay heat, it is the essential object of long-term stabilisation in the spreading area as well as of the preceding chain of processes.

The resulting pan-cake geometry exhibits a surface/volume ratio which allows to remove the decay heat as well as to cool and solidify the melt without exceeding temperatures and heat fluxes critical to the structural components of the core catcher. However, the spectrum of initial physical and thermochemical states of the core melt, e.g. composition and temperature, as well as of melt release sequences from the reactor pressure vessel is deemed to be wide and at the same time, hardly predictable.

In consequence, if the melt was released into the spreading area as it is discharged from the reactor pressure vessel, the conditions for coolability would be indeterminate. In particular, spreadability of the melt would largely depend on the melt characteristics as they evolve from in-vessel processes. Ultimately, spreading would be a matter of chance, given the large spectrum of melt states at the time of vessel failure. Aside from forming significant local inhomogeneities as regards melt distribution, a step-wise and undefined melt release from the RPV and, accordingly, into the spreading compartment, bears the potential of energetic reactions between the in-vessel core melt and water. Water is potentially present in the spreading area since its addition to the melt is passively triggered upon first melt arrival. Additionally, potential blockages formed of already quenched and solidified melt may further disturb the spreading process.

On this basis, it is essential to implement a device on the path from the reactor pressure vessel to the spreading area that eliminates undefined melt release conditions into the spreading compartment and thus enables the proof of long-term melt stabilisation.

Specifically, temporary retention of the melt in the reactor pit constitutes the fundamental approach to set proper initial conditions for achieving a coolable configuration independent of

the uncertainties associated with in-vessel processes and with the melt release mode from the reactor pressure vessel. The principal idea behind this retention is illustrated in Fig. 2.1-1.
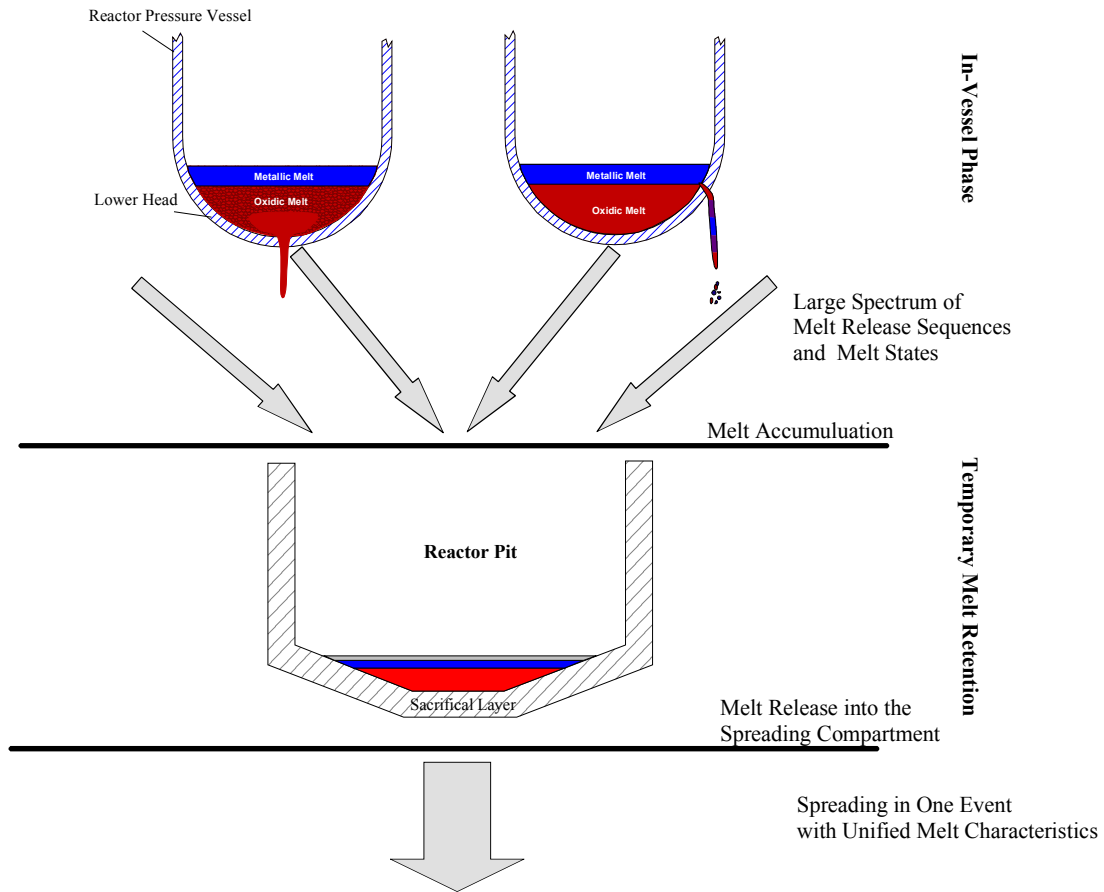

Fig. 2.1-1: *Principle of the temporary melt retention*

One essential objective is to accumulate most of the core melt inventory before its relocation into the spreading compartment. This issue is of particular importance, since it enables spreading of the core melt inventory in one event and consequently establishes the prerequisite for a homogeneous distribution of the melt on the spreading floor.

The temporary melt retention is based on layers of sacrificial material, see Fig. 2.1-1, through which the melt erodes, driven by the decay heat and by the energy released through exothermic reactions between unoxidised core melt components and decomposition products of the sacrificial material. The erosion of the melt through the sacrificial layer provides the time window for melt accumulation. Correspondingly, the sacrificial material must entail sufficient stability.

In parallel to melt accumulation, mixing of sacrificial material with the oxidic melt is expected to generate melt properties that are favourable for melt spreading. In addition, it restricts the spectrum of possible melt compositions and with it, thermophysical and thermochemical melt characteristics at the time of spreading which is instrumental in validating the long-term stabilisation phase.

For condensing the variety of initial melt states into a narrow band at the time of spreading, it is important to oxidise the chemically aggressive metallic core melt components U and Zr, as

their concentration in the initial core melt constitutes a principal uncertainty. Additionally, oxidation rules out the risk of energetic melt/water interactions, when the melt is flooded with water in the spreading compartment.

The sacrificial layer is backed up by a refractory shielding, see Fig. 1-2, to prevent interactions of the melt with the load bearing structural concrete behind, as well as to limit the interactions between the melt and the sacrificial material to a defined geometry. Ultimately, the geometrical constraint effectively restricts the amount of ablatable sacrificial material.

Spreading of the melt takes place after the melt has contacted and destroyed the melt gate which is located underneath the sacrificial concrete in the centre of the bottom of the pit and which blocks the access to the melt transfer channel.

Given the fundamental idea behind temporary melt retention, the following section addresses the selection of the type of sacrificial material as well as the specification of its composition.

2.2 Selection of sacrificial material

2.2.1   Selection of the type of material

Concrete is deemed to be well-suited as sacrificial material on the basis of the following rationale.

Representative experiments employing prototypic, i.e. UO_2/ZrO_2-containing corium, and different types of concrete, e.g. the ACE [Thompson 1997] and MACE [Farmer 1997, Farmer 1999] tests showed that the concrete ablation rate approximately follows the power supply to the melt related to the boundary area of the pool. Further, they indicated that the MCCI favours a homogeneous heat flux distribution along the boundaries of the pool.

Combination of both effects points to self-adjusting characteristics of the MCCI which means that the velocity of the melt front progression into the concrete adjusts to the decay heat level and to the volume/surface ratio of the melt. Applied to the melt retention in the reactor pit, the idea is that for an initially low amount of released melt, the decay heat, the volume/surface ratio of the interacting melt and thus the heat flux and ablation rate are also low. This extends the time window for the inclusion of later pours from the reactor pressure vessel. Conversely, for an initially high amount of released melt, this time window is smaller in accordance with a correspondingly reduced requirement for accumulating the melt.

Additionally, the self-adjusting characteristic correlates the retention time with the time required to accumulate the core melt. In particular, if the first melt pour released into the pit consists of a high fraction of the total inventory, then the period to collect the residual melt is likely shorter than for low fractions. This effect is beneficial for soundly defining the thickness of the sacrificial layer. In contrast, if the system was not self-adjusting, definition of the layer thickness would have to rely on a bounding case which is hardly definable.

The ACE and MACE tests also showed that melt temperatures, if so, only modestly declined during the duration of the test which suggests that the MCCI involves a low melt viscosity and thus establishes adequate conditions for melt spreading.

Remarkably, all above-mentioned experiments used various types of concrete having highly different concrete compositions, e.g. siliceous concrete vs. limestone concrete. This indicates that the outlined experimentally observed phenomena arise independently of which concrete composition is used. Transferred to the EPR, this provides a large flexibility as regards incorporating suitable additives in the sacrificial material. Conversely, a concrete composition that deviates from the specified one would not endanger the objectives of the temporary melt retention.

Additionally, the MCCI effectively mixes the concrete decomposition products with the melt due to the stirring effect induced by the gas release arising from concrete decomposition.

On the other hand, the gas generation by MCCI constitutes an additional source for mass and energy release into the containment and thus has to be considered for the design of measures that mitigate containment loads. Consequently, the selection of the concrete must also consider this issue, in addition to those concerning melt accumulation and melt conditioning.

2.2.2   Definition of the concrete composition

The composition of the sacrificial concrete employed in the reactor pit is specifically selected to meet the requirements of the temporary melt retention. The concrete aggregates dominantly consist of Fe_2O_3 and SiO_2 in approximately equal proportion and are provided in their natural modification form as iron ore and siliceous pebble. 15 wt% of common Portland cement in the dry concrete mixture serve as a binder.

Fe_2O_3 favourably contributes to oxidising the chemically aggressive metals Zr and U in the sub-stochiometric oxidic melt. The reaction by-product Fe does not affect the thermo-chemical characteristics of the metallic melt. In addition, after the dissolved metal inventory in the oxide depletes, surplus Fe_2O_3 accumulates as $FeO_{x,\ x\geq 1}$ in the oxide melt, thus reducing the liquidus temperature and correspondingly, the temperature level at which the MCCI takes place. This effect is beneficial for melt relocation into the spreading compartment, as it diminishes radiant heat losses and thus cooling of the melt during the spreading process. Further, it contributes to reducing the fission product release from the MCCI pool.

The main objective of siliceous pebble is to increase the stability of the concrete.

As the aggregates are applied in their natural modification form, impurities such as $MgCO_3$ (magnesite) and $CaCO_3$ (limestone) are introduced into the concrete system. These components constitute a source for the release of CO_2 during the MCCI. However, as can be deduced from the composition given in Tab. 2.2-1, the CO_2 content in the sacrificial concrete only amounts to ~1.7 wt%, while ordinary siliceous concrete, see Tab. 3.3-2, contains ~3 wt%.

Portland cement was given the preference over alumina-based refractory cement, as it only binds 25 wt% of water referred to the dry cement mass compared to 50 wt% for the other variant. Hardening tests with the described composition have shown that a steady state water content of less than 5 wt% results after a drying time of 150 days, see Fig. 2.2-1. This content is also below the 6 wt% bound in the siliceous concrete used in the BETA tests.
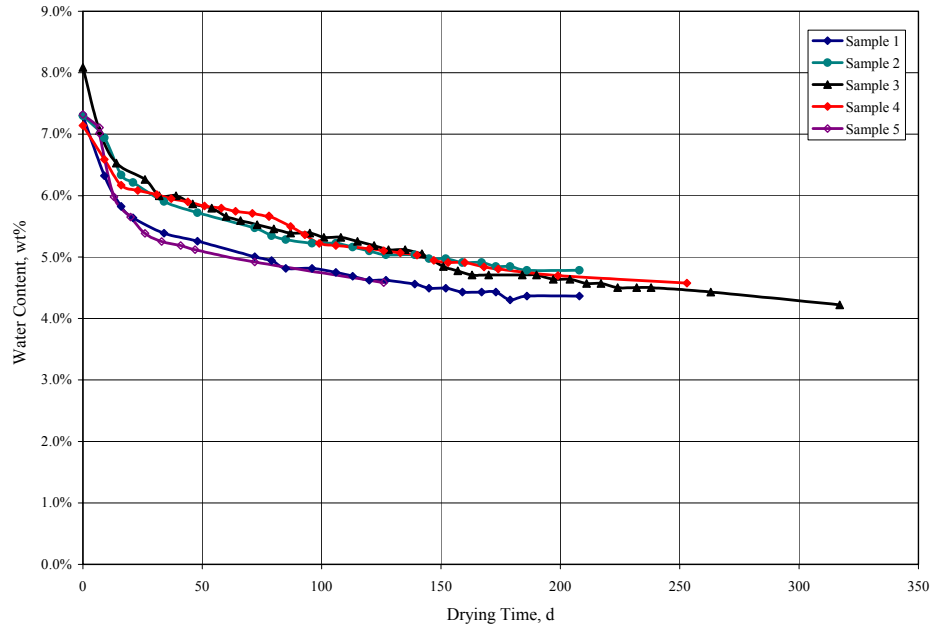
Fig. 2.2-1: *Water content in the sacrificial concrete as a function of drying time for various concrete samples. The samples have the same initial composition.*

Assuming a water content of 5 wt%, the chemical composition is,

Component	wt%
Fe_2O_3	35.3
SiO_2	42.9
Al_2O_3	3.8
CaO	11.1
MgO	0.2
CO_2	1.7
H_2O	5

Tab. 2.2-1: *Chemical composition of sacrificial concrete*

Given the definition of the objectives of the temporary melt retention and the selection of sacrificial material, the next step is to develop a model to appropriately predict the interaction between the core melt and sacrificial concrete.

Chapter 3
Development of the computer code COSACO to analyse Molten Core Concrete Interactions

3.1 Motivation

In the past, substantial effort was devoted to modelling molten core concrete interactions as an important contribution to quantify and to evaluate the radiological release into the environment as a consequence of a core melt accident in existing plants.

This effort resulted in the MCCI codes WECHSL and CORCON. The modelling incorporated in both codes relies on the fundamental assumption that the MCCI pool is almost exclusively a thermal hydraulic system. In contrast, the modelling of thermochemical aspects mostly concentrated on the fission product release from the melt pool. Thermochemical phenomena which influence the behaviour of the molten pool were not or only addressed in a fairly simplified, frequently debatable manner. Aside from chemical reactions, this is particularly true regarding modelling of solidification of the relevant oxidic melt. At the same time, these phenomena are widely decoupled from thermal hydraulic aspects.

On the basis of this thermal hydraulic approach, sophisticated models were developed to predict the heat transfer at the melt/concrete boundary. WECHSL e.g. uses a model based on the assumption that a gas-film may evolve at the interface formed by the concrete decomposition gases which results in similar heat transfer characteristics as film-boiling.

Although metallic and oxidic melts greatly differ in terms of their thermochemical characteristics, the thermal hydraulic approach is used independently of what type of melt interacts with the concrete.

In consequence, due to the model's principal characteristic not to take into account the fundamental differences of the melt thermochemical properties, a similar behaviour of the MCCI is obtained for either type of melt. This especially concerns melt temperature. Specifically, also for oxidic melts a transient cool-down as a typical characteristic of MCCIs involving metallic melts is predicted. This prediction contradicts to the results of relevant MCCI experiments, i.e. of the ACE and of the MACE experimental programme which show fairly constant melt temperatures throughout the test duration. Additionally, the calculated transient cool-down results in a substantial overprediction of ablation front progression.

Hence, additional parameters for heat transfer were introduced to improve the prediction of melt temperature and of ablation front progression, see [Foit 1995a]. These parameters are adaptable to individual MCCI experiments.

Therefore, agreement with experiments to which they are adapted improves. Nevertheless, they still show only limited ability to predict the general phenomenology of oxidic melts observed in the tests, namely not to cool down transiently. Instead, the parameters only retard cooling due to diminishing the heat transfer through the thermal boundary layer which e.g. in WECHSL is assumed to be the main contributor to the overall thermal resistance from the bulk of the melt to the concrete.

Further, test-specific adjustment implies that the prediction of other experiments regarding both, temperature evolution and progression of concrete erosion can diminish, if these parameters are left unchanged.

On that grounds, the existing codes were deemed to be inadequate for validating the temporary melt retention in the reactor pit due to (i) the large uncertainties involved in choosing the parameters, and (ii) due to their limited ability to adequately predict the principal phenomenology of MCCIs involving oxidic melts.

Contrary to the existing models, the fundamental requirement on COSACO is to adequately reproduce this phenomenology without relying on adjustable parameters.

This requirement is a prerequisite to quantify and to extrapolate the expected inherent characteristics of the MCCI with oxide melts to reactor conditions which would strongly support the plausibility of the temporary melt retention.

3.2 General approach

The experience gained from using the existing models as well as from experimental observations suggests that modelling of MCCI involving oxide melts cannot solely rest on thermal hydraulic considerations.

This leads to the idea that phenomena exist inside the melt which effectively limit heat transfer from the bulk of the melt to the pool boundaries already at high temperatures and thus only allow removing approximately the decay heat generated in the melt. In particular, heat removal from the melt is assumed to be governed by internal thermal resistances, while the influence of external resistances is less pronounced. These internal resistances are assumed to arise from depositing refractory core melt components as crusts at the cold boundaries of the pool and, to a lesser extent, from viscosity increase due to formation of solid particles in the volume of the melt. The formation of the solid phases at the boundaries and in the volume is assumed to be governed by the thermochemical behaviour of the multi-component melt in combination with the thermal hydraulic characteristics of the melt pool.

The thermochemical behaviour comprises chemical reactions in as well as the solidification characteristics of the melt. Chemical reactions contribute to the energy balance as a heat source or sink, dependent on whether the reactions are exo- or endothermic. Additionally, they change the melt composition and consequently affect the solidification behaviour. This in turn significantly influences the heat transfer characteristics within the melt.

The fundamentally new philosophy pursued in COSACO addresses this mutual dependence using a consistent modelling of thermal hydraulics and thermochemistry, with the objective to avoid free and thus adaptable parameters.

In terms of metallic melts, the effect of internal heat resistances is less pronounced. Instead, it is assumed that due to the highly effective heat transfer from the bulk of the melt to the concrete interface, the ability of the concrete to absorb the heat delivered from the melt, or, more generally, the thermal resistance at the outer boundary of the pool, mainly limits the heat removal from the melt. Therefore, metallic melts cool down transiently, the extent of which is governed by the conditions at the outer boundary.

For both, the oxidic and metallic melt, thermochemistry is consistently linked with the energy balance and with the pool thermal hydraulics. As a result, a consistent thermochemical state including melt temperature, melt composition and repartition of melt components on solid and liquid phases is obtained.

The general thermodynamic approach to model the time-dependent evolution of the MCCI bases on the assumption of a quasi-steady state. The term quasi-steady implies the idea that the boundary conditions of the system only allow a relatively slow change of state so that the system attains equilibrium at any discrete time. Following this idea, the time-dependent evolution can be approximated by a series of equilibrium states. The relevance behind this approach is that it enables the combined use of phase diagrams, heat transfer coefficients, and chemical equilibrium to predict the extent of chemical reactions. The approach intrinsically neglects the kinetics of chemical reactions. Neglecting this aspect is, however, adequate, since the assumption of equilibrium forms a conservative upper limit for the chemical transformations. Incidentally, validation of COSACO against representative experiments also constitutes a test for the suitability of that approach.

The following sections describe the specific aspects to consistently represent the MCCI, as well as general issues. While the first predominantly relate to phenomena that occur inside the melt, the latter concerns the characteristics at the outer periphery of the pool. These are e.g. concrete decomposition, heat transfer at the outer pool boundaries as well as representation of the geometry. Though the description generally evolves from the specific to the general aspects, an introduction into the characteristics of concrete decomposition is given first in Chap. 3.3. Chap. 3.4 highlights the important thermochemical characteristics and the corresponding modelling. These characteristics are not discussed isolatedly but it is attempted to foreshadow their implications on the representation of the melt pool and corresponding mass transfer, c.f. Chap. 3.5, as well as on the heat transfer within the MCCI pool as discussed in Chap. 3.6. Conversely, aspects described in Chap. 3.5 and 3.6 take advantage of those of Chap. 3.4 which reflects their mutual dependency. Chap. 3.7 concludes the COSACO development with modelling of heat transfer at the melt free surface, melt volume increase due to gases sparging through the pool, representation of the geometry as well as modelling of thermophysical properties of the melt. Chap. 3.8 briefly describes the main characteristics of COSACO including information on the required input data as well as on the output.

3.3 Modelling of concrete ablation

3.3.1 General aspects

Concrete is generally fabricated of cement, aggregates and water. Cement essentially consists of CaO, Al_2O_3, SiO_2 and to a negligible portion of MgO and Fe_2O_3 which is <1wt%. The proportion between the dominant components CaO and Al_2O_3 classifies the cement and determines its field of application. Ordinary Portland-cement as used for construction-type applications and as envisaged for the sacrificial concrete, contains about 65 wt% CaO and 10 wt% Al_2O_3, see Tab. 3.3-1.

In contrast, the concentration of Al_2O_3 in refractory cements, e.g. SECAR 71 [Lafarge 2001] as commonly used for the fabrication of blast furnace liners may exceed 70 wt%, whereas the CaO content is only ~27 wt%. For both types of cement, SiO_2 complements the composition.

Component	Portland Cement, wt% [Wülfrath 2000]	Refractory Cement (SECAR 71, Lafarge), wt%
SiO_2	22.2	0.35
Al_2O_3	10.3	71
CaO	63.44	27
Fe_2O_3	2.0	0.1
TiO_2	0.18	0.25
MgO	0.33	0.5
Others	1.55	0.8

Tab. 3.3-1: *Composition of Portland cement and of Refractory cement*

Portland cement chemically binds ~25% of water referred to its own mass which may rise to ~50% for refractory cement. The contact between water and cement components results in the formation of hydraulic phases, which is an exothermic reaction. The most important phases that arise through these reactions are $Ca(OH)_2$ and $Al_2O_3 \cdot 3H_2O$. These phases govern the hardening process as well as the final strength of the concrete. In addition to the water bound in hydraulic bonds, hardened concrete also stores free water in the pores. Further, a fraction of CaO in the cement may take up atmospheric CO_2 to form $CaCO_3$. However, this formation reaction is considered to be negligible, given the large surplus of water in the initial, wet concrete mixture.

The aggregates influence strength and density and consist of material found in the ambient of the construction site. Commonly, either limestone (mainly $CaCO_3$) or siliceous gravel (mainly SiO_2) is used for common construction concrete [Schäffler 1986]. These aggregates usually contain impurities. In particular, limestone is frequently accompanied by magnesite ($MgCO_3$), whereas siliceous gravel mostly involves magnesite and limestone. The extent of impurities greatly depends on the mine from which the raw material is exploited. E.g. aggregates commonly denoted as limestone may contain up to ~45 wt% magnesite.

In the course of an MCCI, the concrete may interact with oxidic and metallic melts. As soon as the melt comes into contact with concrete, the concrete starts to decompose and to erode. It is evident that the decomposition of concrete is a highly complex process due to the

concrete's inhomogeneous constitution. Prime contributors to concrete decomposition are endothermic degradation reactions, which lead to a successive destabilisation of the concrete structure. These reactions play a dominant role for the decomposition of hardened cement and involve the evaporation of free water at ~100°C, the degradation of the so-called Portlandite $(Ca(OH)_2)$ to CaO and H_2O between 450°C and 550°C, and, to a minor extent at a temperature level of ~800°C, the decarbonisation of the limestone fraction in the cement. The decarbonisation of limestone also occurs in the aggregates. If the aggregates consist to a large part of limestone, this reaction has a considerable influence on the release of CO_2. In this context, it is worth noting that limestone concrete releases ~40wt% of its weight as CO_2 [Roche 1994]. In contrast, siliceous concrete typically liberates 5wt% as CO_2. This relatively small fraction is attributed to lime impurities in the siliceous aggregate. Additionally, the decomposition of limestone is highly endothermic and thus increases the integral energy necessary to decompose concrete with growing limestone content.

Melting of concrete components takes place in the range from ~1100°C to ~1600°C which is essentially dependent on the type of aggregates and the chemical and phase composition. Peehs [Peehs 1979] indicates an effective melting temperature, the so-called concrete decomposition temperature, of about 1300°C for siliceous concrete and 1400°C for the more refractory limestone concrete. The energy required for heating the concrete from ambient temperature to decomposition temperature is called decomposition enthalpy [Peehs 1979]. Given this definition, the decomposition enthalpy inherently includes all energetic transformations arising during the heat-up of concrete up to its decomposition.

The decomposition enthalpy is a valuable property to model concrete ablation rate for a quasi-steady ablation front progression which is induced by the low thermal conductivity of the concrete. In particular, this low conductivity results in almost the same velocity of the ablation front and temperature front. Thus, the concrete temperature behind the ablating surface remains at ambient temperature. This has been confirmed by numerous MCCI experiments, e.g. the SURC-4 test [Copus 1989], where thermocouples embedded in the concrete basemat showed a response almost coincident with the arrival of the melt front. Therefore, the conduction heat transfer from the ablation front into the concrete can be neglected. This yields the following equations for modelling the concrete ablation rate.

An energy balance at the ablating surface gives

$$\dot{m}''_{Cc}\Delta e_{dec} = \dot{q}''_{dec} \tag{3.3-1}$$

where the decomposition enthalpy is of the form,

$$\Delta e_{dec} = e_{Cc}\big|_{T=T_{dec}} - e_{Cc}\big|_{T=T_{amb}} \tag{3.3-2}$$

and the convection heat flux from the melt bulk to the concrete surface is,

$$\dot{q}''_{dec} = \bar{h}_{dec}\left(T_B - T_{dec}\right) \tag{3.3-3}$$

The ablation velocity is given by,

$$\frac{dz_{Cc}}{dt} = \frac{\dot{q}''_{dec}}{\rho_{Cc}\Delta e_{Dec}} \tag{3.3-4}$$

While the next chapter deals with modelling of decomposition enthalpy and decomposition temperature, the model for determining the overall heat transfer coefficient at the melt/concrete interface, $\overline{h}_{dec}$, is outlined in Chap. 3.6 following an introduction into the thermochemical characteristics of the melt pool. This is due to the high relevance of thermochemistry as regards this issue.

Thermochemical considerations also play an important role for modelling concrete decomposition enthalpy and temperature, as the melting behaviour of the concrete is obtained from thermochemical calculations. However, an in-depth thermochemical understanding is not considered to be crucial for this task. Therefore, modelling of these concrete parameters is already outlined in the following chapter.

3.3.2 Prediction of concrete decomposition temperature and –enthalpy

3.3.2.1   General

Experiments investigating decomposition temperature and enthalpy were only conducted for few construction-type concretes employed at selected reference plants. Consequently, there exists a lack of corresponding data for both, concretes used in other existing plants as well as the sacrificial concrete envisaged for the EPR. Additionally, the decomposition and melting characteristics of the individual concretes significantly depend on the type of cement in combination with the specific characteristics of the aggregate. The latter is a function of composition which varies with the mine from which the material is exploited. Thus, the uncertainties involved in applying the existing experimental values even to concretes of similar composition can be significant. However, all the concrete types can definitely not be analysed experimentally with respect to decomposition enthalpy and temperature. At the same time, there is no model available to predict these properties.

Therefore, the focus of this chapter is devoted to modelling these properties for a number of different concrete types involving all relevant concrete components. Examination of the melting behaviour of the concrete using thermochemistry involving modelling of real-solution effects as outlined in Chap. 3.4.4 builds the general framework for this model. This approach enables to predict the melting behaviour of concrete systems for almost arbitrary compositions. The modelling and its validation is outlined employing the relatively well-investigated types of siliceous concrete as used in e.g. some BETA tests [Alsmeyer 1992] and the MACE M4 experiment [Farmer 1999] and of limestone common *s*and (LCS) concrete as used in e.g. the MACE 3b test [Farmer 1997].

The model development involves two essential steps.

Firstly, the composition of the hardened concrete at room temperature is estimated and the respective concrete specific enthalpy, i.e. the second term on the right side of Eq. 3.3-2 is determined. The estimate factors in the type of cement and its respective characteristics, as well as the water content and composition of the aggregates.

Secondly, an analysis of the concrete melting behaviour employing thermochemical equilibrium calculations is conducted to determine the concrete decomposition temperature. The respective specific enthalpy to finally predict the decomposition enthalpy according to

Eq. 3.3-2 is determined using complementing equilibrium calculations involving gaseous and condensed phases.

3.3.2.2 Composition and specific enthalpy of hardened concrete

In terms of hydrate phases, it is assumed that Al_2O_3 and CaO form the hydrate phases $Ca(OH)_2$ and $Al_2O_3 \cdot 3H_2O$ by exothermic chemical reactions.

Provided that enough water is present and intimately mixed with the cement components to transform all CaO and Al_2O_3 present in the cement into hydrate phases, Portland cement as given in Tab. 3.3-1 theoretically binds ~25.8% water referred to the dry cement weight. Assuming that the aggregates remain chemically unaffected during the hardening process, the degree to bind water is solely determined by the cement content in the concrete mixture.

Component/wt%	Siliceous Concrete	LCS concrete	Heat of formation [kJ/kg]
$Ca(OH)_2$	11.92	12.79	-13322
$Al_2O_3.3H_2O$	2.40	2.4	-16593
$CaCO_3$	6.48	30.83	-12066
$MgCO_3$	0.68	16.48	-13000
Fe_2O_3	1.7	1.7	-5146
CaO	0	0	-11339
SiO_2	70.0	29.28	-15180
MgO	0.0	2.08	-14917
Al_2O_3	3.2	2.03	-16424
Water (free)	3.62	2.41	-15880
Specific enthalpy of hardened concrete (kJ/kg)	-14656.0	-13511.0	

Tab. 3.3-2: *Estimated composition of hardened concrete and corresponding heat of formation*

Tab. 3.3-2 lists the predicted composition of siliceous and of Limestone Common Sand (LCS) concrete, the heat of formation of the individual components and the concrete specific enthalpy. The hardened composition is obtained using the composition of Portland cement given in Tab. 3.3-1 in combination with the chemical compositions of the concretes given in the test reports, see [Firnhaber 1992] for siliceous concrete and [Farmer 1997] for LCS concrete. The specific enthalpy of hardened concrete at room temperature is deduced from the heat of formation of the individual compounds weighed by their respective mass fractions in the hardened concrete.

3.3.2.3 Decomposition temperature and decomposition enthalpy

The main difficulty involved in determining the decomposition enthalpy is to predict the decomposition temperature. The methodology to address this issue is adopted from the immobilisation criterion for viscosity-limited melt spreading based on the melt volumetric solid fraction.

Specifically, it is assumed that the immobilisation criterion developed for viscosity-limited spreading also applies to predict the onset of concrete ablation. In this context, ablation relates to melting of concrete at the melt/concrete interface. Given a sufficiently low viscosity as a

result of melting, the melted concrete slag detaches from the solid concrete underneath and buoys up into the melt.

The immobilisation criterion employs the volumetric solid fraction as a function of temperature to determine a threshold value at which the modelled viscosity approaches infinity. Consequently, the melt immobilises if the volumetric solid fraction approaches this threshold. Transferred to modelling concrete ablation, the volumetric fraction must fall short of such threshold value to enable the concrete to ablate.

A number of authors, e.g. [Marsh 1980] report that spreading stops if the volumetric solid fraction in the melt approaches ~50%. Strictly, this value only applies to spherical particles which do not interact chemically with the ambient liquid phase. It may also vary with the type of melt and the cooling rate during the spreading transient. However, the subsequent analysis employs the 50% criterion, given the good experience gained from post-test calculations of the KATS spreading experiments with the CORFLOW code [Wittmaack 2002] utilising this value [Eppinger 2001].

The basis for predicting the volumetric solid fraction is formed by thermochemical equilibrium calculations employing the real-solution thermochemical database COSCHEM of COSACO, see Chap. 3.4.4.3. These calculations yield the solid and liquid phase compositions as a function of temperature, from which the volumetric solid fraction is finally obtained by inversely averaging the densities of the individual solid and liquid phase densities by weight,

$$\zeta_s = \frac{\dfrac{m_s}{\rho_s}}{\dfrac{m_l}{\rho_l} + \dfrac{m_s}{\rho_s}} \qquad (3.3\text{-}5)$$

Fig. 3.3-1 relates the volumetric solid fraction with the corresponding decomposition enthalpy as a function of temperature for both, siliceous and LCS concrete. The decomposition enthalpy has been obtained from Eq. 3.3-2, where the concrete specific enthalpy at decomposition temperature has been determined using the results of the thermochemical analysis and the respective specific enthalpies of the individual components, i.e.

$$e_{Cc}\big|_{T=T_{dec}} = \sum_{i_s} \xi_{i_s} e_{i_s}(T_{dec}) + \sum_{i_l} \xi_{i_l} e_{i_l}(T_{dec}) + \sum_{i_g} \xi_{i_g} e_{i_g}(T_{dec}) \qquad (3.3\text{-}6)$$

As Fig. 3.3-1 indicates, LCS concrete melts gradually, whereas siliceous concrete exhibits an almost isothermal drop of solid fraction from 95 % to 60 %. This effect is attributed to the quite different compositions. LCS concrete involves significantly lower fractions of relatively low melting components, i.e. SiO_2, than siliceous concrete. On the other hand, it contains a larger amount of higher melting components, i.e. CaO and Al_2O_3. Since, according to the rule of thumb, the concrete components melt sequentially corresponding to the relative position of their melting points, it is obvious that concretes which rather consist of low-melting oxides exhibit a relatively steep decline of solid fraction already at the solidus temperature.
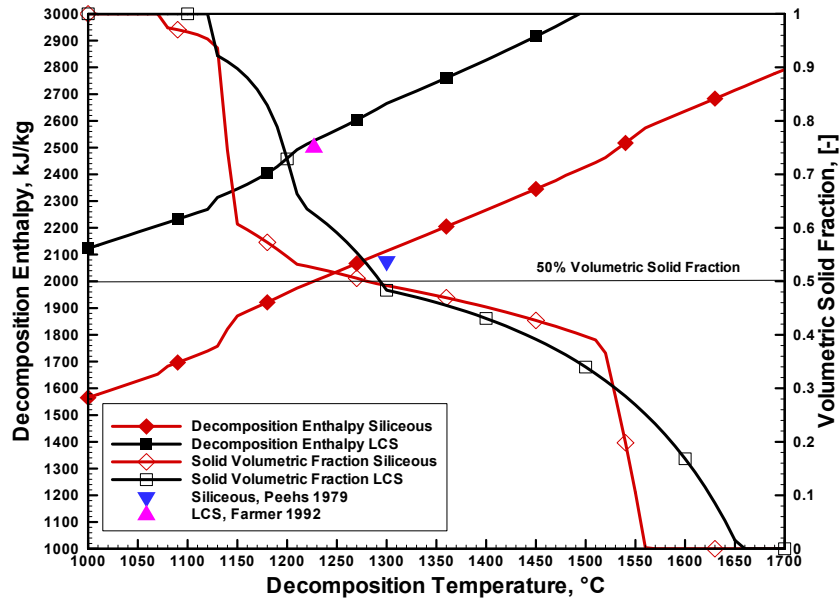
Fig. 3.3-1: *Volumetric solid fraction and decomposition enthalpy of siliceous and limestone common sand concrete*

The model predicts a decomposition temperature for siliceous concrete of 1295°C which is well in line with the experimental value of ~1300°C reported by [Peehs 1979]. The predicted decomposition enthalpy of 2100 kJ/kg also favourably agrees with the value of 2075 kJ/kg indicated by Peehs. The solidus temperature is ~1080°C and the liquidus temperature amounts to 1560°C.

LCS concrete has a predicted decomposition temperature of 1300°C and a decomposition enthalpy of 2670 kJ/kg. These values are also fairly consistent with the data commonly assumed for post-test examinations of MCCI tests. In particular, a decomposition temperature and enthalpy of ~1227°C and 2500 kJ/kg, respectively was employed in MACE [Farmer 1992] to conduct the energy balance based on the experimentally obtained ablation front progression.

The differences between the decomposition enthalpy of both concretes are attributed to the content of $CaCO_3$ and $MgCO_3$ and to the related thermochemical effects.

In summary, the prediction of decomposition enthalpy and temperature is in reasonable agreement with the existing data. On this basis, this model can be extrapolated to other construction concretes as well as to the sacrificial concrete of the EPR with a sufficient level of confidence.

As regards sacrificial concrete, the chemical composition given in Tab. 2.2-1 establishes the basis for determining the composition of the hardened state at room temperature. Tab. 3.3-3 lists the result.

Component	wt%
$Ca(OH)_2$	12.2
$Al_2O_3.3H_2O$	2.4
$CaCO_3$	3.32
$MgCO_3$	0.44
Fe_2O_3	35.3
SiO_2	42.9
Al_2O_3	2.24
H_2O (free)	1.2
Specific enthalpy of hardened concrete (kJ/kg)	-11360

Tab. 3.3-3: *Composition and specific enthalpy of sacrificial concrete in the hardened state*

Given this composition, the concrete decomposition temperature and corresponding decomposition enthalpy are determined utilising the model described above. Fig. 3.3-2 relates the volumetric solid fraction with the corresponding decomposition enthalpy.
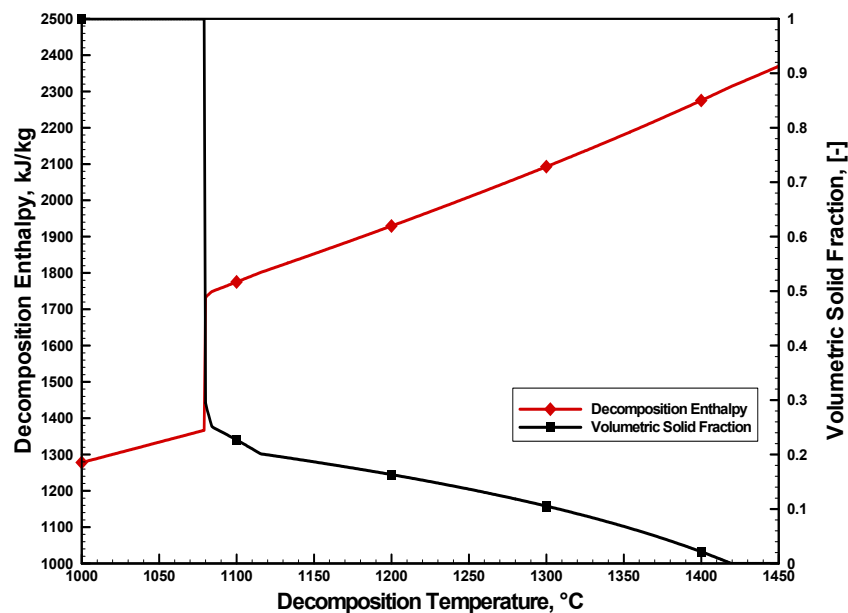
Fig. 3.3-2: *Volumetric solid fraction and decomposition enthalpy vs. temperature of the sacrificial concrete*

According to Fig. 3.3-2, the sacrificial concrete exhibits an isothermal drop of solid fraction from 100% to ~30% at the predicted solidus temperature of ~1080°C. This behaviour contrasts with that of the investigated conventional concretes. These showed a relatively continuous decline over the entire melting range. The difference is attributed to the high content of low melting concrete oxides, i.e. SiO_2 and particularly Fe_2O_3 which in combination lead to a significant formation of liquid phases already at the solidus temperature.

Therefore, melting of sacrificial concrete is similar to the melting of a single component solid. Due to the isothermal change of phase, the decomposition enthalpy of 1730 kJ/kg corresponds to the low bound of solid fraction of 30%.

3.4 Assessment of thermochemical characteristics of the MCCI and corresponding modelling

3.4.1 Introduction

An essential aspect of the consistent approach to model MCCI is to appropriately reflect the thermochemical behaviour of the melt pool. The core melt, as it evolves from in-vessel processes and is released into the reactor pit, consists of several components that embody fairly different characteristics. To a first approximation, they can be classified into metals and oxides. The group of metals essentially comprises Fe, Cr, Ni and Zr, where Fe, Cr and Ni predominantly stem from structural in-vessel components, e.g. the heavy reflector, the lower core support plate, and the lower head, while Zr comes from fuel rod cladding. The principal oxides are UO_2 from the fuel and ZrO_2 resulting from fuel cladding oxidation. Except Zr which shows a very high solubility also in the oxidic $(U,Zr)O_2$ system [Farmer 1999a] and thus results in forming sub-stochiometric $(U,Zr)O_{2-x}$ melts, metals and oxides are considered to be almost immiscible. In consequence, the two groups form a molten pool consisting of stratified metal and oxide layers, where the denser oxide layer is located underneath the metal layer.

When this melt is poured into the reactor pit and the MCCI starts, it undergoes a permanent change in composition due to mixing with concrete decomposition products. This process increases the mass of the melt and at the same time also the number of melt components.

Metallic components, e.g. metallic Zr, are oxidised by some of the oxidic concrete components. Depending on the reactants involved, the chemical reactions are either exothermic or endothermic and thus contribute to the energy balance as heat source or heat sink. Exothermic reactions which preferably involve metallic Zr/U, augment the concrete erosion rate, whereas endothermic reactions result in a decrease. In addition, H_2 and CO arising from a reduction of the gaseous decomposition products H_2O and CO_2 by metallic melt components, are released into the containment.

In case of oxide melts, concrete decomposition products do not only give rise to chemical reactions but also dissolve in the oxidic melt due to their oxidic character. The continuous dissolution decreases the liquidus and solidus temperature and at the same time widens the temperature difference between these temperatures. Above the liquidus or below the solidus temperature, the melt is either completely liquid or solid; in the solidification regime bound by these temperatures, liquid and solid phases coexist. The solidification regime may increase from ~10-20 °C for the binary UO_2-ZrO_2 melt to more than 1000 °C when the concrete concentration in the melt becomes significant, see Fig. 3.4-7.

Solidification of the oxide starts upon initiation of the MCCI. In the further course, it is affected by the decay power and the change of the melt's liquidus and solidus temperature due to sustained mixing with concrete decomposition products. It involves a variety of phenomena, among which the most important ones are (i) the formation of solid phases as a function of temperature and composition and (ii) the distribution of the melt components on the coexisting solid and liquid phases. Both phenomena have a considerable effect on the heat

transfer in the molten pool, cf. Chap. 3.6, and ultimately govern the temperature level at which the MCCI takes place.

Additionally, dissolution of concrete in the oxide melt significantly influences important thermophysical properties, e.g. viscosity and density.

In contrast, given the almost complete immiscibility of the metal melt with concrete oxides, the solidification regime of the metal melt is only affected by metallic reaction by-products, such as Si which arise from the reduction of concrete components. For metal melts as they develop during an MCCI, the solidification regime is, in general, more than one order of magnitude smaller and much less affected than that of the oxide melt.

Chap. 3.4.2 and 3.4.3 provide a thorough examination of the relevant thermochemical phenomena. This essentially concerns chemical reactions as well as the solidification behaviour of the oxide melt. The examination is based on an approximate modelling which also reflects the history of the COSACO development.

Chap. 3.4.4 then describes the implementation of thermochemical modelling addressing the prevailing real solution behaviour of the considered multi-component melts. This approach establishes an advanced representation of the thermochemical behaviour of complex core melts.

3.4.2 Chemical reactions in the MCCI pool

Chemical reactions are of significance for modelling the MCCI, since they contribute to the MCCI as an additional heat source or sink which in turn influences the concrete ablation rate. Equally important, they affect melt composition which determines the solidification behaviour and which in terms of the EPR is a relevant parameter for examining melt unification and conditioning at the time of spreading.

Following this motivation, this chapter systematically discusses condensed phase reactions and heterogeneous reactions in the MCCI system for both, metallic and oxidic melts. These chemical reactions take place (i) between condensed, i.e. liquid or solid metallic and oxidic components and (ii) between metals and the gaseous concrete decomposition products H_2O and CO_2.

Some of the metallic melt components exhibit a strong affinity for oxygen and, since they take up oxygen from almost every oxygen source, tend to a complete oxidation. On the contrary, other components are relatively stable and thus are hardly oxidisable. The same holds true for oxides, where in the absence of reducing metals some oxides decompose at a certain temperature threshold while others maintain their state even in the presence of strongly reducing components.

The first task at hand is to examine the stability of the relevant MCCI oxides in the presence of reducing metals and, given this precondition, to formulate condensed phase reactions. The second task is to evaluate the reactions between the gaseous concrete decomposition products and metals. Aside from formulating chemical reactions, the motivation behind these tasks is to establish a ranking scheme which is obeyed by the reactions.

The basic idea to assess the potential for condensed phase reactions is to evaluate the stability of melt components towards each other. The free reaction enthalpy for a formation reaction of an oxidic compound from its respective components constitutes the principal parameter for this evaluation. This stochiometric, heterogeneous reaction involves *one* mole O_2 as well as the appropriate amount of the metal educt which then form the oxide [Frohberg 1994]. The reference to one mole of oxygen instead of to one mole of oxide has been chosen to facilitate the comparison of the free enthalpy of formation of the relevant MCCI oxides in the Richardson diagram, Fig. 3.4-1. After this diagram is constructed using Eqs. 3.4-1 to 3.4-11 [Frohberg 1994], it serves to deduce a characteristic reaction hierarchy for the MCCI system.

The equations below also allow to estimate the molten pool composition in chemical equilibrium, given the specific chemical reactions involved in the MCCI plus the corresponding equilibrium constants.

The molar free reaction enthalpy $\Delta G^o_{M,R}$ for a heterogeneous reaction involving metal ('MT') and oxygen as reactants,

$$n_{Met}MT + \left(n_{O_2} = 1\right)O_2 \rightarrow n_{Ox}MT_xO_y \tag{3.4-1}$$

is evaluated from

$$\Delta G^o_m = |\nu_{Ox}|G^o_{MT_xO_y} - |\nu_{Met}|G^o_{m,MT} - |\nu_{O_2} = -1| \cdot G^o_{m,O_2} = \sum_i \nu_i G^o_{m,i} \tag{3.4-2}$$

where $G^o_{m,i}$ is the molar free enthalpy of the pure substance at reference pressure for a given temperature. In this context, a heterogeneous reaction denotes a chemical reaction, for which at least one component on the reactant or product side is gaseous and one component has a condensed aggregate state. Notably, the stochiometric coefficients ν in Eq. 3.4-2 are negative for substances on the educt side of Eq. 3.4-1, whereas they are positive for substances on the product side.

The equilibrium constants of the individual chemical reactions form the basis to estimate the composition of the MCCI pool. Principally, the equilibrium constant is defined by the mass action law and provides information about the degree to which the reaction proceeds. This degree and thus, the stability of the forming oxide increases with an increasing equilibrium constant. For a reaction of the type as given in Eq. 3.4-1, the mass action law yields the following form of the equilibrium constant,

$$K = \frac{\left(a_{MT_xO_y}\right)^{n_{Ox}}}{\left(a_{O_2}\right)^1 \left(a_{MT}\right)^{n_{Met}}} \tag{3.4-3}$$

or, more generally

$$K = \prod_i a_i^{\nu_i} \tag{3.4-4}$$

Additionally, K is linked with the free reaction enthalpy by the following exponential function,

$$K = e^{-\Delta G^o_m/R_mT} \tag{3.4-5}$$

The activities a_i of Eq. 3.4-4 are given by the product of the activity coefficient γ_i with the molar fraction of the ith component,

$$a_i = \gamma_i \psi_i \qquad (3.4\text{-}6)$$

where

$$\psi_i = \frac{n_i}{\sum_i n_i} \qquad (3.4\text{-}7)$$

As indicated by Eq. 3.4-6, the activity can be considered as an effective concentration, while the molar fraction constitutes the true concentration. Accordingly, the activity coefficient yields the deviation of the real from ideal behaviour of thermochemical mixtures which in the following are also denoted as solutions. For modelling ideal solutions and pure substances, as considered for the present considerations, the activity coefficient is equal to one. In contrast, modelling of real solutions requires activity coefficients which are generally different from one and which can be determined experimentally.

The molar fraction ψ_i is evaluated from the amount of the ith component, referring to the amount of the specific phase of which the ith component is a component, see Eq. 3.4-7.

Thus, given the assumption that the condensed educts and products, i.e. the oxidic and the metallic components of Eq. 3.4-1, exist separately as so-called pure oxidic and metallic substances, the molar fractions and corresponding activities of these components, a_{MT} and $a_{MT_xO_y}$ are equal to one.

The gas phase generally consists of all melt components, including gaseous metals and oxides plus potentially inert gases from the ambient atmosphere. Assuming the gas phase as an ideal mixture, the activity of oxygen in this phase equals its molar concentration,

$$a_{O_2} = \psi_{O_2} \qquad (3.4\text{-}8)$$

Since the molar concentration is proportional to the partial pressure, the equilibrium constant given in Eq. 3.4-3 can be ultimately transformed to

$$K = \frac{p^o}{p_{O_2}} \qquad (3.4\text{-}9)$$

If more than one gaseous component participates in the heterogeneous reaction, K has the form

$$K = \prod_i \left(\frac{p_i}{p^o} \right)^{\nu_i} \qquad (3.4\text{-}10)$$

where the reference pressure p^o is frequently taken as 1 bar. Inserting Eq. 3.4-5 into Eq. 3.4-9 yields the governing equation to evaluate the stability of the oxide melt components [Frohberg 1994],

$$\Delta G_m^0 = -R_m T \ln \frac{p^o}{p_{O_2}} \qquad (3.4\text{-}11)$$

where the free reaction enthalpy is evaluated using Eq. 3.4-2. According to this relation, the partial oxygen pressure decreases with decreasing free reaction enthalpy for a given temperature. Clearly, the oxide is the more stable, the more negative the free reaction enthalpy is.

To examine the stability of the oxidic melt components, according to Eq. 3.4-11, Fig. 3.4-1 compares ΔG_m^0 as a function of temperature for the relevant oxidic melt components in the so-called Richardson diagram.

The diagram indicates that CaO is the most stable and NiO the least stable oxide. CaO is not reduced by any metal, whose oxide is less stable. Therefore, elemental Ca receives
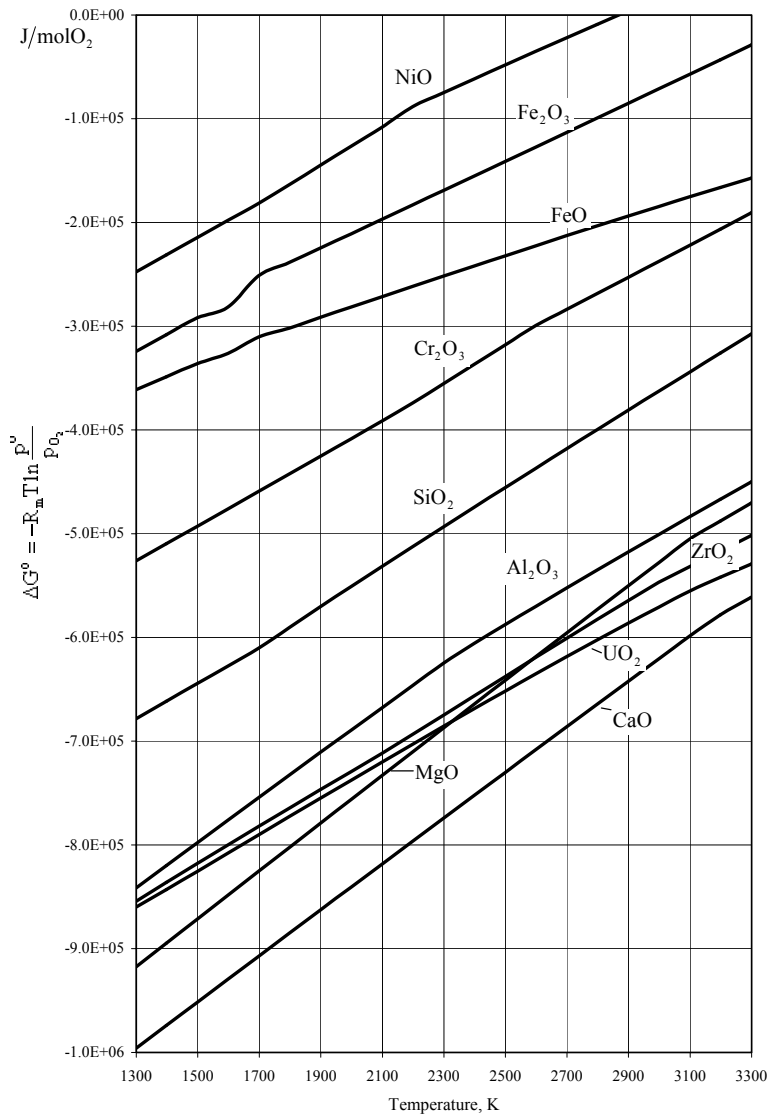
Fig. 3.4-1: *Richardson-diagram for the relevant oxides involved in the MCCI. The underlying Gibbs-enthalpies were taken from the SGTE database for pure substances [Dinsdale 1991]*

oxygen from all oxides given in this diagram. Conversely, all metals are oxidised by NiO, but Ni is not oxidised at all. This ranking already forms the basis for the reaction hierarchy. Ca
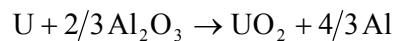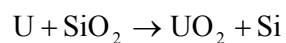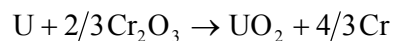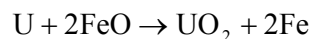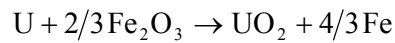
would be oxidised first and Fe oxidation takes place only after all other elements are oxidised. However, since Ca is not a component of the initial core melt, and since there exists no mechanism to form it, oxidation of Ca is only hypothetical.

The stability of MgO falls below that of UO_2 above ~2350 K and below that of ZrO_2 above ~2600 K. Thus, MgO is reduced by uranium and by zirconium above these temperatures. However, since the stability of MgO is fairly similar to that of the core oxides UO_2 and ZrO_2 and it additionally constitutes only a minor fraction of the concrete decomposition products, possible reactions involving MgO and Mg are neglected. A source for formation of Al is the reduction of Al_2O_3 by Zr and U, respectively.
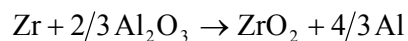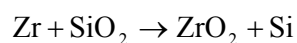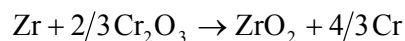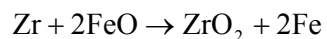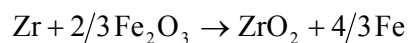
Since UO_2 is slightly more stable than ZrO_2 over the entire temperature interval, the first order oxidation sequence of the metals is U>Zr>Al>Si>Cr>Fe. The stability criterion also determines the reaction order of the oxides that oxidise the metals. In particular, U and Zr are oxidised by Fe_2O_3, FeO, Cr_2O_3, SiO_2 and Al_2O_3 in the given order. Since UO_2 and ZrO_2 have almost the same stability towards each other, a reduction of ZrO_2 by U is neglected.

Al is oxidised by Fe_2O_3, FeO, Cr_2O_3 and SiO_2. Si reacts with Fe_2O_3, FeO, and Cr_2O_3. Cr is only oxidised by Fe_2O_3 and FeO. The weakest oxygen reducing agent Fe forms FeO in the presence of Fe_2O_3. Given the identification of potential reaction partners, the following gross-reactions involving condensed phases are formulated.
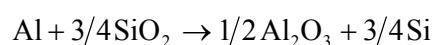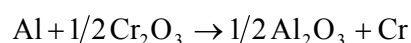
a) *Reactions with uranium*

$$U + 2/3\,Fe_2O_3 \rightarrow UO_2 + 4/3\,Fe$$

$$U + 2\,FeO \rightarrow UO_2 + 2\,Fe$$

$$U + 2/3\,Cr_2O_3 \rightarrow UO_2 + 4/3\,Cr$$

$$U + SiO_2 \rightarrow UO_2 + Si$$

$$U + 2/3\,Al_2O_3 \rightarrow UO_2 + 4/3\,Al$$

b) *Reactions with zirconium*

$$Zr + 2/3\,Fe_2O_3 \rightarrow ZrO_2 + 4/3\,Fe$$

$$Zr + 2\,FeO \rightarrow ZrO_2 + 2\,Fe$$

$$Zr + 2/3\,Cr_2O_3 \rightarrow ZrO_2 + 4/3\,Cr$$

$$Zr + SiO_2 \rightarrow ZrO_2 + Si$$

$$Zr + 2/3\,Al_2O_3 \rightarrow ZrO_2 + 4/3\,Al$$

c) *Reactions with aluminium*

$$Al + 1/2\,Fe_2O_3 \rightarrow 1/2\,Al_2O_3 + Fe$$

$$Al + 3/2\,FeO \rightarrow 1/2\,Al_2O_3 + 3/2\,Fe$$

$$Al + 1/2\,Cr_2O_3 \rightarrow 1/2\,Al_2O_3 + Cr$$

$$Al + 3/4\,SiO_2 \rightarrow 1/2\,Al_2O_3 + 3/4\,Si$$
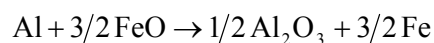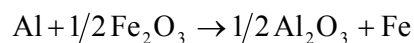
d)   *Reactions with silicon*

$$Si + 2/3\,Fe_2O_3 \rightarrow SiO_2 + 4/3\,Fe$$

$$Si + 2\,FeO \rightarrow SiO_2 + 2\,Fe$$

$$Si + 2/3\,Cr_2O_3 \rightarrow SiO_2 + 4/3\,Cr$$
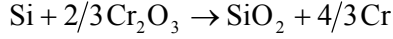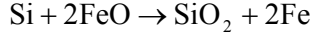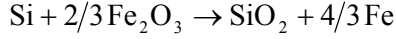
e)   *Reactions with chromium*

$$Cr + 1/2\,Fe_2O_3 \rightarrow 1/2\,Cr_2O_3 + Fe$$

$$Cr + 3/2\,FeO \rightarrow 1/2\,Cr_2O_3 + 3/2\,Fe$$
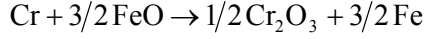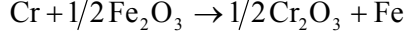
f)   *Reactions with iron*

$$Fe + Fe_2O_3 \rightarrow 3FeO$$
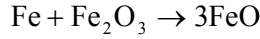
Finally, the potential for reactions of metals with the gaseous concrete decomposition products CO_2 and H_2O remains to be assessed.

In general, metals undergo an oxidation by H_2O or CO_2 of the form [Frohberg 1994],

$$MT + n_G H_2O \leftrightarrow n_{Ox} MT_x O_y + n_G H_2 \tag{3.4-12}$$

$$MT + n_G CO_2 \leftrightarrow n_{Ox} MT_x O_y + n_G CO \tag{3.4-13}$$

For these kinds of heterogeneous reactions, the equilibrium constant is also represented by Eqs. (3.4-2)-(3.4-11). Given the relation between the partial and total pressure,

$$p_i = \psi_i p_{tot} \tag{3.4-14}$$

and the assumption that condensed educts and products exist separately as pure phases, the equilibrium constant can be written as the mole ratio of the educt and product gases,

$$\frac{\psi_{H_2}}{\psi_{H_2O}} = \sqrt[n_g]{e^{-\Delta G_m^o / R_m T}} \quad \text{and} \quad \frac{\psi_{CO}}{\psi_{CO_2}} = \sqrt[n_g]{e^{-\Delta G_m^o / R_m T}} \tag{3.4-15}$$

where the free reaction enthalpy of Eq. 3.4-15 is determined corresponding to the considered reaction. If this ratio is $\gg 1$, the equilibrium is completely on the product side, whereas for a ratio $\ll 1$ almost no oxidation takes place. Eq. 3.4-15 has been evaluated for potential oxidation reactions involving U, Zr, Si, Cr, Fe, Ni and H_2O and CO_2 as a function of temperature. The underlying Gibbs enthalpies of the pure substances to determine ΔG_m^o according to Eq. 3.4-2 were taken from the SGTE-database [Dinsdale 1991]. The results are depicted in Figs. 3.4-2 and 3.4-3.
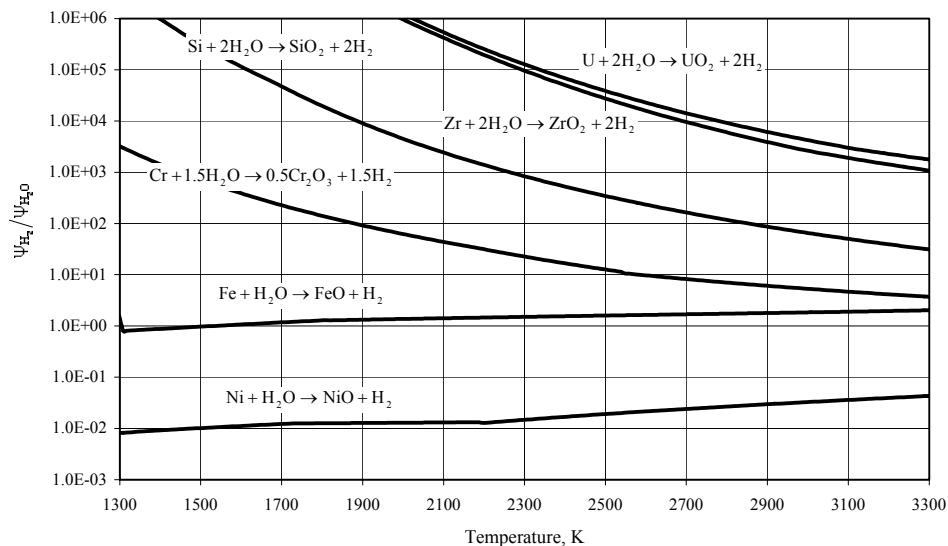
Fig: 3.4-2: *Ratio of equilibrium mole fractions H_2-H_2O vs. temperature for the principal metallic components*
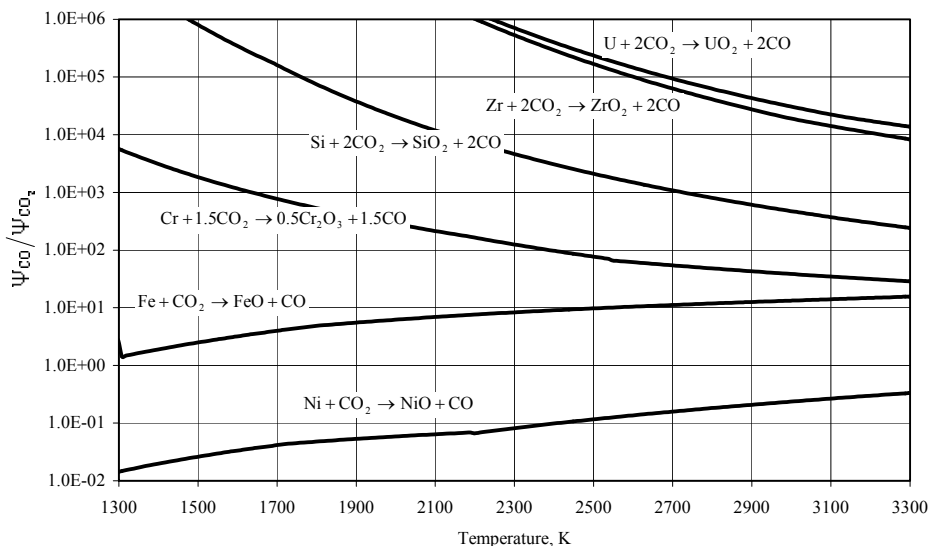
Fig: 3.4-3: *Ratio of equilibrium mole fractions CO-CO_2 vs. temperature for the principal metallic components*

Both figures indicate a high degree of reduction of the reactant gases, except for reactions involving Ni. Even for the reaction of Fe with H_2O or CO_2, this ratio -over a wide temperature range- is larger than two. This indicates a reduction of about 2/3 of the initial amount of H_2O and CO_2, respectively. For Ni, the ratio is always less than one. This means that chemical equilibrium is on the reactant side. Moreover, since Ni appears only as a minor alloy component in conjunction with Cr and since the predominant metal component is Fe, oxidation of Ni by H_2O or CO_2 can be neglected.

Given this analysis, the list of gross reaction equations a) - f) can be extended by heterogeneous reactions as presented in Fig. 3.4-2 and Fig. 3.4-3, neglecting Ni oxidation reactions.

For the purpose of completeness, a reaction hierarchy is also introduced among the gaseous components. This is accomplished by comparing the concentration ratios H_2/H_2O and CO/CO_2 given in Figs. 3.4-2 and 3.4-3. Since this ratio is higher for all heterogeneous reactions involving CO_2, it is considered to be the stronger oxygen provider.

The results of above analyses are summarised in the following ranking scheme for the entire set of considered reactions.
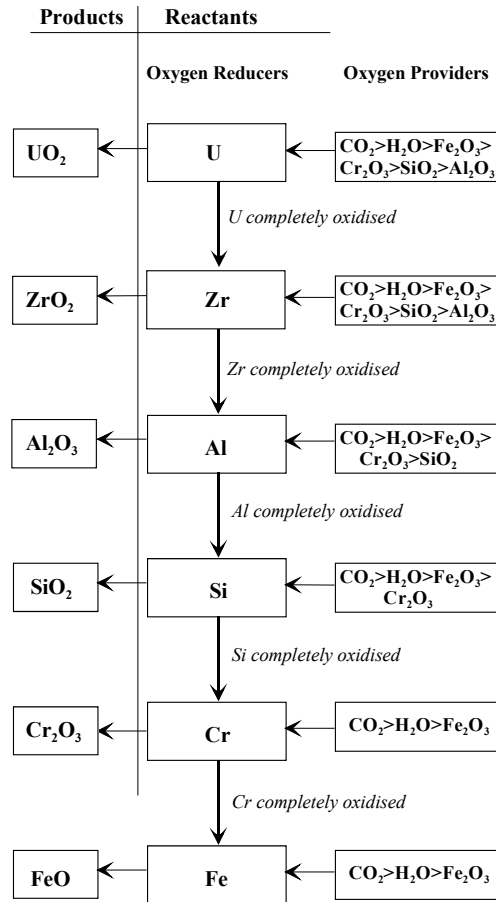
Fig. 3.4-4: *Hierarchy of chemical reactions for corium melts*

The reaction hierarchy is independent of the temperature level at which the chemical interactions take place. This follows from an assessment of the Richardson-diagram which indicates stability conditions between the oxides of interest independent of temperature.

The melt composition can be obtained from that model by determining the equilibrium composition for each chemical reaction individually according to the above hierarchy.

This requires to calculate for each reaction individually the equilibrium constant resulting from equating Eq. 3.4-4 with Eq. 3.4-5, where the free reaction enthalpy is determined according to the stochiometry of the considered reaction. Given the individual equilibrium constants, the melt composition is obtained from sequentially calculating the compositions resulting from the respective reactions. In particular, the initial composition of the melt is used to determine the change of composition induced by the first chemical reaction based on the formulation of an appropriate molar balance. The melt composition as it evolves from this

reaction is then used as an initial condition for the molar balance of the following reaction. This process is repeated until all above reactions are considered.

As is evident from this ranking, the presence of uranium and zirconium prevents the build-up of the essential decomposition products iron oxide and silica in the oxide melt. They only accumulate after these metallic components are depleted.

Given the mechanisms that determine melt composition, the next section deals with the effect of melt composition on the solidification characteristics of corium-concrete mixtures.

3.4.3 Solidification behaviour of oxidic corium melts

3.4.3.1 General

For obtaining a consistent description of the MCCI, the characteristics of solidification of oxidic melts have significant implications on the modelling of heat transfer and, consequently, on establishing the mass- and energy balance.

As will be assumed in Chap. 3.6.2, the formation of refractory crusts at the heat-absorbing boundaries of the melt establishes the dominant thermal resistance for heat removal from the melt.

The following assessment is used to identify the prevailing solidification characteristics of oxidic corium/concrete mixtures and to justify that the solid phases deposited as crusts can be assumed to be in thermochemical equilibrium with the rest of the melt. This means that the solid phases are considered in the mass and energy balance for the molten pool at any stage of solidification, or more generally, at any stage of the MCCI.

Characterisation of the solidification behaviour includes two tasks, (i) to identify the characteristics of solidification of corium/concrete mixtures for bounding solidification mechanisms followed by (ii) estimating the solidus and liquidus lines of the oxide melt as a function of the concrete content in the melt. These lines define the solidification regime and constitute the essential parameters to characterise the solidification behaviour.

3.4.3.2 Enveloping solidification mechanisms

Multi-component melts as oxidic corium solidify within the limits set by (i) equilibrium solidification and by (ii) solidification that follows the path proposed by Scheil [Scheil 1942]. These limits are useful because they represent the two extremes observed in practice [Dantzig 1999].

The underlying condition for *equilibrium solidification*, see .e.g. [Flemings 1974], is that the process is slow enough to attain thermochemical equilibrium of the *entire* solid-liquid mixture. The condition is also met if mass transport by diffusion within the solid and liquid phase that levels out differences in concentration is infinitely high.

The path typical to equilibrium solidification is depicted in Fig. 3.4-5 for a subsequent cool-down of the melt along a line of *constant* composition. The composition variable x can either attain the dimension of molar fraction or mass fraction, therefore the following considerations always refer to the corresponding dimensions. As Fig. 3.4-5 indicates, a decrease of

temperature below the liquidus line to T_1 results in the precipitation of a solid phase with the composition x_{sol1}. The coexisting liquid phase attains the composition x_{liq1}. Accordingly, further cooling to T_2 yields the compositions x_{sol2} and x_{liq2} for the solid and liquid phase, respectively. The solid fraction f_s in the melt is obtained by the lever rule,

$$f_s = \frac{x_{liq} - x_0}{x_{liq} - x_{sol}} \qquad (3.4-16)$$

Additionally, for a given temperature, the solid and liquid compositions are combined by the partition coefficient,

$$\lambda = \frac{x_{sol}}{x_{liq}} \qquad (3.4-17)$$
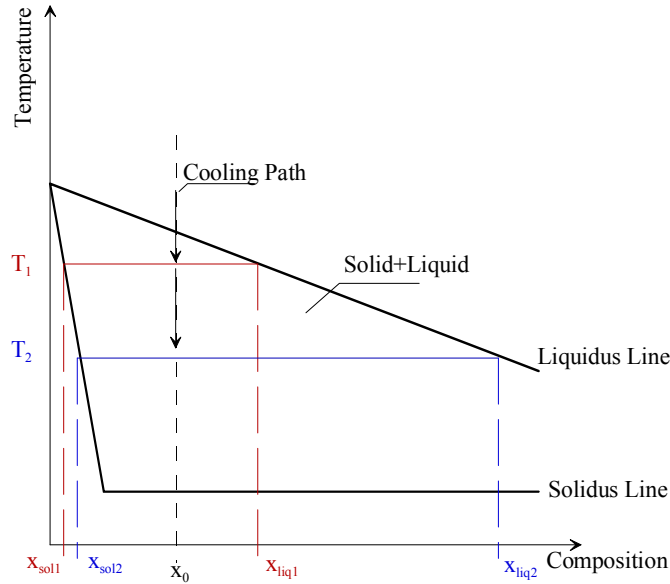
Fig. 3.4-5: *Illustration of equilibrium solidification. X_0 is the initial composition subjected to cooling*

When the liquidus and solidus are straight lines as sketched in Fig. 3.4-5, the partition coefficient becomes independent of temperature. As regards the phase diagram sketched in Fig.3.4-5, for both T_1 and T_2 the resulting ratios x_{sol1}/x_{liq1} and x_{sol2}/x_{liq2} are identical. For many systems, the coefficient has a value less than unity which is equivalent with solidus and liquidus lines sloping downward.

Combination of Eqs. 3.4-16 and 3.4-17 yields the governing equation for equilibrium solidification,

$$x_{sol} = \frac{\lambda x_0}{f_s(\lambda - 1) + 1} \qquad (3.4-18)$$

To recall, equilibrium solidification assumes infinite diffusion in both, the liquid and the solid phase. However, in terms of the MCCI, mass transport and corresponding mixing in the liquid is primarily by bubble-driven convection and thus quite fast, while mass transport in the solid

phase is attributed to diffusion which in contrast is a slow process. Hence, employing equilibrium solidification is a-priori inappropriate to model melt solidification.

Therefore, it is important to examine the Scheil-model describing the second limiting mechanism. This model adequately describes conventional casting processes.

The principal assumption is that diffusion rates are infinitely high in the liquid and zero in the solid. In addition, assuming that λ is a constant, i.e. the solidus and liquidus are straight lines, the Scheil equation is of the form,

$$x_{sol} = \lambda x_0 (1 - f_s)^{\lambda - 1} \tag{3.4-19}$$

Given a stepwise cooling, this means that the solid phases precipitating in each cooling step neither change their composition during further cooling nor interact with the residual liquid phase.

Thus, in practice, during each cooling step only the *residual liquid* is considered for determining the conditions for solidification relevant to the following step. Solid phases are removed from the thermochemical system after every step. In contrast, in the case of equilibrium solidification, the solid fraction is always part of the thermochemical system.
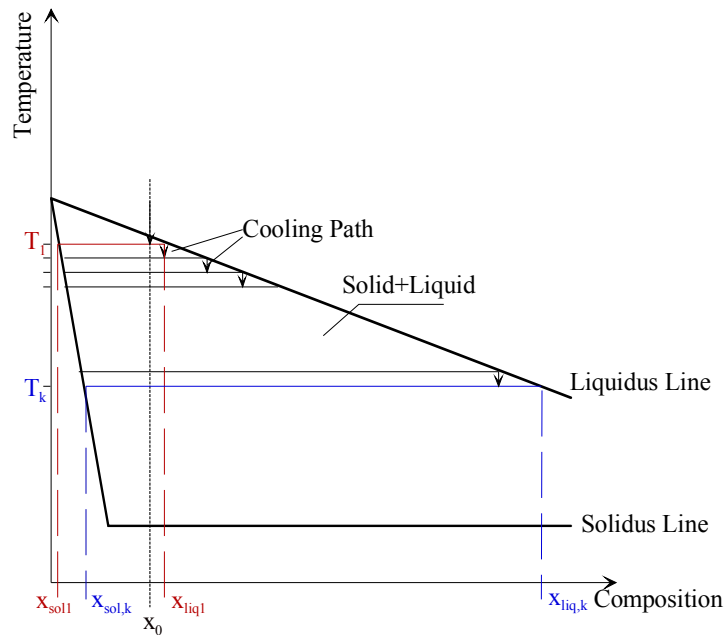
Fig. 3.4-6: *Illustration of melt solidification according to Scheil. X_0 is the initial composition subjected to cooling*

Fig. 3.4-6 depicts the solidification path typical of the Scheil model. Unlike equilibrium solidification, the cooling path does not follow the line of initial composition, x_0, but is along the liquidus line.

A comparison between Eq. 3.4-18 and 3.4-19 reveals that both equations converge for partition coefficients $\lambda \rightarrow 0$, since $\lambda - 1 \approx -1$ if λ is small. As a consequence, the results obtained from analysing solidification become independent of which modelling approach is pursued, due to the practical equivalence between the bounding solidification mechanisms.

Thus, if small partition coefficients apply to corium concrete mixtures, melt solidification can be treated according to the equilibrium approach. Correspondingly, the following section is concerned with evaluating partition coefficients of representative corium-concrete mixtures.

3.4.3.3   Examination of the partition coefficient based on representative phase diagrams

Determination of the partition coefficient relies on converting the multi-component mixture into a pseudo-binary system consisting of the refractory core oxide fraction UO_2-ZrO_2 on the one side and of the concrete oxides on the other side. Fig. 3.4-7 presents corresponding experimentally determined phase diagrams of corium-concrete mixtures involving core oxides (LCS), siliceous and limestone concrete.
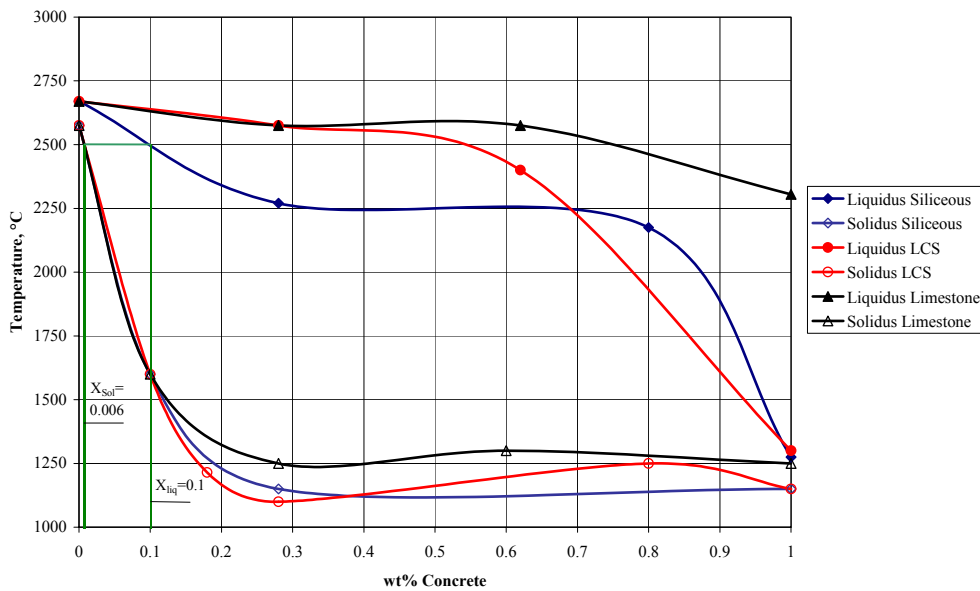

Fig. 3.4-7: *Pseudo-binary phase diagrams of mixtures of UO_2/ZrO_2 and siliceous, limestone common sand (LCS) and limestone concrete. The molar ratio between UO_2 and ZrO_2 is 1.6:1 [Roche 1994]*

Due to the strongly downward slope of the solidus lines, all above phase diagrams yield partition coefficients of generally below ~0.1. The partition coefficient e.g. of the mixture containing siliceous concrete amounts to 0.06 at a temperature of 2500°C.

This principal finding is applies to all core oxide/concrete mixtures investigated in Roche's experiments. Consequently, the type of solidification mechanism is of low significance for modelling solidification phenomena under MCCI conditions at least for common construction type concretes.

However, this conclusion is not stringently transferable to EPR specific conditions, since the types of concrete involved in the above solidus/liquidus measurements are poor in iron-oxide and so is the resulting melt. In contrast, sacrificial concrete in the reactor pit contains about 35wt% of Fe_2O_3 and thus leads to a correspondingly increased concentration in the oxide melt. Consequently, the next task is to analyse the solidification characteristics of corium-concrete mixtures containing substantial amounts of iron-oxides.

As there only exists a single liquidus measurement of an iron-oxide rich melt which is insufficient to construct a phase diagram, an approximate phase diagram is deduced based on existing liquidus and solidus curves of binary systems and on the thermochemical similarity between UO_2 and ZrO_2.

The procedure starts from a binary UO_2-ZrO_2 subsystem of the corium concrete mixture, for which the solidus/liquidus temperatures are determined using the following binary UO_2-ZrO_2 phase diagram.
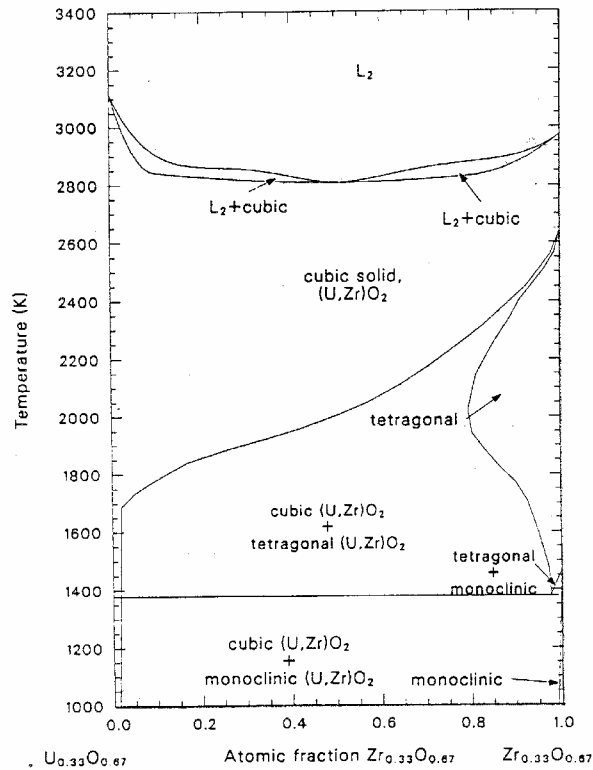
Fig. 3.4-8: *UO_2-ZrO_2 phase diagram [Hohorst 1990]*

The thus determined temperatures form an upper limit which translates to the left, core oxide side of the phase diagram to be constructed in equivalence with those presented in Fig. 3.4-7. As a result of dilution with the principal concrete decomposition products Fe_2O_3 and SiO_2, both, the liquidus and solidus temperatures decrease. In terms of liquidus temperature, quantification of the integral reduction as a consequence of coincident mixing with two components bases on addition of the individual contributions of Fe_2O_3 and SiO_2, i.e.,

$$T_{liq} = T_{liq,UO_2-ZrO_2} + \Delta T_{liq,FeO} + \Delta T_{liq,SiO_2} \qquad (3.4\text{-}20)$$

In contrast, the prediction of the solidus temperature applies a minimisation function instead of taking into account superimposing effects of the individual components. This approach avoids unphysically low solidus temperatures as they would result from a superposition of the individual effects.

$$T_{sol} = T_{sol,UO_2-ZrO_2} + \min\left[\Delta T_{sol,FeO}, \Delta T_{sol,SiO_2}\right] \qquad (3.4\text{-}21)$$

Principally, the reduction terms of both equations can be derived examining the respective ternary subsystems UO_2-ZrO_2-FeO and UO_2-ZrO_2-SiO_2.

However, there exist no phase diagrams of these ternary systems nor are complete phase diagrams available for the UO_2-FeO system as well as for the UO_2-SiO_2 system. Therefore, the ZrO_2-FeO and ZrO_2-SiO_2 phase diagrams, see Fig. 3.4-9 and Fig. 3.4-10, are used based on the assumption that UO_2 and ZrO_2 are chemically similar due to similar melting temperatures and the same type of bond. Following this assumption, the molar fractions of UO_2 and ZrO_2 in the ternary UO_2-ZrO_2-FeO and UO_2-ZrO_2-SiO_2 melt are condensed in an equivalent molar fraction of ZrO_2,

$$\psi_{ZrO_2}^{eq} = \psi_{ZrO_2} + \psi_{UO_2} \tag{3.4-22}$$

while the molar fractions of FeO and SiO_2 remain unchanged, hence resulting in

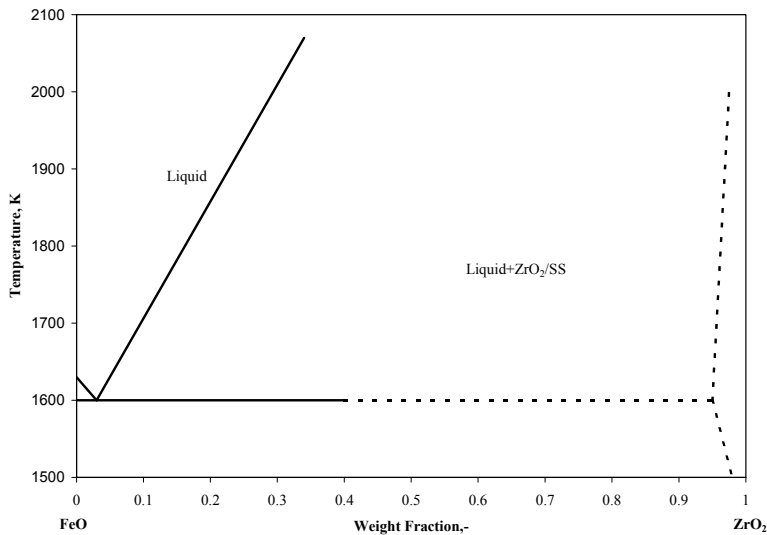$$\psi_{ZrO_2}^{eq} + \psi_{SiO_2} + \psi_{FeO} = 1 \tag{3.4-23}$$

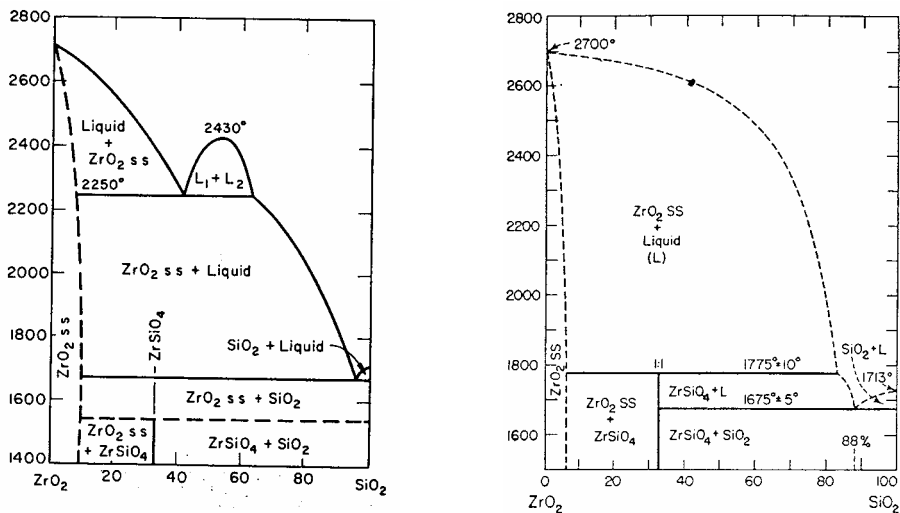**Fig. 3.4-9:** *FeO-ZrO₂ phase diagram [Hohorst 1990]*

Fig.3.4-10: *ZrO₂-SiO₂ phase diagrams (Levin 1975], absizza in °C, ordinate in wt%*

Estimation of the reduction of liquidus and solidus temperatures is based on a linearisation of the respective liquidus and solidus lines given in the phase diagrams of Fig 3.4-9 and Fig. 3.4-10,

$$\Delta T_{liq} = w_{liq} \xi_{add}^{mod} \text{ and } \Delta T_{sol} = w_{sol} \xi_{add}^{mod} \tag{3.4-24}$$

where 'add' denotes either FeO or SiO_2 and 'w' represents the slope of the liquidus or solidus line of the corresponding ZrO_2-FeO or ZrO_2-SiO_2 phase diagrams.

The modified mass fraction is introduced as a result of the difference between the molar weights of UO_2 and ZrO_2 which becomes effective due to combining both core oxides. Eq. 3.4-25 relates the correspondingly modified mass fraction with the molar fraction,

$$\xi_{add}^{mod} = \frac{1}{\dfrac{\psi_{ZrO_2}^{eq} M_{ZrO_2}}{\psi_{add} M_{add}} + 1} \tag{3.4-25}$$

The slope of the liquidus line of the ZrO_2-FeO phase diagram is,

$$w_{liq, ZrO_2-FeO} = -1330K \quad \xi_{FeO} < 0.97$$

while that of the solidus line amounts to,

$$w_{sol, ZrO_2-FeO} = -27000K \quad \xi_{FeO} \leq 0.05$$

$$w_{sol, ZrO_2-FeO} = 0K \quad \xi_{FeO} > 0.05$$

In terms of SiO_2, the left diagram of Fig. 3.4-10 yields a slope of the liquidus line of,

$$w_{liq, ZrO_2-SiO_2} = -1000K \quad \xi_{SiO_2} \leq 0.43$$

while for the same validity range, the liquidus line of the diagram to the right has a slope of,

$$w_{liq, ZrO_2-SiO_2} = -250K \quad \xi_{SiO_2} \leq 0.43$$

Therefore, an arithmetically averaged value of -500 K is used.

In contrast, both phase diagrams yield the same slope of the solidus line which is,

$$w_{sol, ZrO_2-SiO_2} = -1000K \quad \xi_{SiO_2} \leq 0.1$$

$$w_{sol, ZrO_2-SiO_2} = 0 \quad \xi_{SiO_2} > 0.1$$

The above outlined procedure is first tested against the measured liquidus temperature of Corium R' to check its principal feasibility before being applied to construct the phase diagram of corium concrete mixtures involving significant amounts of iron-oxides.

Corium R' was extensively investigated in the frame of the COMAS-project [Steinwarz 1999]. The composition of 44 wt% UO_2, 19 wt% ZrO_2, 27 wt% FeO and 10 wt% SiO_2 results in a liquidus temperature of ~1900°C. The effect of impurities was not analysed in that investigation.

The corresponding molar composition is 19/18/43.6/19.4 mol% UO_2/ZrO_2/FeO/SiO_2. The composition of the ternary subsystem UO_2/ZrO_2/FeO is 23.6/22.3/54 mol%, while that of the subsystem UO_2/ZrO_2/SiO_2 amounts to 33.7/31.9/34.4 mol%.

Fig. 3.4-8 yields 2810 K as liquidus temperature of the UO_2-ZrO_2 subsystem system which consists of ~50 mol% UO_2 and 50 mol% ZrO_2.

Given the equivalent molar fractions of ZrO_2 in the FeO- and SiO_2- containing subsystems of 0.459 and 0.656, Eq.3.4-25 yields the following modified mass fractions of FeO and of SiO_2,

$$\xi_{FeO}^{mod} = 0.41 \text{ and } \xi_{SiO_2}^{mod} = 0.2$$

The decrease of liquidus temperature by FeO and SiO_2 is obtained from inserting the modified fractions in combination with the appropriate slopes of liquidus lines into Eq. 3.4-24. The result is,

$$\Delta T_{liq,FeO} = -545K \text{ and } \Delta T_{liq,SiO_2} = -100K$$

Thus, according to Eq. 3.4-20, the estimated liquidus temperature of Corium R' amounts to 2165 K (1892°C) which is in adequate agreement with the measured value.

To construct the pseudo-binary phase diagram in the same manner as those given in Fig. 3.4-7, UO_2 and ZrO_2 were combined to the refractory core-oxide component, while the concrete component exclusively consists of FeO and SiO_2. The mass ratios between UO_2 and ZrO_2 as well as between FeO and SiO_2 were selected in agreement with the composition of Corium R'. In terms of the core oxides, a ratio of 2.3 results, while for the concrete component a ratio of 2.7 is obtained. Therefore, Corium R' corresponds to a corium-concrete mixture consisting of 63 wt% core oxides and 37% concrete. Fig. 3.4-11 plots the resulting pseudo-binary phase diagram.
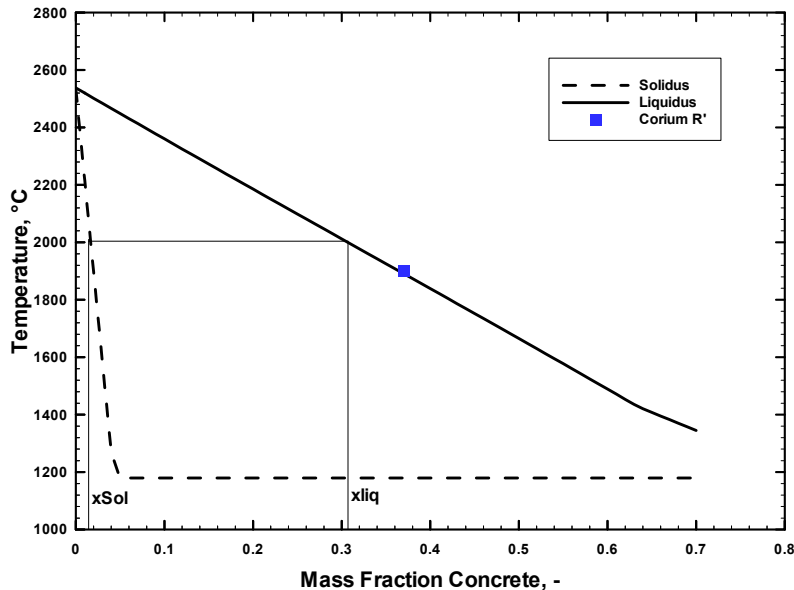
Fig. 3.4-11: *Pseudo-binary phase diagram for a corium–concrete mixture with a UO_2/ZrO_2 mass ratio of 2.3 and a FeO/SiO_2 mass ratio of 2.7*

The general form of the phase diagram depicted in Fig. 3.4-11 indicates that corium-concrete mixtures containing significant amounts of FeO also exhibit solidification characteristics which are independent of the solidification path, since λ is small. In particular, at 2000°C, the liquidus composition contains ~31 wt% concrete, while the solidus composition only consists

of less than 2 wt% concrete components. Hence, the partition coefficient amounts to ~0.06 which is fairly independent of temperature, as the liquidus and solidus curves are almost straight lines.

The evaluation of Eqs. 3.4-18 and 3.4-19 is depicted in Fig. 3.4-12 to illustrate the practical equivalence of the Scheil solidification and equilibrium solidification for Corium R'. The initial composition, x_0 required to evaluate above equations equals 37 wt%. The core oxides UO_2 and ZrO_2 complement this composition.

As is evident, both, the equilibrium solidification model and the Scheil model predict almost identical compositions of the solid phase up to a solid fraction of ~80%. For higher fractions, the solid phase composition predicted for equilibrium solidification approaches the global composition of Corium R', i.e. a concrete content of 37% and a core oxide content of 63wt%. In contrast, in case of Scheil solidification the last increment of solid formed before the melt is entirely solidified almost exclusively consists of the (low-melting) concrete components.

As is additionally obvious from Fig. 3.4-12, for a low content of solid phases in the melt corresponding to higher temperatures, the solid phase is predominantly composed of the refractory core oxides UO_2 and ZrO_2. Only for high solid mass fractions corresponding to low temperatures, the low-melting concrete components solidify and build up in the solid phase.
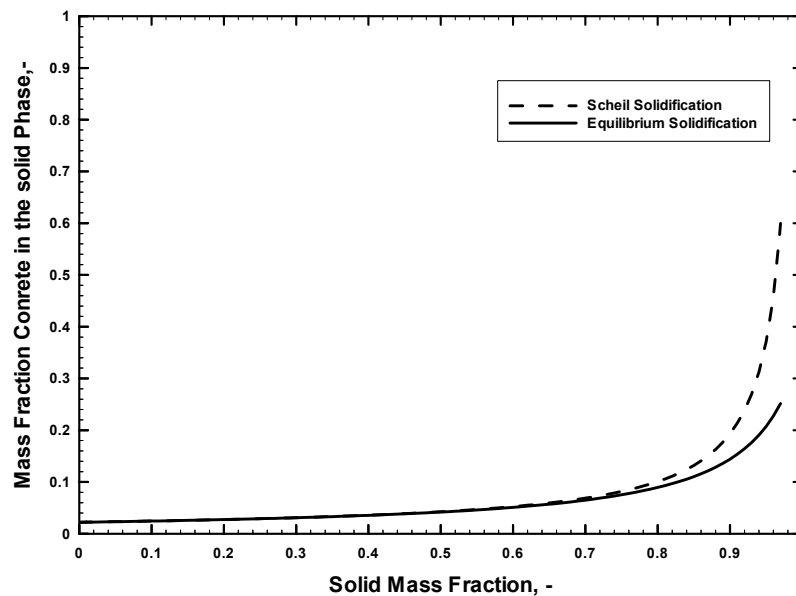
Fig. 3.4-12: *Composition of the solid fraction according to the Scheil model and to equilibrium solidification*

In terms of solidification during the MCCI, this effect translates into crusts that have a high content of core oxides, while the lower-melting concrete decomposition products predominantly accumulate as liquid phases in the bulk of the melt.

In summary, for both, corium melts involving common construction concretes as well as sacrificial concrete as selected for the EPR, the solidification characteristics evolving from either the Scheil or equilibrium solidification mechanism are equivalent. Consequently, it is justified to use the equilibrium approach to model solidification of complex oxidic core melts.

Given the outline of the fundamentals of thermochemical aspects as a necessary condition for a consistent modelling of MCCI, the next chapter introduces real solution thermochemistry into the modelling approach. This method offers an advanced representation of the prevailing thermochemical phenomena of complex core melts.

3.4.4 Modelling of complex chemical and phase equilibria using real solution thermochemistry

3.4.4.1 Motivation

Thermochemical phenomena which influence the behaviour of the MCCI constitute a principal element of the new modelling approach.

Therefore, description of these phenomena as accurate as reasonably achievable is essential to make this approach plausible. I.e. the validation of the code against representative experiments serves to scrutinise the plausibility. Conversely, only if this approach is plausible, the proof of the melt retention function of the pit can benefit from the specific characteristics inherent to the MCCI which are expected to be identified using this model.

The corresponding implementation of thermochemical modelling could be potentially based on the models deduced for assessing the principal thermochemical characteristics of the MCCI.

However, these models rely on idealised assumptions, as is the case for modelling of chemical reactions, or are limited to few melt components as is the case in terms of examining the solidification characteristics of the melt.

In particular, the Richardson-diagram which establishes the hierarchy of chemical reactions in the melt pool implies that reactants and products exist separately as pure phases. However, under real conditions like in the MCCI pool, reactants and products are in intimate contact with each other and with components that do not participate in the reaction. This contact results in forming mixture phases, provided that the components are miscible. The activity of components involved in such phases is generally below one, while for pure phases the activity is always unity. Although the formation of mixture phases can be taken into account for formulating the equilibrium constant, it is restricted to ideal solutions. Therefore, the activity coefficients are equal to one. However, for real conditions, real solutions arise, for which the activity coefficient is different from one.

As a consequence of idealising assumptions, the calculated composition may not appropriately correspond to the true composition. This in turn affects the solidification characteristics which are essential with respect to model the heat transfer characteristics of oxidic melts. Additionally, since chemical reactions are energetic, the location of the chemical equilibrium also affects the energy balance.

In terms of solidification behaviour, the model to construct the phase diagram for iron-oxide rich melts as a boundary condition to examine the solidification behaviour partially takes into account effects of real solutions, since it is directly derived from phase diagrams. However, it does not consider the effects related to the mutual influence between the melt components, if

more than two components are present in the melt. In particular, the presence of a third melt component may change the effect of the second melt component e.g. it might alter the liquidus temperature. This also holds true for the third and any additional melt component. Consequently, the approach to linearly superimpose the individual effects is limited to quite few melt components.

Following this reasoning, it is instrumental to rely on a comprehensive representation of the thermochemical characteristics of the MCCI pool. This representation should take into account the prevailing real behaviour of the melt involving the relevant components. To this end, the approach of a direct integration of a so-called *real solution* database into the overall modelling strategy for MCCI using an appropriate equilibrium solver is pursued for COSACO.

This approach enables to predict complex chemical reactions simultaneously with the formation of solid and liquid phases involving a large number of melt constituents. The results of such calculations include the important chemical composition of the solid and liquid mixture phases which may coexist in equilibrium for a given melt temperature.

Additionally, this methodology is highly advantageous, as it enables to address almost arbitrarily composed melts and thus significantly increases the flexibility of modelling with respect to a variation of the melt and concrete composition.

In terms of the melt retention in the pit, a more realistic representation of the thermochemical characteristics reduces uncertainties in the analyses and thus is beneficial for diminishing conservatisms involved in the definition of the concrete as well as in the arrangement of the corresponding layers.

3.4.4.2   General

Chemical equilibrium calculations for multi-component systems exhibit the highest potential to appropriately determine the constitution of the molten pool and the physical properties of the melt. These calculations require a representation of the Gibbs energy of the entire considered system as a function of temperature, pressure and composition.

In particular, the Gibbs-energy is usually given by (i) a contribution of the pure substances, plus (ii) a term which factors in the mixture entropy of ideal mixtures plus (iii) an excess term to take into account real solution effects [Eriksson 1990],

$$G_\phi = G_\phi^o + G_\phi^{id} + G_\phi^{xs} \tag{3.4-26a}$$

or, more specifically,

$$G_\phi = \sum_{i_\phi} n_{i_\phi} G_{m,i_\phi}^o + R_m T \sum_{i_\phi} n_{i_\phi} \ln \psi_{i_\phi} + R_m T \sum_{i_\phi} n_{i_\phi} \ln \gamma_{i_\phi} \tag{3.4-26b}$$

In particular, the excess term represents the difference between the real value and that if the solution was ideal.

Note that Eq. 3.4-26 only represents the Gibbs-energy for an individual phase denoted ϕ, where the index i_ϕ of Eq. 3.4-26b indicates the ith component of the respective phase. The

Gibbs-energy of multiphase systems, e.g. the MCCI pool, consists of contributions of all considered phases, i.e.

$$G = \sum_{\phi} G_{\phi} \qquad\qquad (3.4\text{-}27)$$

Equilibrium of the thermochemical system is attained, if the Gibbs-energy is at its minimum, i.e.

$$dG = 0 \qquad\qquad (3.4\text{-}28)$$

Minimisation of the Gibbs-energy particularly of real solutions is a complex task. There exist several commercially available equilibrium solvers, the particular one used for COSACO is the integratable solver CHEMAPP [GTT 1999]. The underlying property data used for the representation of the Gibbs-energy are stored in databases which can be classified into (i) pure substance databases, (ii) ideal solution databases and (iii) real solution databases.

Pure substance databases do not take into account mixture phases. Instead, the melt components are modelled to exist separately as pure phases. Specifically, the Gibbs-energy of the chemical system is only represented by the first term of Eq. 3.4-26 and thus results in a deterioration of thermochemistry modelling in comparison with the approach described in Chaps. 3.4.2 and 3.4.3.

Using *ideal solution databases*, also ideal mixture phases can be modelled. This modelling comprises the first two right hand terms of Eq. 3.4-26. The rightmost term of Eq. 3.4-26 vanishes, since the activity coefficients of the components in an ideal mixture equal unity. The main characteristic of an ideal solution is that the mixing enthalpy is zero. Thus, the Gibbs energy of mixing, i.e. the change in Gibbs energy due to the formation of a solution from the corresponding pure substances, is simply the change of entropy multiplied by temperature.

Though the first two terms of the right side of Eq. 3.4-26 constitute the major contribution to the Gibbs-energy [Erikkson 1990], miscibility gaps such as that between the metallic and oxidic melt, cannot be predicted but have to be anticipated by the database using specific pre-defined mixture phases. In particular, the individual oxidic and metallic melt components are assigned to an oxidic and metallic phase, respectively. This approach yields hard-wired phase compositions and can thus not be used to predict e.g. the limited solubility of metals in oxides which is essential for describing sub-stochiometric $(U,Zr)O_{2\text{-}x}$ melts. Additionally, solidus and liquidus temperatures and the corresponding solidification behaviour of real solutions, such as eutectic systems, cannot be addressed. As already the UO_2-ZrO_2 subsystem constitutes a real solution, the use of a real solution database for modelling the thermochemical melt behaviour in case of an MCCI is highly preferred.

Real solution databases offer the most advanced thermochemical modelling of a thermochemical system. The Gibbs energy of a real solution includes the rightmost excess term of Eq. 3.4-26 which takes into account non-ideal behaviour. The activity coefficient γ of this term contains the information relevant to predict real solution effects.

Due to the empirical nature of the activity coefficients, the database development involves a careful assessment of the available experimental data, e.g. of binary and ternary phase

diagrams. Methods to determine activity coefficients as a function of temperature and composition are discussed e.g. in [Horvard 1970] or [Frohberg 1994]. Though, strictly speaking, the obtained data only hold for these lower order systems, a multi-component system can be also adequately modelled using these data [Bhansali 1987]. It is worth noting, that unlike so-called adjustable parameters, the activity coefficients, though experimentally determined, are generic and thus are not adjustable to the characteristics of individual MCCI experiments.

However, real solution modelling cannot reduce the persisting uncertainties involved in phase diagrams, due to its reliance on empirical activity coefficients. Further, it requires an extensive evaluation of a huge amount of experimental data. Thus, in theory, already the modelling of a mixture consisting of four components principally requires the information on six binary subsystems. As a consequence, modelling of real solution behaviour concentrates on the pertinent melt components and phases.

Nevertheless, application of real solution modelling allows the prediction of complex chemical and phase equilibria involving the relevant melt components with the highest achievable accuracy, as the level of uncertainty is restricted to that induced by the underlying experimental data.

3.4.4.3   Development of the dedicated MCCI database COSCHEM

This chapter deals with the development of the MCCI database COSCHEM to simulate real solution effects with COSACO. The data stored in this database essentially rest upon the real solution database TDBCR 99 [Chevalier 1999].

The TDBCR 99 database is well-suited for the thermochemical modelling of in-vessel and ex-vessel situations during a severe accident. The development of this database was launched in 1989 and, since then, has received support from several multi-lateral activities, e.g. from the EU's CIT-project [Adroguer 1999]. With the 16+2 elements included in the database, all essential melt components which may arise under MCCI conditions, can be represented. These may be distributed into up to 39 mixture phases.

Up to now, this database has been extensively used only for chemical stand-alone analyses due to the adjustment of the data format to the requirements of the code GEMINI 2 [Cheynet 1992]. Thanks to the recent availability of the database in the CHEMAPP format, coupling with the thermal-hydraulic modelling of the MCCI is now possible.

The first task was to reduce the database size in order to decrease the calculation time. To this end, all fission products were omitted, as they only constitute a molar fraction of less then 1% in the initial core melt and thus were considered negligible for the thermochemical modelling of the MCCI. The thus generated new database COSCHEM includes the elements U, Zr, Si, Fe, Al, Ni, Cr, O, H, Ca, Mg. Alkali-metals such as sodium and potassium whose oxides are generally components of concrete, are neglected, since the portion of these oxides in the concrete composition is low [Roche 1994].

However, this list does not contain carbon which is a component of the concrete decomposition gas CO_2. The reason is that carbon is not included in the TDBCR database

which therefore does not allow to model CO and CO_2. Thus, CO and CO_2 were implemented as ideal gases into COSCHEM using the data of the SGTE database [Dinsdale 1991].

Since an MCCI involving liquid phases generally takes place at temperatures above ~1000 °C, all phases which are only stable below this threshold are not modelled. This measure reduced the number of solid phases from 36 to 13.

In case of an MCCI, liquid metal and oxide phases often exhibit a large mutual miscibility gap for sufficiently high temperatures and masses. Hence, two liquid solution phases are modelled in COSCHEM. In general, both liquids may contain the same constituents. However, under MCCI conditions in the case of two coexisting liquids, one will be oxide-rich, while the other will be rich in metal. The criterion established to discriminate the metal from the oxide phase, bases on the atom fraction of oxygen. In particular, if the liquid phase has an atom fraction of oxygen >50%, the phase character is oxidic, while for an oxygen content <50% the phase is assumed to adopt a metallic character.

Mixture Phase	Components	Character (metallic/oxidic)
Gas	H_2O, H_2, CO, CO_2, O_2, O	Gaseous
Liquid #1	UO_2, ZrO_2, SiO_2, Fe_2O_3, FeO, Al_2O_3 CaO, MgO, NiO, Cr_2O_3, U, Zr, Si, Fe, Al, Ca, Mg, Ni, Cr	Oxidic or metallic
Liquid #2		
BCC_A2(1)	Al, Cr, Fe, Ni, Si, Cr	Metallic
FCC_A1	Al, Ca, Ni	Metallic
FCC_A_1(1)	Al, Cr, Fe, Ni, Si, Zr	Metallic
HCP_A3_1	Al, Mg, ZrO_2, Zr	Metallic
HCP_A3_2	Al, Cr, Fe, Ni, Zr	Metallic
FCC_B1(1)	Al_2O_3, CaO, FeO, Fe_2O_3, MgO, SiO_2	Oxidic
Rho	Al_2O_3, Cr_2O_3, Fe_2O_3	Oxidic
FCC_B1(3)	CaO, FeO, MgO	Oxidic
FCC_C1	CaO, MgO, UO_2, ZrO_2, U, Zr	Oxidic
FCC_B1	CaO, MgO, NiO	Oxidic
CC	CaO, ZrO_2	Oxidic
FCC_B1(2)	Cr_2O_3, FeO, Fe_2O_3, NiO	Oxidic
Tet-Oxide	MgO, UO_2, ZrO_2	Oxidic

Tab. 3.4-1: *Mixture phases, their constituents and characters considered in the real solution database COSCHEM: Abbreviations of structure names: BCC ~ Body Centered Cubic, FCC ~ Face Centered Cubic, HCP ~ Hexagonal Closed Packed Structure, Rho ~ Rhomboedric Structure, CC ~ La_2O_3 structure, Tet-Oxide ~ Tetragonal Structure*

Tab. 3.4-1 summarises the mixture phases of the database, their potential components and characters as considered for an implementation into COSACO.

It shows that the gas phase which is modelled as an ideal mixture, may consist of up to six gases. In general, gaseous core melt constituents e.g. Fe, UO_2, are also constituents of the gas phase. Their molar fraction in the gas phase is proportional to the partial pressure. Since the maximum partial pressure of the condensed melt components is limited to the vapour pressure

which is low, these components are not modelled. Tab. 3.4-1 further indicates that an oxidic or metallic character has been assigned to the individual phases. This significantly affects the mass transfer in the melt pool as well as stratification of the melt pool involving metallic and oxidic layers, see Chap. 3.5.

Analogous to the liquid phases, also solid phases are not necessarily solely composed of either stochiometric oxidic compounds or metallic elements, but may also attain sub-stochiometric compositions as the phase $(U,Zr)O_{2-x}$ which prevails in a number of core melt situations. Specifically, the FCC_C1 phase can be sub-stochiometric while retaining its oxidic character. Equivalently, the HCP_A3_1 phase can dissolve oxygen while maintaining its metallic character.

In addition to the condensed mixture phases, the TDBCR database also contains stochiometric compounds as pure phases. These pure phases are also retained in the COSCHEM database, though the corresponding compounds are generally dissolved in mixture phases instead of being stabilised as pure phases. This effect is attributed to the increase in entropy if mixture phases are formed.

In summary, chemical phenomena have significant implications on the overall approach to model MCCI. These do not exclusively refer to the principal heat transfer characteristics, but also to the representation of the molten pool.

Due to the existence of miscibility gaps, the MCCI pool may stratify into layers consisting of either oxidic or metallic phases. In turn, this process affects the transport of masses and energy through the pool and thus forms a prerequisite for establishing the mass and energy balance. Solution of the energy balance with respect to temperature requires a close correlation with the thermochemical modelling. As a result, a sound thermochemical state arises which includes the integral composition of the melt as well as the redistribution of the melt components on coexisting solid and liquid phases. Eventually, this state establishes the basis for modelling and calculating the heat transfer within the pool.

The description of modelling in the succeeding chapters follows this logic.

3.5 Representation of the MCCI pool, mass- and energy balance

3.5.1 General

Due to the existence of a large miscibility gap between the oxidic and metallic melt, the pool may stratify into layers consisting of either oxidic or metallic phases. Depending on the density difference between the oxide and the metal layer, the pool is assumed to consist of three or two layers. In particular, the oxide melt as it is released from the reactor pressure vessel is much denser than the metal melt, i.e. depending on the Zr-oxidation level, the difference amounts to ~2000 kg/m^3. Therefore, the oxide layer is initially located below the metal. Additionally, light concrete decomposition products resulting from concrete ablation by the metal layer accumulate on top of the metal and develop a light oxidic layer, thereafter called slag layer.

In consequence, during the initial MCCI, the melt pool is represented by three layers involving (from the bottom up) (i) a heavy oxidic layer, (ii) a metallic layer and (iii) a slag layer.

During the ongoing MCCI, light concrete decomposition products mix with the oxidic melt and by this continuously reduce its density ultimately below that of the metallic melt. Upon achieving the state of equal densities, the layer arrangement is assumed to invert instantly. This process is called layer inversion. Following layer inversion, the pool only consists of two layers (from the bottom up): a metallic and an oxidic layer. The slag layer that has developed until layer inversion disappears, as it is assumed to completely dissolve in or react with the oxidic melt.

However, a stratified situation potentially does not develop due to MCCI gases agitating the pool, thereby resulting in mechanical mixing of the thermochemically immiscible oxidic and metallic phases. To address this effect, a mixed configuration is additionally modelled which assumes the pool as an intimate mixture of oxidic and metallic phases. This mode is valuable to assess the consequences of postulated mixing on the melt retention function of the pit, though for the EPR a mixed situation is not considered to prevail. This assumption bases on the given high temperature difference between the metallic and oxidic melt (initially between 500°C and 1000°C according to in-vessel analyses) which leads to a rapid solidification of the refractory oxidic components at the common interface and thus to a progressive abatement and eventually to a termination of mixing.

The next paragraphs describe the representation of the molten pool and the associated mass transfer. Given this basis, the energy balance is established in Chap. 3.5.4.

3.5.2 Mass transfer for stratified layers

3.5.2.1   Mass transfer prior to the layer inversion

During the early phase of the MCCI, the oxidic melt is denser than the metallic one. Thus, a layer predominantly consisting of oxidic components forms underneath a layer of metallic components. As depicted in Fig. 3.5-1, the heavy oxidic system may consist of UO_2, ZrO_2, CaO, MgO, Al_2O_3, Fe_2O_3, FeO, SiO_2, Cr_2O_3, metallic U and Zr during this early phase, where metallic U and Zr are component of the substochiometric $(U,Zr)O_{2-x}$ melt In addition, further metals e.g. Fe, Si and Al as reaction by-products, may dissolve, though to a minor extent, in the oxidic melt.

The metal layer may be composed of the metallic components Fe, Ni, Cr, Zr, U, Si, Mg and Al, where Si and Al arise from chemical reactions of Zr with alumina and silica, respectively. In addition, also small fractions of oxides may be dissolved in the metallic melt, as is indicated in Fig. 3.5-1.

The principal idea behind the modelling of demixing and corresponding mass flow through the pool is to concentrate phases that exhibit an oxidic character into an oxidic or a slag layer, while the metallic layer is exclusively formed of metallic phases.

Given the prerequisite that at least two phases exist in the melt, spatial demixing of condensed material and corresponding mass flow through the pool is assumed to take place if the following two criteria are fulfilled.
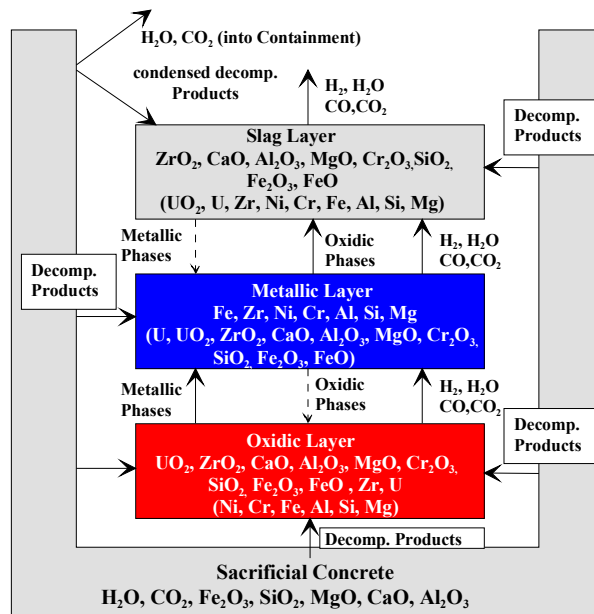

Fig. 3.5-1: *Melt pool configuration and mass transfer before the inversion of layering*

The first criterion for demixing is met if the character (metal/oxide) of the potentially relocating phases is different from that of the considered layer. In terms of solid phases, the phase character can be directly inferred from Tab. 3.4-1, while for coexisting liquid phases, the phase character is identified according to the rule given in Chap. 3.4.4.3.

Second, the density of the potentially relocating phase must be different from that of the ambient layer.

Specifically, the metallic phases which are generated within the oxidic layer, buoy up and mix with the metallic layer, since they are lighter than the surrounding oxidic melt.

Oxidic phases which arise from the interaction of concrete with the metallic melt within the metallic layer, predominantly accumulate as a slag layer above the metallic melt due to their generally lower density. Only oxidic phases which have a higher density than the surrounding metal melt, are passed downwards to the oxidic layer.

The slag layer located above the metallic layer likely consists exclusively of the completely oxidised components ZrO_2, CaO, MgO, Al_2O_3, Fe_2O_3, SiO_2, Cr_2O_3, UO_2. Thus, it does not exhibit a potential for further oxidation reactions. Since, however, the transfer of oxide phases containing metal constituents cannot be excluded a-priori, the slag layer may also contain Fe, Al, Si, Zr, Cr, Mg, Ni and U.

Concrete decomposition above the melt free surface takes place due to thermal radiation emitted from the slag layer. As Fig. 3.5-1 indicates, only the condensed decomposition products resulting from this process are transferred to the slag layer, while the gaseous concrete decomposition products H_2O and CO_2 are released into the containment.

3.5.2.2   Mass transfer after layer inversion

As part of the layer inversion, the slag layer mixes with the formerly heavy oxidic layer. For the situation following layer inversion, the mass flow is sketched in Fig. 3.5-2.

Metallic phases which are generated in the oxidic layer, mix with the metallic layer underneath, if their density is greater than that of the oxidic melt. However, possibly lighter metallic phases consisting to a large extent of light metallic components such as Si, are retained in the oxide layer instead of forming a separate layer above. This assumption bases on the very limited potential for the formation of such phases after layer inversion which is expected to occur only after the oxidic melt attains complete oxidation. For relatively denser oxidic phases arising in the metal layer, this assumption is also applied. Conversely, oxidic phases which are lighter than the ambient metallic melt, escape from the layer in upward direction and mix with the oxidic melt.
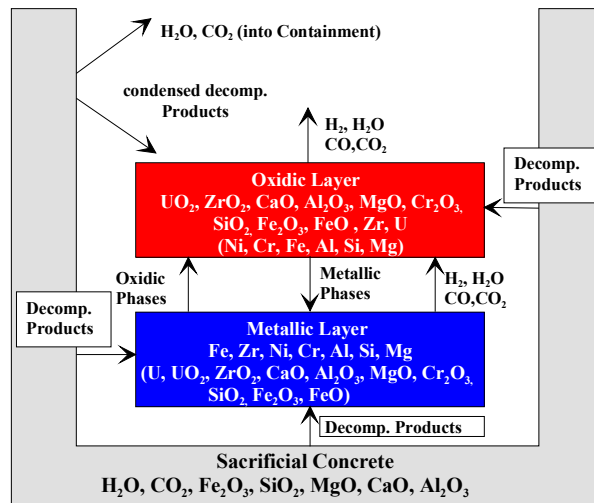

Fig. 3.5-2: *Melt pool configuration and mass transfer after the inversion of layering*

3.5.3 Mass transfer in the melt pool, mixed melts

In addition to the layered pool model, a mixed option has also been incorporated in the code. In the mixed mode the metallic or, conversely, the oxidic melt can be imagined to form a dispersed (droplet-) phase within the melt pool.

As indicated in Fig. 3.5-3, the melt pool may consist of the same oxidic and metallic components as for the layered arrangement of the pool. Aside from assessing the consequences of postulated mixing, this mode is particularly useful to investigate MCCI involving melt pools predominantly consisting of oxidic components.
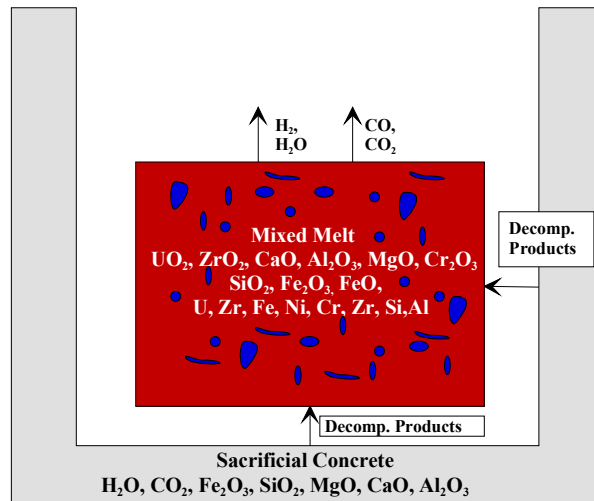
Fig. 3.5-3: *MCCI pool, mixed option*

Due to the permanent admixture of concrete decomposition products, the metallic melt components continuously oxidise. Thus, in theory, the melt becomes completely oxidic after a sufficient amount of concrete is incorporated.

3.5.4 Energy balances for the layers - calculation of bulk temperatures

As depicted in Fig. 3.5-4, the upper, in this case oxidic layer, transfers sensible heat to the adjacent concrete, as well as exchanges heat with the underlying metallic layer. In contrast, the lower layer only transports sensible heat to the concrete walls and to the overlying melt layer. If the system consists of three layers, the medium layer exchanges heat with the upper and lower layer in addition to the concrete walls.
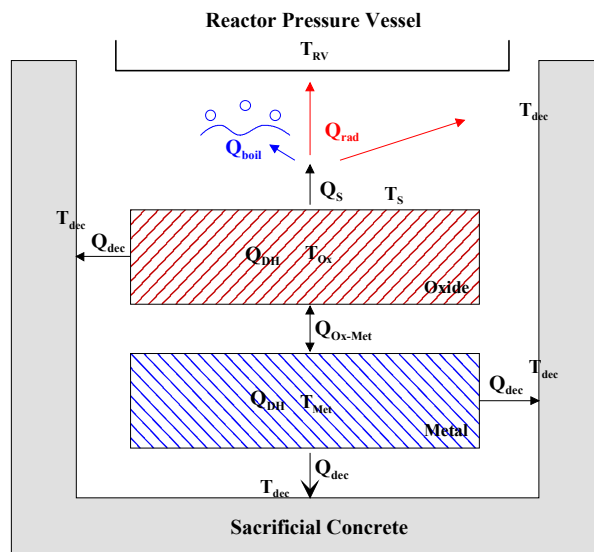

Fig. 3.5-4: *Heat transfer in the melt pool shown by way of example for the configuration after layer inversion*

Heat transfer at the free surface occurs according to the boundary conditions which is either a dry melt free surface as in the case of the EPR or a flooded surface as in the MACE

experiments. Radiation from the melt free surface results in decomposition of concrete located above as well as in heat-up of the remaining structures of the reactor pressure vessel.

Besides the sensible heat transfer by bubble-driven convection, material and corresponding enthalpy streams enter the melt layer and either pass through or become incorporated in accordance with the modelling of mass transfer. In both cases, these streams are thermochemically equilibrated with the layer which they enter.

Thus, the energy balance for the upper layer becomes for an isobaric change of state

$$\frac{dE}{dt} = \dot{Q}_{DH} - \dot{Q}_{dec} - \dot{Q}_{S} \pm \dot{Q}_{Ox-Met} + \sum_{i_{et}} \dot{m}_{i_{et}} e_{i_{et}} - \sum_{i_{ec}} \dot{m}_{i_{ec}} e_{i_{ec}} \tag{3.5-1}$$

where

$$\frac{dE}{dt}:$$

Change of layer enthalpy with time

$$\dot{Q}_{DH}:$$

Decay power

$$\dot{Q}_{dec}:$$

Heat flux at the concrete boundary which results in decomposition

$$\dot{Q}_{Ox-Met}:$$

Heat flux between the oxide and metal layer

$$\dot{Q}_{S}:$$

Heat flux at the free surface

$$\sum_{i_{et}} \dot{m}_{i_{et}} e_{i_{et}}:$$

Enthalpy flows entering the melt layer

$$\sum_{i_{ec}} \dot{m}_{i_{ec}} e_{i_{ec}}:$$

Enthalpy flows escaping from the melt layer

The corresponding mass balance is given as

$$\frac{dm}{dt} = \sum_{i_{et}} \dot{m}_{i_{et}} - \sum_{i_{ec}} \dot{m}_{i_{ec}} \tag{3.5-2}$$

where

The term $\dot{Q}_{dec}$ of Eq. 3.5-1 which describes the heat transfer to the concrete sidewalls is obtained from an integration over all concrete nodes blanketed by melt, according to the geometrical model described in Chap. 3.7.4.

The bulk temperatures are determined from the specific bulk enthalpies. This approach involves (i) the representation of the melt specific enthalpy as a function of temperature only based on the melt constitution and (ii) the determination of the actual melt enthalpy based on the energy conservation equation.

The modelling of specific enthalpies has been motivated by the need for a simplification of the energy balance for chemically interacting components. The aim of this simplification is to avoid an explicit chemical source term. What is carried out by defining the enthalpies for a reference state, i.e. 298.15 K and 1 bar, is as follows: The enthalpy of the elements in their stable states at 298.15 K and 1 bar is zero. Therefore, the enthalpy of the compounds in their

stable states at 298.15 K and 1 bar is equal to their heat of formation which is directly measurable. The corresponding formation reaction involves the arising compound as a *product* and the elements from which the compound is formed, as *educts*. This method is widely used in the field of chemical thermodynamics.

Given this definition of the reference enthalpy, the molar enthalpy of a pure substance as a function of temperature is obtained from,

$$e(T) = e(298) + \int_{298.15}^{T} c\,dT + \sum \Delta e \qquad (3.5\text{-}3)$$

Aside from the integral of specific heat, Eq. 3.5-3 involves any potentially occurring enthalpy change due to transformations in the lattice structure plus the heat of fusion. The reference enthalpy e(298) is either zero for elements that are stable at the reference state or in case of compounds, it equals the heat of formation. The bi-atomic gases H_2 and O_2 belong to the group of elements.

As constituents in the core melt may stay liquid below or solid above their individual melting points, a linear extrapolation of specific enthalpies beyond their original validity limits is applied to meet such conditions,

$$e_s = e_s\big|_{T_{mp}} + \frac{de_s}{dT}\bigg|_{T_{mp}} \left(T - T_{mp}\right), \quad T > T_{mp} \qquad (3.5\text{-}4a)$$

$$e_l = e_l\big|_{T_{mp}} + \frac{de_l}{dT}\bigg|_{T_{mp}} \left(T - T_{mp}\right), \quad T < T_{mp} \qquad (3.5\text{-}4b)$$

As indicated by Eq. 3.5-4, this linear extrapolation implies a constant extrapolated specific heat. The enthalpy data as a function of temperature can be obtained e.g. from the SGTE database for pure substances [Dinsdale 1991] for the individual melt components.

Given the specific enthalpies of the individual solid, liquid and gaseous components involved in the thermodynamic system, the specific enthalpy of the considered layer consists of the solid, liquid and gas phase enthalpies divided by the corresponding mass,

$$e = \frac{\sum\limits_{i_s} m_{i_s} e_{i_s}(T) + \sum\limits_{i_l} m_{i_l} e_{i_l}(T) + \sum\limits_{i_g} m_{i_g} e_{i_g}(T)}{\sum\limits_{i_s} m_{i_s} + \sum\limits_{i_l} m_{i_l} + \sum\limits_{i_g} m_{i_g}} \qquad (3.5\text{-}5)$$

where i_s denotes the number of solid components, i_l the liquid components and i_g the gaseous components of the considered layer.

Notably, the specific enthalpy of the considered melt layer consists of contributions from both the entirety of *all* solid and liquid phase components considered in the system aside from gaseous components. This is a result of the postulate of equilibrium solidification which assumes that solid and liquid phases coexist in overall thermochemical equilibrium.

Finally, the energy conservation equation is rearranged as follows:

$$E\big|_{n+1} = E\big|_{n} + \frac{dE}{dt} \cdot \Delta t \qquad\qquad (3.5\text{-}6)$$

and the mass conservation equation is discretised as

$$m\big|_{n+1} = m\big|_{n} + \frac{dm}{dt} \cdot \Delta t \qquad\qquad (3.5\text{-}7)$$

where 'n' indicates the timestep. This yields a second equation for the specific enthalpy,

$$e(T)\big|_{n+1} = \frac{E}{m}\bigg|_{n+1} \qquad\qquad (3.5\text{-}8)$$

The new temperature of the melt is finally obtained from equating Eq. 3.5-5 with Eq. 3.5-8. The resulting expression is iteratively solved with respect to temperature under the condition of thermochemical equilibrium. As a result, a *consistent* thermochemical state comprising melt temperature, melt composition and repartition of the melt components on the liquid and solid phases is obtained.

Given the configuration and energetic representation of the pool, the following chapter discusses the arising heat flux distribution within the melt pool as well as the corresponding modelling of heat transfer along the pool boundaries.

3.6 Heat flux distribution and modelling of heat transfer

3.6.1 Heat flux distribution for oxide and metal melts

For both, oxidic and metallic melt pools, the gas-driven convection inside the melt is assumed to result in equal heat flux densities along the boundaries of the pool, if the thermal boundary conditions are identical. Specifically, if the capacities of the heat sinks at all boundaries of the pool to absorb heat are identical, then the heat fluxes transferred to each heat sink are equal. Conversely, if a heat sink is not capable of absorbing heat at all, i.e. if it is adiabatic, no heat fluxes are transferred through the corresponding boundary.

In terms of concrete ablation, the assumption of an isotropic heat flux distribution results in equal radial and axial ablation rates due to the identical characteristics of the heat sink.

The assumption rests on the following experimental observations. A post-test examination of MACE M0 [Spencer 1991] as the only available 2D MCCI test involving an oxidic melt, indicated an about equal extent of downward and sideward erosion.

Also in case of an MCCI with metallic melt, an isotropic heat flux distribution is assumed, given the results of the large-scale 2D experiments recently executed under the umbrella of CORESA R&D programme. These transient experiments investigated the 2D erosion behaviour of various sacrificial and construction types of concrete interacting with ~1 Mg metal melt. The melt's initial temperature amounted to ~2000°C. Fig. 3.6-1 presents the results obtained for LCS concrete and for iron oxide-rich sacrificial concrete.
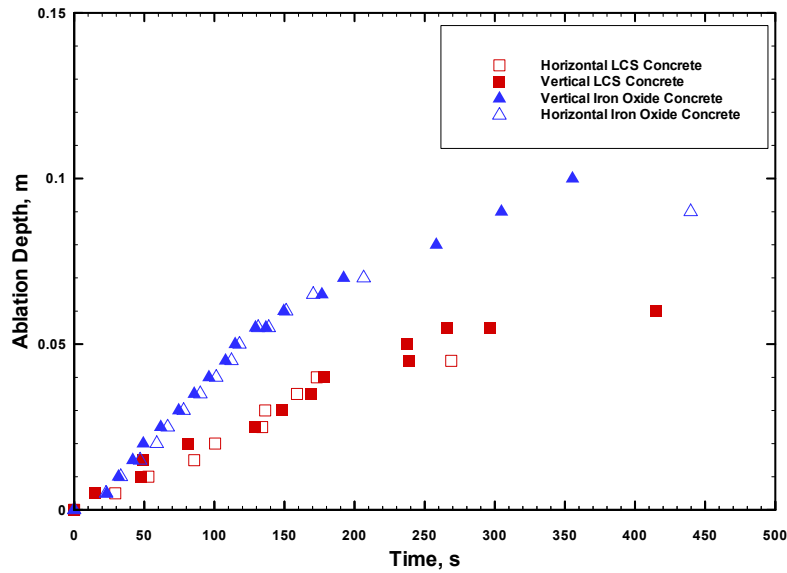
Fig. 3.6-1: *Concrete ablation at the vertical and horizontal sidewalls for LCS concrete and iron oxide-rich concrete observed in the CORESA tests [Häfner 2001]*

As is evident, the evolution of ablation front progression in vertical and horizontal direction is similar for both types of concrete.

Additional support for assuming isotropic behaviour comes from the BALI-experiments [Bonnet 1999] which focus on the heat transfer in gas-agitated liquid pools with variable viscosity. Experiments performed in this frame to examine upward and downward power distribution indicated that gas injection favours an isotropic heat flux distribution, see Fig. 3.6-2.
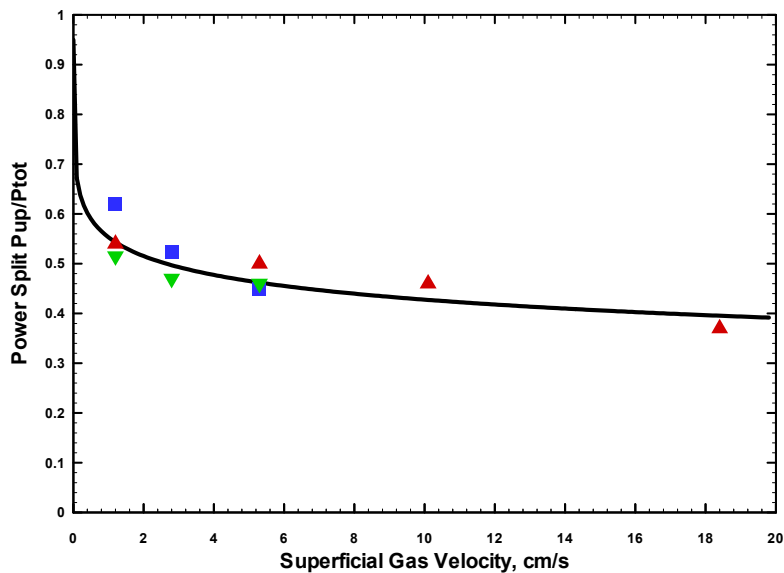

Fig. 3.6-2: *Power distribution as a function of superficial gas velocity [Bonnet 1999]. P_{up} denotes the power transferred upwards, while P_{tot} denotes the total power deposited in the fluid*

Evaluation of Fig. 3.6-2 indicates that already small superficial gas velocities of ~1.5 cm/s induce a ratio between downward to upward heat transfer of ~1. In contrast, given the condition of undisturbed natural convection, i.e. j_G is zero, ~95% of the internally generated power are passed upwards. Under MCCI conditions, the superficial gas velocities are definitely well above 1.5 cm/s, as various MCCI experiments indicate. Specifically, the superficial gas velocity of the ACE/MACE tests amounted to ~2.0-5.0 cm/s on the average. This observation supports the initial assumption that the decay power generated in the melt is homogeneously distributed over the pool boundaries.

Given the principal characteristics of heat flux distribution within the MCCI pool, Chap. 3.6.2 addresses the specific modelling of heat transfer for oxidic melts, while Chap. 3.6.3 is concerned with the modelling for metallic melts.

3.6.2 Modelling of heat transfer for oxidic pools

3.6.2.1   General

To recall, in the existing MCCI codes the modelling of heat transfer for oxidic melts is widely decoupled from thermochemical phenomena within the melt. At the same time, thermochemical aspects are modelled in a fairly simplified manner.

One essential simplification constitutes the approximation of the multi-component system as a single component melt in terms of modelling of crust formation which has significant implications on the prediction of heat transfer. In particular, the crust model incorporated e.g. in WECHSL assumed onset of crust formation at the pool boundaries only after the interfacial temperature has fallen below the solidus temperature. The composition of the material which is taken out of the melt pool to form a crust is assumed to equal the integral composition of the melt. Due to choosing the solidus temperature in combination with using adaptable parameters to affect interfacial heat transfer, the criterion for crust formation may be met only late into the MCCI or after the melt undergoes a significant cool down. At the same time, it is assumed that melt solidification predominantly occurs in the volume of the melt rather than at the cold boundaries of the pool.

Such modelling contrasts with ordinary solidification processes in industrial application, e.g. moulding, in which the melt solidifies and deposits as a crust at the cold interface to the mould instead of in the volume, see e.g. [Biloni 1996]. Further, solidification and corresponding partition of melt components on solid and liquid phases corresponds to the precipitation characteristics established by the phase diagram of the considered melt. In terms of core concrete mixtures, this means that the refractory components UO_2 and ZrO_2 begin to solidify already after the melt temperature shortly falls below the liquidus line, while the lower melting components only solidify at temperatures sufficiently below the liquidus. Consequently, the solid phases are initially rich in refractory components, whereas the concentration of low melting components only gradually increases with declining temperature. Accordingly, the temperature at the melt/crust interface to a first approximation correlates with the liquidus line, instead of being an almost fixed, physically unreasonable temperature at any stage of solidification. On this basis, it is judged that the existing models do not adequately address the pertinent effects of melt solidification of oxidic melts and their

effect on the heat transfer characteristics and therefore offer only limited ability to predict the experimentally observed phenomenology of the MCCI.

In contrast, the new approach aims at assembling a model that consistently describes the heat transfer characteristics involving spatial separation of solid and liquid phases as well as the thermal hydraulic behaviour of the MCCI pool. The spatial separation as it occurs in moulding, is generally denoted as segregation and was introduced into the field of severe accidents by [Seiler 1996] under the term *phase segregation hypothesis*.

A perfect segregation corresponding to moulding translates into melt solidification exclusively at the melt-concrete interfaces and other potential heat sinks at the boundaries of the melt system (e.g. the melt free surface, cooled sidewalls).

However, contrary to moulding, the MCCI embodies a distinctly different phenomenon which is mixing of relatively cold material, i.e. the concrete decomposition products, with the bulk of the melt.

Similar to the formation of condensate in the volume of humid air flow due to spraying water into the flow, i.e. what is done to condition air, concrete decomposition products extract energy from the bulk while heated to the resulting mixture temperature. Eventually, this process results in crystallisation in the volume of the melt, if the mixture temperature is below the liquidus.

Based on this phenomenology, a consistent modelling of melt solidification involves crystallisation in the volume in parallel with crust formation at the cold boundaries of the melt pool. In this manner, it is expected that adjustable parameters become unnecessary.

3.6.2.2   New modelling approach involving characteristic solidification phenomena

The principal assumption for this new approach is a partial spatial separation of the solid and liquid phases by deposition of the predominantly refractory components of the melt at the colder pool boundaries. At the same time, a fraction of the solid phases is assumed to stay mixed with the melt due to crystallisation in the volume. Equivalent to the composition of the solid located at the pool boundaries, the phases within the melt volume also consist of the refractory core oxides rather than of low melting concrete decomposition products.

The resulting crust layer effectively limits the heat extraction out of the melt pool. Therefore, the melt itself forms an upper limit for heat removal and thus for cooling, while the heat sink at the outer side of the crust can only lower this limit, i.e. to zero if it is adiabatic. On the other hand, if one assumes an ideal heat sink, it can only absorb the heat flux which is delivered by the oxidic melt. Clearly, not the conditions at the melt boundaries limit cooling but the heat transfer characteristics within the melt.

This aspect also implies that the ablation front progression in downwards direction is governed by the oxide melt even if the metallic melt is located below the oxide. In particular, after layer inversion concrete ablation is first characterised by transient ablation due to cool-down of the likely superheated metallic melt. However, after the transient effects fade away, downward erosion is proportional to the decay heat which is predominantly generated in the

oxidic melt. Again, the extent of heat transfer to the metal melt as well as to the rest of the surrounding boundaries is mainly determined by the phenomenology inside the oxide melt.

The temperature condition at the crust/melt boundary is close to the liquidus temperature of the melt. The volumetric solid fraction in the melt increases the viscosity and thus contributes to increasing the heat transfer resistance from the bulk to the ablating concrete surface.

The integral amount of solid phases which is given by the thermochemical state of the melt, forms the prerequisite for modelling crust-limited heat transfer and for determining the amount of solids staying in the bulk. However, the equilibrium solidification model used to predict the thermochemical state of the melt assumes the melt as being an intimate mixture of solid and liquid phases, see Fig. 3.6-3. Hence, the next step is to develop a methodology to quantitatively discriminate between the solids that stay mixed with the melt and those that redistribute over the cold boundaries of the pool.
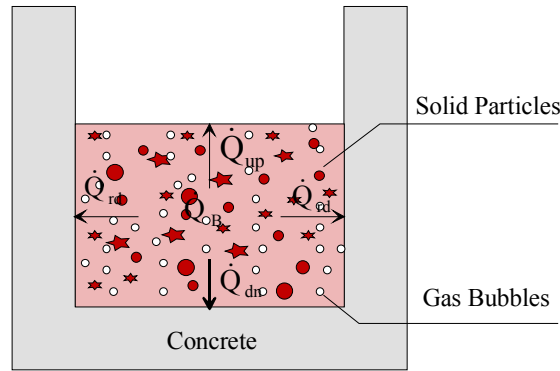

Fig. 3.6-3: *MCCI pool with intimately mixed solid and liquid phases*

The principal idea behind the corresponding modelling rests on assuming that every heat sink of the molten pool contributes to the formation of solid phases. These heat sinks comprise the sensible heat fluxes leaving the pool over its boundaries as well as a volumetric heat sink due to enthalpy streams entering/escaping from the pool.

The modelling starts with assuming a change of state of the system from '1' to '2' within a certain period, where states '1' and '2' correspond to the initial and actual situation, respectively. The change of state arises due to cumulated heat fluxes entering/leaving the system over the boundaries, the decay heat generated within the considered period and due to incoming and outgoing masses. Integration of the energy balance equation, see Eq. 3.5-1, over the considered period reflects this change.

$$E^2 - E^1 = \sum_{i_{et}} \Delta m_{i_{et}} e_{i_{et}} - \sum_{i_{ec}} \Delta m_{i_{ec}} e_{i_{ec}} + Q_{DH} + \sum_{j_{et}} Q_{j_{et}} - \sum_{j_{ec}} Q_{j_{ec}} \qquad (3.6\text{-}1)$$

where

$\qquad$ E $\qquad\qquad\qquad$ Enthalpy of the melt pool

$\qquad \sum_{i_{et}} \Delta m_{i_{et}} e_{i_{et}} \qquad$ Enthalpy entering the pool within the considered period

$\qquad \sum_{i_{ec}} \Delta m_{i_{ec}} e_{i_{ec}} \qquad$ Enthalpy escaping from the pool within the considered period

Q_{DH} Decay heat released within the considered period

$Q_{j_{et}}$ Cumulative sensible heat entering the pool over a pool boundary surface within the considered period

$Q_{j_{ec}}$ Cumulative sensible heat escaping from the pool over a pool boundary within the considered period

and the superscripts '1' and '2' denote the respective states.

The amount of solids in the melt at state '2' is balanced by the decay heat which prevents the melt from complete solidification and by the total removed heat which restricts melt liquification. On the basis of this phenomenology, it is plausible that the total heat removed from the system within the considered time corresponds to the total amount of solids present at state '2'. Hence, a fraction of removed heat corresponds to a fraction of solids. In terms of the MCCI pool, this means that the fraction of solids allocated to a considered sink increases with increasing fraction of heat removed at that sink.

However, before setting up the governing equation for assigning the solids to the respective sinks, the following task concerns the quantification of the heat sink in the volume due to mixing of the melt with concrete decomposition products. While the sensible heat fluxes along the boundaries are explicitly given through the effective heat transfer coefficient and the driving temperature difference, the volumetric heat sink is extracted from the energy balance.

Given the notation of the change of system enthalpy in terms of contributions from the individual liquid and solid components and their change in mass, i.e.

$$E^2 - E^1 = \sum_{i_s}\left(m_{i_s}^1 + \Delta m_{i_s}\right)e_{i_s}^2 + \sum_{i_l}\left(m_{i_l}^1 + \Delta m_{i_l}\right)e_{i_l}^2 - \left(\sum_{i_s}\left(m_{i_s}^1\right)e_{i_s}^1 + \sum_{i_l}\left(m_{i_l}^1\right)e_{i_l}^1\right) \tag{3.6-2}$$

the energy conservation equation as given in Eq. 3.6-1 can be transformed to

$$m^1\left(e^2 - e^1\right) = -\sum_{i_s}\Delta m_{i_s}e_{i_s}^2 - \sum_{i_l}\Delta m_{i_l}e_{i_l}^2 + \sum_{i_{et}}\Delta m_{i_{et}}e_{i_{et}} - \sum_{i_{ec}}\Delta m_{i_{ec}}e_{i_{ec}} + Q_{DH} + \sum_{j_{et}}Q_{j_{et}} - \sum_{j_{ec}}Q_{j_{ec}} \tag{3.6-3}$$

where

$$m^1\left(e^2 - e^1\right) = \sum_{i_s}m_{i_s}^1\left(e_{i_s}^2 - e_{i_s}^1\right) + \sum_{i_l}m_{i_l}^1\left(e_{i_l}^2 - e_{i_l}^1\right) \tag{3.6-4}$$

Note that in both, states '1' and '2' the system merely consists of solid and liquid phases since the gaseous phases were released into the overlying atmosphere during the change of state.

The heat sink in the bulk readily arises from Eq. 3.6-3,

$$Q_B = -\sum_{i_s}\Delta m_{i_s}e_{i_s}^2 - \sum_{i_l}\Delta m_{i_l}e_{i_l}^2 + \sum_{i_{et}}\Delta m_{i_{et}}e_{i_{et}} - \sum_{i_{ec}}\Delta m_{i_{ec}}e_{i_{ec}} \tag{3.6-5}$$

provided that the right term yields a negative value. Of course, the enthalpy flows of Eq. 3.6-5 entering/escaping from the system consist of contributions from solid, liquid and, unlike the system states '1' and '2', of gaseous components, though these contributions are not explicitly mentioned in the notation of the corresponding terms.

The heat sink at the pool boundaries due to sensible heat fluxes is,

$$Q_{By} = -\sum_{j_{ec}} Q_{j_{ec}} \tag{3.6-6}$$

Following the quantification of heat sinks, the amount of solid phases that stays mixed with the melt and of the solid phases that deposit as crusts along the pool boundaries can be obtained from,

$$m_{s,B} = m_{s,tot} \frac{Q_B}{Q_B + Q_{By}} \tag{3.6-7}$$

and

$$m_{s,By} = m_{s,tot} \frac{Q_{By}}{Q_B + Q_{By}} \tag{3.6-8}$$

respectively. $m_{s,tot}$ denotes the total solid phase inventory of the molten pool at state '2'. The solid which remains in the bulk translates into a bulk volumetric solid fraction. The liquid volume to calculate the solid fraction is obtained from the entire amount of liquid phases involved in the system.

Additionally, to determine the resulting crust depth and the corresponding thermal resistance, the modelling requires a spatial distribution of the solid phases over the cold boundaries of the pool. Breaking down the procedure given in Eq. 3.6-7 and 3.6-8 to that level, the solid phase mass deposited along the boundaries can be determined from the sensible heat passing through the respective surfaces, i.e.

$$m_{s,j_{ec}} = m_{s,By} \frac{Q_{j_{ec}}}{Q_{By}} \tag{3.6-9}$$

where 'j_{ec}' denotes the surface through which the heat is removed and $m_{s,j_{ec}}$ is the solid mass deposited on the considered surface.

The equivalent crust depth is finally obtained from the deposited solid, using the corresponding surface area and the solid phase density,

$$\delta_{Cr,j_{ec}} = \frac{m_{s,j_{ec}}}{\rho_s A_{j_{ec}}} \tag{3.6-10}$$

This transfers the pool as depicted in Fig. 3.6-3, into an encrusted condition as illustrated in Fig. 3.6-4.

The crust at the melt/concrete interface is assumed to be permeable for MCCI gases and for concrete decomposition products. This assumption is consistent with the outcome of the MACE-tests see e.g. [Farmer 1997], where the crust formed at the melt free surface due to flooding with water developed permeability for both, liquid and gaseous material.

Additionally, detail 'Z' of Fig. 3.6-4 indicates the temperature profile assumed between the bulk of the melt and the ablating concrete surface. This profile is fixed by the two known temperatures T_B and T_{dec} and the unknown interface temperature T_I.
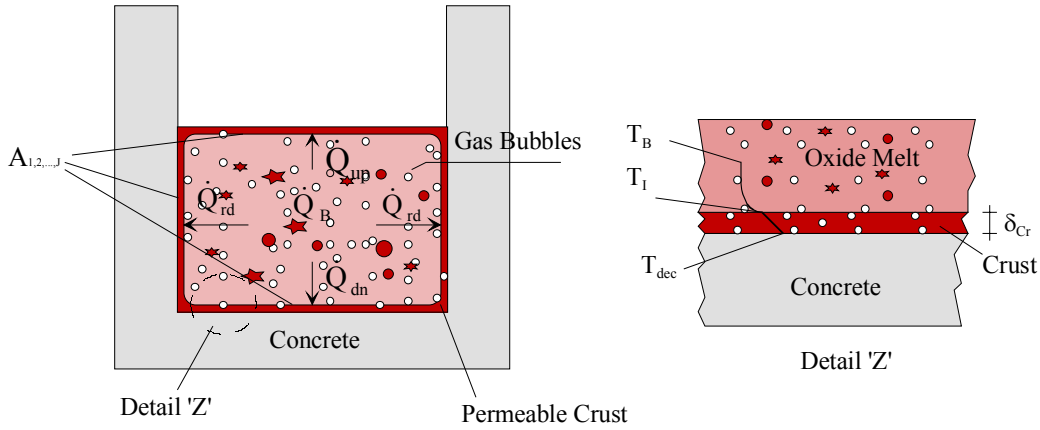
Fig. 3.6-4: *Encrusted MCCI pool as modelled for the calculation of heat transfer, $A_{1,2,...j}$ denotes the heat-transferring surfaces*

Since the interface temperature is unknown, the final task is to determine an effective thermal resistance for the heat transport from the bulk to the ablating concrete.

The governing equation for this heat transport is given as,

$$\dot{q}''_{dec} = \bar{h}_{dec}\left(T_B - T_{dec}\right) \tag{3.6-11}$$

where the heat transfer coefficient from the bulk to the ablating concrete surface, $\bar{h}_{dec}$, is obtained from a simple serial connection of the two individual heat resistances induced by the melt and crust,

$$\frac{1}{\bar{h}_{dec}} = \frac{1}{h_B} + \frac{\delta_{Cr}}{k_{Cr}} \tag{3.6-12}$$

In the same manner, the coefficient for heat transfer in upward direction can be determined from,

$$\frac{1}{\bar{h}_{up}} = \frac{1}{h_B} + \frac{\delta_{Cr}}{k_{Cr}} + \frac{1}{h_{out}} \tag{3.6-13}$$

The corresponding heat flux is,

$$\dot{q}''_{up} = \bar{h}_{up}\left(T_B - T_{out}\right) \tag{3.6-14}$$

where h_{out} characterises the heat transfer at the interface of the outer side of the crust and T_{out} is the temperature of the corresponding heat sink. Before layer inversion, h_{out} corresponds to the characteristics of heat transfer from the crust to the overlying metallic melt. For this particular situation, h_{out} is determined from Eq. 3.6-21. After layer inversion, or if the mixed model is used, h_{out} is determined based on the heat transfer conditions at the melt upper surface which is either thermal radiation as in the EPR, or, if this surface is flooded, boiling. Corresponding models are briefly discussed in Chap. 3.7.1. Analogously, given the situation that the metallic melt is underneath the oxidic one, the heat flux through the oxide/metal interface is also calculated using Eq. 3.6-14, where again Eq.3.6-21 is employed to determine h_{out}. Accordingly, T_{out} corresponds to the bulk temperature of the metallic melt.

The heat transfer coefficients at the melt/crust interfaces, h_B, are obtained from the correlations deduced from the experimental results of the BALI-tests [Bonnet 1999]. These test generically examined the heat transfer characteristics for MCCI conditions.

The principal advantage of these correlations is their large range of validity, since they were derived from experiments involving fluids with Pr-numbers from 7-2400 by increasing the viscosity to up to 100 times that of water. The viscosity increase was achieved by adding hydroxy-ethylcellulose (HEC) to the water which was used as working fluid. In contrast to metallic melts which have Pr-numbers in the range of 0.1, oxidic melts are covered by the Pr-range given above. The exact Pr-number depends on the duration of the MCCI and the type of concrete used. In general, the Pr-number increases in the course of an MCCI, given the relatively high specific heat of concrete and a potentially increasing viscosity. In contrast, the thermal conductivity which is the denominator of the Pr-number, is much less affected.

Moreover, the conditions in the BALI experiments largely correspond to the assumed MCCI conditions. In particular, the interface between the gas-evolving surface and the pool was formed of a crust consisting of solidified fluid. As a result of gas injection, the crusts developed a natural permeability.

The Nu-number for downward heat transfer coefficient has the form,

$$Nu_{dn} = 19.67 \left(\frac{\rho_M j_G^3}{\eta_M g} \right)^{0.136} Pr_M^{-0.22} \qquad (3.6-15)$$

where the Nu-number is defined as

$$Nu_{dn} = \frac{h_{dn} L_M}{k_M} \qquad (3.6-16)$$

Similarly, the Nu-number for heat transfer at the upper melt/crust interface can be obtained from,

$$Nu_{up} = 24.67 \left(\frac{\rho_M j_G^3}{\eta_M g} \right)^{0.063} Pr_M^{-0.29} \qquad (3.6-17)$$

The correlations including the constant coefficients and exponents were deduced from the experimental data obtained from the BALI-tests. Due to their generic character, the coefficients and exponents are not adjustable to specific MCCI experiments, but remain fixed.

The superficial gas velocity j_G of Eqs. 3.6-15 and 3.6-17 equals the volumetric gas flow divided by the cross-section of the gas-agitated area.

Eq. 3.6-15 and 3.6-17 are evaluated using the properties of the liquid pool combined with the effect of solid phases located in the bulk. The corresponding modelling of melt thermophysical properties is briefly outlined in Chap. 3.7.3.

The BALI correlations were derived on the basis of the power split presented in Fig. 3.6-2. Thus, both correlations yield similar heat transfer coefficients, if the superficial gas velocity exceeds ~1.5 cm/s. For the heat transfer in radial direction which was not investigated in the BALI tests, the correlation for downward heat transfer is used. This choice is not expected to

affect the radial erosion characteristics, given the high similarity between the BALI correlations for upward and downward heat transfer.

Prediction of the heat transfer coefficient at the melt/concrete interface, $\overline{h}_{dec}$, further requires to consider the correlation of the superficial gas velocity j_G of Eq. 3.6-15 with the concrete ablation rate. This is deduced from the general equations for predicting the ablation front progression, see Eq. 3.3-1 - Eq. 3.3-4 and is given as,

$$j_G = \frac{\xi_G \overline{h}_{dec}(T_B - T_{dec})}{\Delta e_{dec}\rho_G} \tag{3.6-18}$$

where ξ_G denotes the mass fraction of gaseous concrete decomposition products in the concrete. $\overline{h}_{dec}$ is eventually determined by combining Eqs. 3.6-12, 3.6-15 and Eq. 3.6-18.

The same modelling is also applied if the mixed mode assuming the melt as an intimate mixture of metallic and oxidic phases is applied. Due to its low-melting characteristic, it is assumed that the entire metallic melt in combination with those particular oxidic phases which are liquid establishes the liquid core of the pool. The pool boundary is formed of a crust predominantly consisting of the refractory core oxides UO_2 and ZrO_2. In addition, equivalent to pure oxidic melts, also for the mixed condition solid phases are modelled to stay mixed with the bulk. Corresponding thermal and transport properties of the melt used to evaluate the heat transfer equations take into account the presence of a miscibility gap. In particular, the properties of the individual liquid phases are combined to *mixed* properties using specific rules as given in Chap. 3.7.3.

In summary, the described new model is consistent as regards the melt solidification behaviour and its coupling with the thermal hydraulic conditions. Consequently, there exists no additional degree of freedom, which eliminates the possibility to use adjustable parameters. Further, it also contrasts with that pursued for metallic melts described in Chap. 3.6.3.

3.6.2.3 Calculation of concrete ablation rate for oxidic melts in COSACO

The essential task to calculate the concrete ablation rate constitutes the prediction of the crust depths at the individual pool boundaries. This task stringently follows the overall procedure to construct the time-dependent evolution of the MCCI. In particular, the integral change of state of the system from '1' to '2' arising within a certain period is modelled by integrating the energy balance equation using incremental time steps. The integration uses the current state of the system which includes the melt as well as the pool boundaries, as an initial condition for the next step.

The energy losses at the respective heat sinks of the pool cumulated from the onset of MCCI until the actual situation as well as the actual amount of solids constitute the essential prerequisites for calculating the crust depths. The cumulated energy losses are obtained from integrating the corresponding heat fluxes according to the general integration scheme. The total amount of solids is part of the actual thermochemical state of the melt. This state is obtained from solving the energy balance equation with respect to temperature under the condition that the temperature is consistent with the melt composition.

The energy losses and the actual amount solids are inserted into Eqs. 3.6-7 – 3.6-9. Given the allocation of the solids to the respective sinks, so-called *equivalent* crust depths are determined for the boundaries of the pool using Eq. 3.6-10. In contrast, solid phases which stay in the bulk correspond to a bulk volumetric solid fraction. This fraction is determined using the volume of the entire amount of liquid phases of the melt system which is also given by the melt thermochemical state.

Following the determination of the equivalent crust depths, the heat transfer coefficient at the melt concrete interface, $\overline{h}_{dec}$, is obtained by iteratively solving the combination of Eqs. 3.6-12, 3.6-15 and Eq. 3.6-18. The viscosity employed to evaluate the heat transfer coefficient at the melt/crust interface, h_B, takes into account the bulk volumetric solid fraction according to the model described in Chap. 3.7.3. Given $\overline{h}_{dec}$ as a function of the current state, the heat flux at the melt concrete/interface used for the next time step is calculated corresponding to Eq. 3.6-11 employing the actual melt temperature. The ablation rate of the next step is finally obtained from inserting the heat flux into Eq. 3.3-4.

3.6.3 Modelling of heat transfer for metallic MCCI pools

3.6.3.1   General

After layer inversion, potentially superheated metallic melt governs downward concrete ablation until it has cooled down to its steady state temperature. Corresponding transient concrete ablation by metallic melts is characterised by ablation rates which are up to one order of magnitude higher than those during steady state ablation, e.g. $3 \bullet 10^{-4}$ m/s vs. $5 \bullet 10^{-5}$ m/s. An additional, experimentally observed characteristic is the insensitivity of transient ablation rates towards melt temperature during the cool-down, as one can infer from Fig. 3.6-1 which shows the ablation front progression observed in the CORESA tests. In particular, despite the melt has cooled-down from 2000°C to 1600°C during the interaction with concrete, the ablation front progression is an almost linear function of time.

However, the existing models yield a significant correlation between melt temperature and ablation rate [Firnhaber 1992]. The consequence is an overprediction of transient ablation rates. Therefore, with view to reducing conservatisms in predicting concrete ablation, the task of this chapter is to provide a model which yields an improved agreement with the experimentally observed ablation characteristics.

Due to the principal suitability of the existing models to predict the phenomenology of melt concrete interactions with metallic melts, the following model builds on an existing phenomenological approach instead of being a completely new development. Specifically, the underlying approach rests on the assumption that a slag layer consisting of concrete decomposition products forms at the interface between the metallic melt and the concrete. A similar phenomenology is applied for modelling MCCI for both, metal as well as oxide melts in CORCON.

While specifically addressing transient concrete ablation, the resulting model is also valid for quasi-steady conditions. Equivalent to oxidic melts, the fundamental assumption of an

isotropic heat flux distribution is also used for metallic melts. Hence, the following model is used for both, the prediction of downward and sideward concrete ablation.

Aside from the heat transfer at the metal melt/concrete interface, the following chapter also provides a brief outline on the modelling of heat transfer between the metal melt and the overlying slag layer.

3.6.3.2 Modelling of heat transfer at the ablating concrete boundary

The modelling begins with the assumption that the heat transfer characteristics arising from the contact between the melt and concrete are analogous to those which would result if the melt was a solid body. Following contact, a slag layer consisting of concrete decomposition products is assumed to arise. The assumption of a slag layer is plausible, since the metallic melt and the oxidic concrete decomposition products are mutually imiscible.

The slag layer would stay in place if the metallic melt was solid. However, since the true state of the metallic melt is liquid and the concrete decomposition products are significantly lighter than the metallic melt, they buoy up almost concurrent with their formation and pass through the melt. After detachment, the melt again contacts a cold concrete surface. Fig. 3.6-5 depicts this cycle.
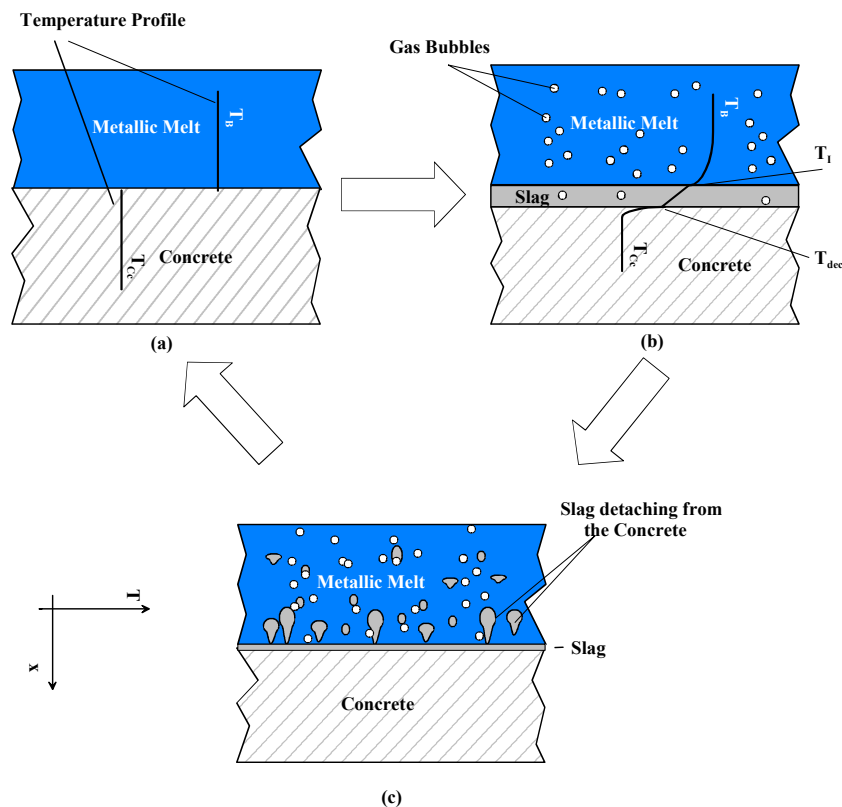

Fig. 3.6-5: *Assumed phenomenology of melt/concrete heat transfer for metallic melts*

The assumed phenomenology can be cast into the following set of equations. Given the temperature at the interface between the metal melt and slag layer, the heat flux from the molten pool to the slag/melt interface has the form,

$$\dot{q}''_{dec} = h_B (T_B - T_I) \tag{3.6-19}$$

As is indicated by the nomenclature of Eq. 3.6-19, the heat flux at the slag/melt interface directly translates into concrete ablation, implying that heat capacity effects of the slag layer are neglected and thus, the temperature profile across that layer is linear, see also Fig. 3.6-5.

The interface temperature T_I is obtained from solving the heat conduction equation for two semi-infinite solid slabs of different initial temperature attaining contact at a common interface,

$$T_I = \frac{\sqrt{k_{Cc}\rho_{Cc}c_{Cc}}\, T_{Cc} + \sqrt{k_M \rho_M c_M}\, T_B}{\sqrt{k_{Cc}\rho_{Cc}c_{Cc}} + \sqrt{k_M \rho_M c_M}} \tag{3.6-20}$$

where the concrete temperature T_{Cc} is taken as the ambient temperature of the concrete, i.e. 25°C, given the assumption that the melt always contacts cold concrete. Strictly, Eq. 3.6-20 is only valid for a stagnant melt pool corresponding to a solid body. In contrast, under MCCI conditions the pool is intensively agitated by gases which results in augmenting the heat transfer over the originally conduction-limited heat transfer employed to derive that equation. To take into account such augmentation, the molecular thermal conductivity k_M of the melt pool is replaced by an effective conductivity. For the present task, the effective value was empirically determined to be 10 times the theoretical one.

If Eq. 3.6-20 yields an interface temperature that is below the liquidus temperature of the metal melt, e.g. 1450°C, the interface temperature is taken equal to the liquidus temperature.

The bulk/interface heat transfer coefficient of Eq. 3.6-19 is obtained from the Kutateladze-correlation [Kutateladze 1978],

$$h_B = 1.5 \cdot 10^{-3} \frac{k_M}{L_M} \left(\frac{pc_M j_G}{k_M g} \right)^{2/3} ; \quad \frac{j_G \eta_M}{\sigma_M} \leq 4.3 \cdot 10^{-4}$$

$$h_B = 3.1 \cdot 10^{-5} \frac{k_M}{L_M} \left(\frac{pc_M j_G}{k_M g} \right)^{2/3} \left(\frac{j_G \eta_M}{\sigma_M} \right)^{-1/2} ; \quad 4.3 \cdot 10^{-4} < \frac{j_G \eta_M}{\sigma_M} \leq 10^{-2} \tag{3.6-21}$$

$$h_B = 3.1 \cdot 10^{-4} \frac{k_M}{L_M} \left(\frac{pc_M j_G}{k_M g} \right)^{2/3} ; \quad \frac{j_G \eta_M}{\sigma_M} > 10^{-2}$$

This correlation was developed to investigate boiling heat transfer and is among others supported by data on boiling sodium and boiling water, which are reflective for a Pr-number range from 0.004 to at least 2. Thus, the correlation is also representative for metallic melts, for which the Pr-number is typically around 0.1. In contrast, the BALI correlations, see Eq. 3.6-15, were derived for Pr-numbers $> \sim 7$ and thus do not apply to metallic melts. The underlying data for developing the Kutateladze-correlation was obtained from experiments involving rigid porous plates, through which gas was injected into a liquid pool with a predefined superficial gas velocity.

Equivalent to oxidic melts, also this model employs Eq. 3.6-18 to take into account the dependency of the superficial gas velocity on the ablation rate.

Following the development, the model is applied by way of example to generically evaluate the transient heat transfer characteristics for an MCCI involving siliceous concrete as given in Tab. 3.3-2 and a representative metallic melt. The pressure is assumed to be 1 bar.

Fig. 3.6-6 indicates that as long as the interface temperature is above the liquidus temperature, the heat transfer coefficient decreases with rising melt temperature, while at the same time the resulting heat flux increases. The decrease of heat transfer is attributed to the increasingly insulating effect of the slag layer which grows with rising heat flux at the melt/concrete interface. Clearly, the slag layer becomes the thicker the higher the ablation rate is and thus retards the increase in heat flux and, correspondingly, of ablation rate.
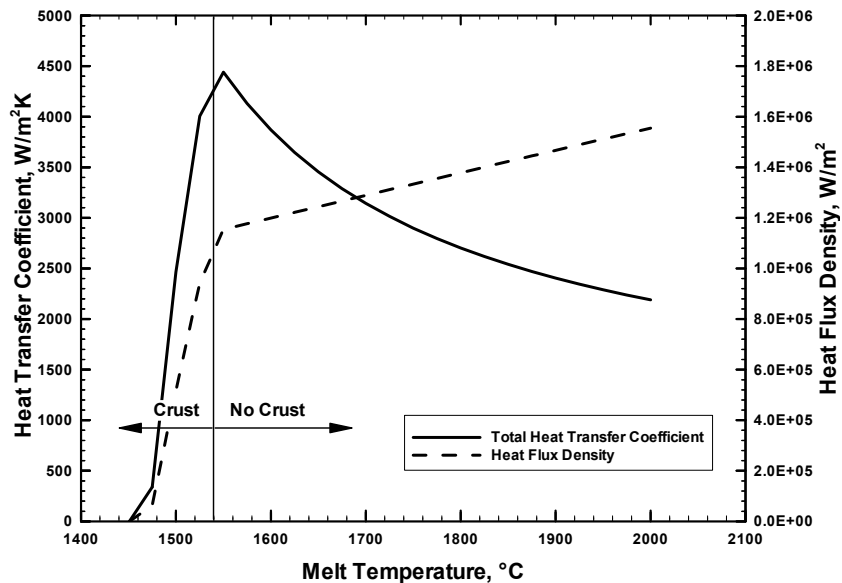

Fig. 3.6-6: *Heat transfer coefficient and corresponding heat flux density at the metallic melt-concrete interface*
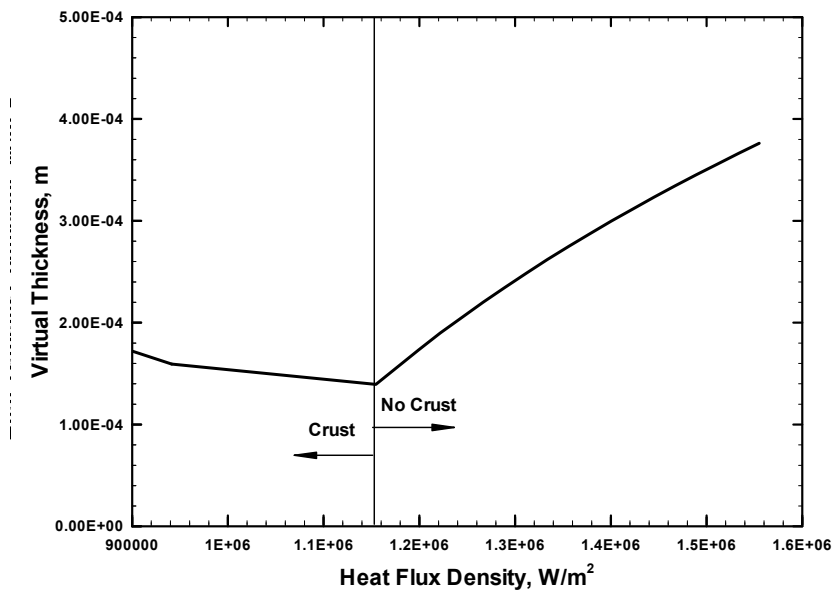

Fig. 3.6-7: *Virtual thickness of the slag layer plotted vs. heat flux density of Fig. 3.6-6*

Fig. 3.6-7 depicts this general behaviour using the following relation between thickness of the slag layer and heat flux,

$$\delta_{Sl} = \frac{k_{Sl}(T_I - T_{dec})}{\dot{q}''_{dec}}$$
(3.6-22)

To illustrate the general tendency rather than quantifying the thickness, the thermal conductivity of the slag employed to evaluate above equation was arbitrarily taken equal to unity. Therefore, the resulting thickness is denoted virtual.

When the interface temperature is predicted to fall short of the melt's liquidus temperature, which occurs at ~1530°C in this example, the interface temperature is kept constant at that temperature and consequently, the heat transfer characteristics change. The change manifests in a steep decline of both, heat transfer coefficient and heat flux, while at the same time the thickness of the slag layer increases.

In terms of heat transfer to the slag, the model developed by [Szekely 1963] is used. This theoretical model addresses the particular situation encountered in blast furnaces, where a metallic melt is covered by a slag layer. The model bases on a conduction analysis for two semi-infinite slabs attaining contact at a common interface. It factors in the periodic disruption of the evolving thermal boundary layer by gas bubbles passing through the interface.

The heat transfer at both, the slag and metal side of the interface has the form,

$$h = 1.69 k_M \sqrt{\frac{\dot{j}_G}{\frac{k_M}{\rho_M c_M} r_{eq}}}$$
(3.6-23)

where the equivalent radius of the gas bubble is [Blottner 1979],

$$r_{eq} = 3.97 L_M$$
(3.6-24)

The constant multiplier of Eq. 3.6-24 was deduced from experimental results.

Given the individual heat transfer coefficients of both sides of the metal/slag interface using the corresponding thermal properties, the overall heat transfer is determined from a serial connection of both heat transfer resistances.

At this stage of documentation, the key physics involved in the MCCI for both, oxidic and metallic melts as well as the corresponding model development is described. The next section briefly outlines further aspects of the MCCI which are generally important to close the modelling and which are specifically relevant to model the melt retention in the pit as well as experiments with respect to code validation. These are (i) the heat transfer conditions at the melt upper surface, (ii) melt volume increase due to MCCI gases, (iii) modelling of the melt thermal and transport properties of the melt as well as (iv) the representation of geometry.

3.7 Further modelling

3.7.1 Modelling of heat transfer at the melt's free surface

In terms of the melt retention in the reactor pit, the principal heat transfer mechanism at the melt free surface is radiant heat transfer to the remains of the reactor pressure vessel and to the concrete walls of the reactor pit located above the melt surface. Correspondingly, COSACO incorporates a model which specifically addresses the conditions relevant to the EPR.

On the other hand, in terms of validation, models are required to address test specific situations which deviate from those expected at reactor scale. In particular, in the MACE tests, against which the code is validated, the melt free surface was flooded with water. Consequently, the code also models boiling heat transfer.

In any case, heat removal at the melt free surface is determined by balancing the convective heat flux from the bulk with either the radiant or boiling heat flux,

$$\overline{h}\left(T_B - T_S\right) = \dot{q}''_{rad,boil} \tag{3.7-1}$$

In case the oxidic melt forms the free surface, $\overline{h}$ is determined corresponding to the logic developed in Chap. 3.6.2. In contrast, if the low-melting slag layer is at the free surface, $\overline{h}$ exclusively corresponds to the heat transfer coefficient of the BALI-correlation for upward heat transfer, see Eq. 3.6-17.

The radiant heat flux from the melt surface to the overlying hemisphere consists of a term for the heat transfer to the reactor pressure vessel plus a term for the transfer to the concrete above the melt,

$$\dot{q}''_{rad} = \varepsilon_S \sigma_{blz} \left(\varepsilon_{RV} \varphi_{S-RV} \left(T_S^{\,4} - T_{RV}^4\right) + \sum_{j_{ND}} \varepsilon_{Cc} \varphi_{S-j_{ND}} \left(T_S^4 - T_{dec}^4\right) \right) \tag{3.7-2}$$

In Eq. 3.7-2, index 'j_{ND}' denotes the jth node of the cavity wall exposed to radiation, see Fig. 3.7-1. Modelling of the viewfactor for the radiation heat exchange between melt surface and the reactor pressure vessel obeys the rule for two parallel circular surfaces centered on a common axis [VDI 1984],

$$\varphi_{S-RV} = \frac{1}{2R_1^2} \left(1 + R_1^2 + R_2^2 - \sqrt{\left(1 + R_1^2 + R_2^2\right)^2 - 4R_1^2 R_2^2} \right) \tag{3.7-3}$$

with

$$R_1 = \frac{r_S}{l_{S-RV}} \text{ and } R_2 = \frac{r_{RV}}{l_{S-RV}} \tag{3.7-4}$$

where R_1 denotes the larger and R_2 the smaller ratio.

The viewfactors between the surface and each of the upper nodes are determined utilising auxiliary surfaces, see Fig. 3.7-1.
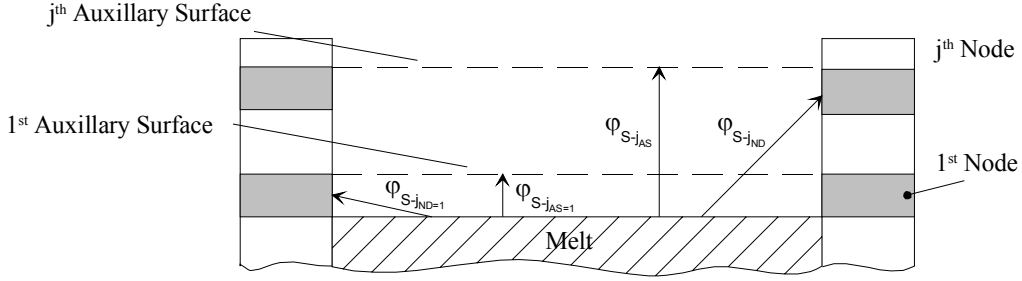
Fig. 3.7-1: *Calculation of viewfactors for the surface-to-pit radiant heat exchange*

Given the condition that the sum of the individual viewfactors for radiant heat exchange with the overlying hemisphere equals one, the viewfactors are determined successively starting with the first node,

$$\varphi_{S-j_{ND}=1} = 1 - \varphi_{S-j_{AS}=1} \tag{3.7-5}$$

The subsequent nodes are determined employing the following expression,

$$\varphi_{S-j_{ND}} = 1 - \varphi_{S-j_{AS}} - \sum_{h_{ND}=1}^{j_{ND}-1} \varphi_{S-h_{ND}} \tag{3.7-6}$$

where $\varphi_{S-j_{AS}}$ is evaluated with Eq. 3.7-3 and $j_{AS} = j_{ND}$.

To determine the temperatures of the bodies being involved in the heat exchange with the free surface, the RPV is modelled as a lumped system with mass, material and initial temperature specified by the user. The heat-up of the reactor pressure vessel is governed by radiant heat emitted from the melt surface according to

$$\frac{d(m_{RV}e_{RV})}{dt} = \dot{Q}_{rad} \tag{3.7-7}$$

The surface of the concrete exposed to radiant heat transfer is assumed to be at uniform, constant temperature. If this temperature is the concrete decomposition temperature, the radiant heat flux decomposes the concrete with a rate proportional to the heat flux density.

When water is present at the melt free surface, the modelling considers film boiling for saturated water pools. Behrenson's heat transfer coefficient (see [Rohsenow 1973]), used to describe this regime is itself a function of the driving temperature difference.

$$h_{cd} = 0.425 \left(\frac{k_V^3 \rho_V (\rho_W - \rho_V) g (\Delta e_W + 0.4 c_{pV} \Delta T)}{\eta_V L \Delta T} \right)^{0.25} \tag{3.7-8}$$

Thermal radiation which passes through the vapour film, augments the originally conduction limited heat transfer, particularly at high temperature differences. Accordingly, a radiant heat transfer coefficient is introduced,

$$h_{rad} = \frac{1}{1/\varepsilon_S + 1/\varepsilon_W - 1} \sigma_{blz} \frac{\left(T_S^4 - T_{sat}^4\right)}{T_S - T_{sat}} \tag{3.7-9}$$

The overall heat transfer coefficient is obtained by superposition of the conduction and the radiation transfer coefficient,

$$h_{film} = h_{rad} + h_{cd} \tag{3.7-10}$$

and the heat flux is,

$$\dot{q}''_{boil} = h_{film}(T_S - T_{sat}) \tag{3.7-11}$$

Film-boiling heat transfer is further augmented by MCCI gases passing through the vapour film which increase the area of the involved surfaces. This effect is addressed using a surface enhancement factor [Farmer 1990] which relates the increased surface to the originally flat surface,

$$A/A_{fl} = 1 + 4.5\, j_G /U_t \tag{3.7-12}$$

The total film-boiling heat transfer coefficient is finally obtained from multiplying Eq. 3.7-10 with Eq. 3.7-12.

3.7.2 Melt volume increase by decomposition gases

When gas sparges through a melt pool, the surface level of the resulting gas-melt mixture increases over the collapsed volume of the melt to accommodate the gas. The ratio of the arising gas volume to the total melt volume, i.e. the collapsed volume of the melt plus that of the gas, is denoted melt void fraction. The significance is its impact on the energy balance of the melt pool as heat removal to the concrete sidewalls is increased due to an increase in the sidewall surface area in comparison to an unsparged pool. The melt void fraction can be potentially determined from several different correlations. The particular one incorporated in COSACO is that developed by Zuber and Findlay [Wallis 1969] based on the drift flux model,

$$\alpha = \frac{j_G}{j_G + U_t} \tag{3.7-13}$$

The terminal rise velocity of the bubble is evaluated using a model given in [Blottner 1979],

$$U_t = 1.53\sqrt{\frac{\sigma_M}{\rho_M L_M}} \tag{3.7-14}$$

The void fraction is limited to 0.42, since beyond this threshold jets will likely develop [Blottner 1979].

3.7.3 Mixture rules to determine the properties of multi-component melts

The essential prerequisite to predict mixture properties of a multi-component melt is its thermochemical state which determines the distribution of the individual components on the liquid and solid phases. Correspondingly, models are applied which allow predicting the properties of the solid and liquid mixture phases from the properties of the individual components. However, the properties of the various types of solid phases which may coexist in the melt are not determined individually. Instead, all solid phases are rendered in one solid phase of mean composition, for which the properties are finally determined. If solid and liquid phases coexist, e.g. in the bulk of the oxidic melt, the corresponding solid and phase properties are combined to so-called *slurry* properties.

While density, specific heat and thermal conductivity are evaluated from ordinary mixture rules, prediction of viscosity, particularly of oxidic melts, is rather complicated and thus is discussed more thoroughly.

In contrast to the viscosity of steel melts which is dominated by Fe as the main component and thus can be represented by a simple correlation developed for melted iron (see e.g. [Brandes 1983]), the viscosity of oxidic melts is highly sensitive to the effect of specific melt components. Probably the most complete model for determining the viscosity of oxidic melts formed of liquid phases has been developed by Urbain [Urbain 1987]. This model is a function of temperature and composition that takes into account interactions between the melt components on a molecular level. Due to this approach, it covers a vast amount of constituents exhibiting either a glass-forming or liquefying character. At the same time, it is applicable to a broad spectrum of melt compositions and is thus particularly useful for modelling MCCI.

The model is based on a classification of melt constituents as (i) glass formers, (ii) modifiers and (iii) amphoterics. *Glass formers* highly increase the viscosity due to their strong covalent bonds. The group of glass formers contains SiO_2 and B_2O_3. The group of *modifiers* represents the mono-, bi- and trivalent metallic cations that form a compound with oxygen, i.e. UO_2, ZrO_2, CaO, Cr_2O_3 and FeO. All these components decrease the melt viscosity. *Amphoterics* only comprises the trivalent compounds Al_2O_3 and Fe_2O_3 which behave as either glass formers or modifiers.

Urbain [Urbain 1987] proposed the following Ahrrenius-type approach to determine the liquid phase viscosity,

$$\eta_l = 10^{-1} z_1 T \cdot e^{10^3 z_2 / T} \qquad (3.7\text{-}15)$$

where z_1 and z_2 are linked through the following equation,

$$z_1 = e^{-(0.2693 z_2 + 11.6725)} \qquad (3.7\text{-}16)$$

The constant coefficients 0.2693 and 11.6725 in the exponent of Eq. 3.7-16 are valid for molar concentrations of glass formers< 85 wt%. To estimate the viscosity of melts with higher fractions of glass formers, these coefficients have to be substituted by 0.207 and 10.28, respectively. The parameter z_1 is a function of the equivalent molar concentration of the three groups and can be obtained from Fig. 3.7-2. The equivalent mole of the individual glass-forming compounds used to determine the molar concentration takes into account the charge potential of the respective cation of the molecule, i.e. Si^{4+} and B^{3+} which is 1 and 4/3. It is evaluated with the following two relations for SiO_2 and B_2O_3,

$$n_{SiO_2,eq} = 1 \cdot 1 \cdot n_{SiO_2}$$

$$n_{B_2O_3,eq} = 2 \cdot 4/3\, n_{B_2O_3}$$

The modifier mole equivalent is simply obtained by multiplying the stoichiometric mole with the number of oxygen atoms bound in the molecule, i.e.

$$n_{UO_2,eq} = 2 \cdot n_{UO_2} \qquad n_{CaO,eq} = n_{CaO}$$

$$n_{ZrO_2,eq} = 2 \cdot n_{ZrO_2} \qquad n_{Cr_2O_3,eq} = 3 \cdot n_{Cr_2O_3}$$

while the amphoteric mole equivalent equals the stochiometric mole,

$$n_{Fe_2O_3,eq} = n_{Fe_2O_3}$$

$$n_{Al_2O_3,eq} = n_{Al_2O_3}$$

Given the equivalent moles, the equivalent molar fraction is determined from,

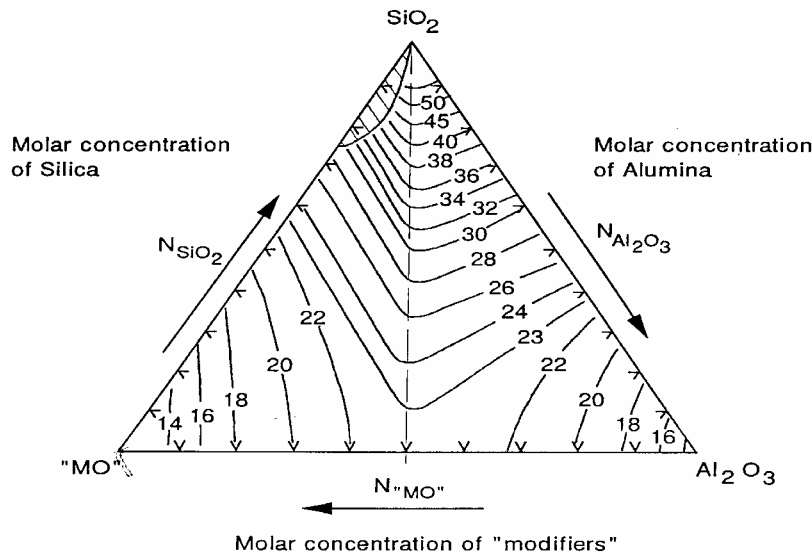$$\psi_{i,eq} = \frac{n_{i,eq}}{\sum_i n_{i,eq}} \qquad (3.7\text{-}17)$$

Fig. 3.7-2: *Parameter z_2 map [Urbain 1987]. Alumina represents all amphoterics, silica all glass formers. N constitutes the equivalent molar fraction calculated according to Eq. 3.7-17*

If solid phases build up in the melt, the viscosity increases over the level that arises if the melt exclusively consists of liquid phases and which is described by the Urbain model. There exist several approaches to model the resulting, so-called *slurry* viscosity, e.g. [Stedman 1990]. However, the use of these particular correlations is restricted to suspensions of spherical particles. Additionally, these spheres are assumed to be inert towards the ambient liquid. Therefore, COSACO makes use of an alternative model [Ramaciotti 1999] which takes into account chemically interacting solid and liquid phases. This model modifies the liquid phase viscosity by a multiplier of exponential form,

$$\eta_{su} = \eta_l \exp(2.5z_3\zeta_s) \qquad (3.7\text{-}18)$$

As is evident from that expression, the exponent consists of the volumetric solid fraction ζ_s and a parameter z_3 reflecting the uncertainties involved in determining the viscosity. This empirical parameter is a function of composition and has to be deduced from experiments. The suggested range is from ~4 to ~8. A more precise selection is not plausible due to the fairly small amount of reliable experimental viscosity data for such complex, solidifying

mixtures. Additionally, the value can depend on the cooling rate or effects induced by the measurement technique. For corium-concrete mixtures as investigated by e.g. [Roche 1994], z_3 varies between ~4.8 and ~5.5. Since these mixtures are in reasonable agreement with those anticipated for the EPR, the parameter is selected accordingly.

In case the oxidic melt is assumed to be intimately mixed with the metallic melt due to a postulated intense agitation of the pool by MCCI gases bubble agitation, the viscosity of such system is calculated using a model described in [Wallis 1969],

$$\eta_{mx} = \eta_1 \left(1 + 2.5 \frac{\eta_2 + 0.4\eta_1}{\eta_2 + \eta_1} \frac{V_2}{V_1 + V_2} \right) \tag{3.7-19}$$

where the indices '1' and '2' denote the two fluids, i.e. the oxidic and metallic melt. This expression has only been derived for smaller fractions of liquid '2' (< 5 vol%). Thus, for higher fractions of either liquid, the viscosity is estimated by linearly interpolating between the bounding values, given by a volume fraction of 5 vol% of either liquid '1' or liquid '2'.

The density of the melt composed of several liquid and solid components is determined assuming that the volumes of all individual components add to the total volume,

$$\rho = \frac{1}{\frac{1}{m} \sum_i \frac{m_i}{\rho_i}} \tag{3.7-20}$$

The specific heat is merely used to evaluate the heat transfer correlations, while the temperature is determined from the melt enthalpy in combination with the melt thermochemical state. It is determined from averaging the contributions of the individual solid and liquid phase components by weight,

$$c = \frac{1}{m} \sum_i m_i c_i \tag{3.7-21}$$

Estimation of the thermal conductivity uses a serial connection of the individual thermal resistances [Artnik 1995],

$$k = \frac{1}{\frac{\rho}{m} \sum_i \frac{m_i}{\rho_i k_i}} \tag{3.7-22}$$

If the oxidic and metallic melts are assumed to be mixed, the following expression is used to quantify the thermal conductivity [Schulz 1975],

$$\left((1 - \zeta_2)(k_2 - k_1) \right)^3 = (k_2 - k_1)^3 \frac{k_1}{k_{mx}} \tag{3.7-23}$$

where the indices '1' and '2' denote the two fluids, i.e. the oxidic and metallic melt.

3.7.4 Geometry model

The walls of the cavity are divided into equidistant annular nodes. Starting from the initial shape (defined by the tilt angle, outer radius, minimum radius and concrete layer thickness) a

new shape is determined after every timestep, dependent on the actual ablation rate of each node. The volume required to accommodate the melt as well as the MCCI gases is dynamically adjusted corresponding to the change of volume of the melt/gas mixture. Fig. 3.7-3 illustrates the modelling of the cavity geometry.
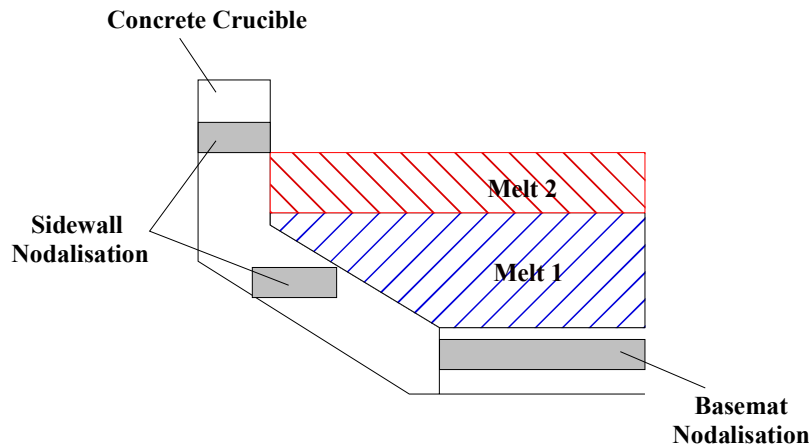

Fig. 3.7-3: *Geometrical model of the reactor cavity*

The volume occupied by the melt as well as the heat transfer surfaces of the melt/concrete boundary are calculated according to the rules for rotational-symmetric bodies.

3.8 The MCCI code COSACO

Following the model development, this chapter outlines the general features of COSACO, including input data to execute a calculation and the output.

The general framework of COSACO builds on real solution thermochemistry using the database COSCHEM described in Chap. 3.4.4. The database is incorporated into the logic of the code employing the thermochemical equilibrium solver CHEMAPP.

Thermochemistry is consistently linked with the energy balance and with the pool thermal hydraulics. This means that the temperature as determined from the energy conservation equation stringently correlates with the melt thermochemical state. Clearly, the melt thermochemical state is determined from the integral melt composition for a given temperature. On the other hand, the temperature is not an independent variable but is a function of the pool specific enthalpy resulting from the energy conservation equation. This equation includes terms that take into account the characteristics of heat and mass transfer within the MCCI pool. Again, these characteristics highly correlate with the thermochemical state of the melt. Addressing this mutual dependency is the principal feature of COSACO.

In practice, the numerical approach for integrating the energy conservation equation and the mass balance equation is a simple single step method with a user-defined fixed width of the time step. The reason for using a fixed width is that physical criteria for a time step control could not be identified. In addition, several plant specific calculations as well as post-test calculations of experiments revealed that the results are highly insensitive against the time step width due to the high inertia of the MCCI system. The energy conservation equation is formulated using heat transfer characteristics calculated on the basis of the melt

thermochemical conditions of the preceding time step. Consequently, determination of the actual concrete ablation, and thus, the actual mass transfer within the pool rests on heat transfer coefficients of the preceeding state of the pool. The actual thermochemical state is determined by iteratively solving the energy balance equation with respect to temperature using the actual melt composition. In parallel, a thermochemical equilibrium calculation is conducted at every iteration step. To this end, the Pegasus method is used which, unlike other methods, does not demand an explicit function.

The thermophysical properties of the individual melt components as a function of temperature required to evaluate the heat transfer characteristics as well as to solve the energy conservation equation, are stored in a separate routine. The properties of the melt are determined based on the thermochemical state using the mixture rules outlined in Chap. 3.7.3. Due to the outlined normalising procedure of specific enthalpies to enable implicitly modelling chemical reactions, the code maintains the system energy throughout the calculation. This means that the end state energy of the system equals the initial energy content plus the decay heat generated in the corresponding period. The system energy comprises contributions from the sacrificial concrete, the melt, as well as from the reactor pressure vessel remains. The loss of mass is only a few grams for a plant specific calculation.

The code is programmed in FORTRAN 90. The modular structure allows to easily replace/add models if felt necessary.

In conclusion, the outlined procedure is considered adequate to provide general consistency between the thermochemical state and mass and heat transfer characteristics for the MCCI system.

Execution of a calculation requires specification of the following parameters:

The geometry of the reactor pit is defined by the thickness of the concrete basemat and of the vertical concrete sidewalls as well as by its dimensions. These are the height of the pit, the diameter of the basemat, maximum diameter and the tilt angle of the inclined sidewalls. Additionally, the level and the radius of the reactor pressure vessel are required for calculating radiant heat transfer at the melt free surface.

The melt initial conditions involve mass, composition and initial temperature. The input allows to assign all melt components modelled in the thermochemical database COSCHEM to both, the metallic and oxidic melt. Clearly, specification of the oxidic melt may also include metallic components, while the metallic melt can initially also contain oxidic melt components. Further, the user can choose between the layered and the mixed representation of the melt pool. If the layered option is chosen, COSACO conducts a thermochemical equilibrium calculation for each melt independently to determine their proper initial thermochemical states. Conversely, in case of the mixed mode, COSACO mixes the specified melts which includes determination of the thermochemical state of the mixture as well as the arising mixing temperature.

Specification of the concrete requires selecting the type and amount of cement in the dry concrete mixture. Correspondingly, COSACO contains the built-in compositions of Portland and Tonerde cement as given in Tab. 3.3-1. Further, the integral chemical composition

comprising the concrete components SiO_2, Fe_2O_3, CaO, Al_2O_3, H_2O and CO_2 must be specified. Given the concrete composition and the selection of cement, the concrete decomposition temperature and enthalpy is determined according to the model developed in Chap. 3.3.2. Additionally, the density is required to calculate the weight of the concrete embedded in the reactor pit as well as the concrete ablation rate.

The decay heat in the oxidic and in the metallic melt is defined by a set of data points vs. time, between which is linearly interpolated. The decay heat can also attain negative values, which corresponds to simulating a heat sink. This possibility is relevant for recalculating experiments.

Further, the user can select between radiant and boiling heat transfer at the melt free surface, dependent on whether the melt upper surface is dry or wet. If radiant heat transfer is chosen, the mass, type of material and initial temperature of the reactor pressure vessel remains must be specified. Further, both models require specification of emissivities of the involved surfaces. If wet conditions are selected, the user can determine the time at which flooding of the melt surface is initiated.

In terms of investigating the temporary melt retention in the reactor pit, the user can additionally determine a temperature-dependent failure criterion of the reactor pressure vessel remains. These remains can be heated by residual melt located in-vessel in addition to radiant heat emitted from the MCCI pool. Upon failure, the reactor pressure vessel remains fall into the MCCI pool with the specific enthalpy corresponding to the state at failure temperature. At the same time, also the residual melt discharges into the MCCI pool. This melt comprises an oxidic and a metallic part which are separately defined by temperature and composition. Correspondingly, the thermochemical states of the melts and thus the specific enthalpies, at which they are released into the MCCI system, are given. As an alternative option, the residual melt can also be released according to a user-defined inflow history.

The output provides all relevant parameters of the involved melt layers and structures as a function of time to examine the MCCI and to conduct plausibility checks. At first, these are melt temperature as well as solidus and liquidus temperature, ablation depth and the evolution of the contour of the pit. In terms of thermophysical properties, density, specific heat, thermal conductivity and viscosity are registered. To evaluate the solidification behaviour as well as the heat transfer characteristics of the oxidic melt, the code calculates the volumetric solid fraction, and the equivalent crust depths at the boundaries of the pool. In terms of melt composition, the masses of the individual melt components and their distribution on the solid and liquid phases are stored. Further, one gets the actual and time-dependent integrated heat fluxes at the boundaries of the individual melt layers and the surfaces of the corresponding boundaries.

In terms of radiant heat transfer at the melt free surface, the heat fluxes to the reactor pressure vessel and to the dry walls of the pit and, accordingly, their cumulated values are determined. In addition, COSACO records the viewfactors to the reactor pressure vessel and to the concrete walls to allow plausibility checks.

For containment analyses, the evolution of mass release of CO_2, CO, H_2O and H_2 is registered.

COSACO is relatively fast running and easy to use. Thus, the code is well suited for performing parametric calculations to investigate the effect of selected variable changes on the overall course of the MCCI for realistic plant specific sequences. Additionally, it can be used to thoroughly investigate thermochemical phenomena involved in MCCI tests, apart from thermal hydraulic aspects.

Chapter 4
Validation of COSACO against selected MCCI experiments

4.1 Introduction

A substantial part of the COSACO development is devoted to the validation of the code against representative experiments. In this respect, this chapter presents post test calculations of selected tests involving prototypic oxidic corium as well as steel melts with COSACO. The tests were selected in the sense that they do not involve significant uncertainties in the experimental results due to specific experimentally induced effects.

In this manner, the MACE tests M3b and M4 were chosen as oxide tests due to their high quality with regard to the experimental conduct and the test's outcome. In particular, in both tests a thermite reaction instantaneously provided the melt and thus reduced the experimental uncertainties involved in the melt generation phase. Aside from the relatively high quality of temperature measurements, direct electrical heating as used in MACE to simulate decay heat enables to relatively precisely quantify the power that is deposited in the melt.

In contrast, other experiments, i.e. the SURC1/2 tests, see e.g. [Copus 1992], as well as the MACE test M1b [Farmer 1992] were found inappropriate for validation, as, among other experimental distortions, the melt was generated by heating a powder mixture for a couple of hours. As a result, also the concrete basemat was preheated and thus was weakened before concrete ablation commenced. In addition, M1b involved Zr-inserts in the concrete basemat, which are considered to have significantly influenced the ablation behaviour. Unfortunately, the MACE scoping test M0 [Spencer 1991] dominantly served to test experimental techniques and correspondingly was too weakly instrumented to enable validation of codes.

Nevertheless, validation against M3b and M4 is deemed to be sufficient to identify the inherent characteristics involved in the MCCI which are instrumental to demonstrate the viability of the melt retention in the reactor pit. The reason is that these tests investigated different types of concrete, i.e. limestone common sand vs. siliceous at different scale involving different power histories. Further, the duration of these tests was unlike that of the ACE experiments [Thomson 1997] fairly long. Therefore, the influence of test-specific effects arising during the initial phase becomes insignificant for the most part of the test duration.

In terms of tests conducted with metal melts, the CORESA 2.1 and the SURC 4 tests were employed to validate the code. While the CORESA 2.1 test specifically focussed on the transient ablation characteristics in a 2D geometry, the SURC 4 involved Zr-metal to identify the occurrence and the effect of condensed phase chemical reactions on the MCCI characteristics.

Since these experiments involve a variety of thermochemical effects they are considered adequate to examine the feasibility of the consistent modelling approach realised in COSACO. Additionally, since three different types of concrete, i.e. LCS concrete in M3b and CORESA 2.1, siliceous concrete in M4 and basaltic concrete in SURC 4 were employed in the tests, this selection offers the opportunity to examine the validity of the modelling also with respect to the type of concrete.

A successful validation against the oxide tests provided, the results for the principal experimental parameters ablation front progression and temperature are then used to develop a rationale for the expected inherent characteristics of the MCCI.

For all tests, the experimenter's best estimates of net input power, initial melt composition, and initial melt temperature were used in the calculations.

4.2 MACE tests

These tests were conducted to investigate the potential to terminate an MCCI by flooding the melt free surface. M3b [Farmer 1997] examined the interaction between fully oxidised PWR corium and limestone/sand concrete, while M4 [Farmer 1999] employed the same corium, but siliceous concrete.
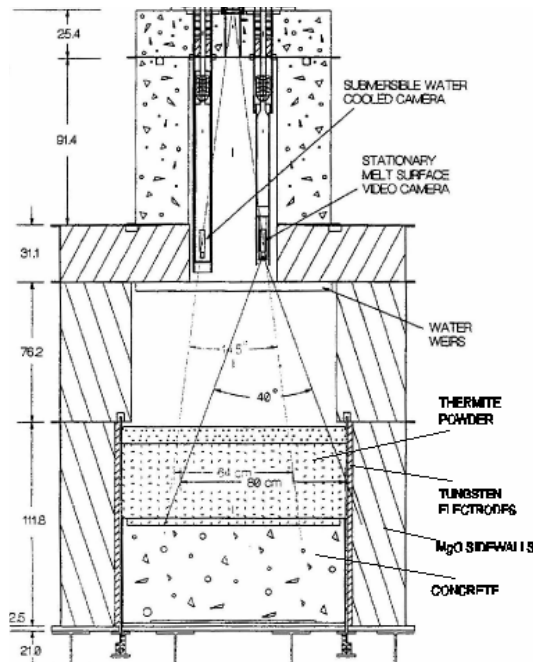

Fig. 4.2-1: *Experimental apparatus of M3b*

Both tests were conducted in a 1D geometry that consisted of a rectangular concrete basemat enclosed by inert MgO-sidewalls. The apparatus of M3b is presented in Fig. 4.2-1, while that

of M4 is neglected here due to the great similarity with that of M3b. The two opposite electrodes used to directly heat the melt, were mounted flush to the sidewalls.

4.2.1   MACE test M3b

The M3b test was conducted with an initial melt charge of 1790 kg corium which had the following composition.

Component	wt%
UO_2	57
ZrO_2	29
SiO_2	3.6
CaO	2.7
MgO	1.6
Al_2O_3	0.4
Cr	5.7

Tab. 4.2-1: *Initial melt composition of M3b*

The metallic Cr contained in the initial corium mixture was a by-product of the thermite reaction. The basemat fabricated of limestone common sand concrete measured $1.2 \times 1.2 \text{ m}^2$. The concrete composition is listed in Tab. 3.3-2.

As Fig. 4.2-2 reveals, the power input ranged from 220 kW to 390 kW.
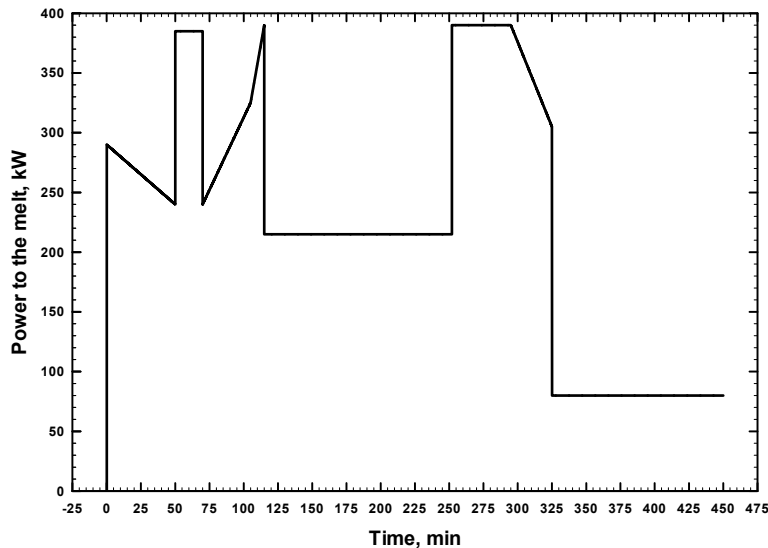
Fig. 4.2-2: *M3b – Power to the melt vs. time*

The heat losses into the side walls were deemed to be negligible. As a result of flooding of the melt surface after 52 min into the test, ~750 kg of melt were estimated to be ejected from the molten pool into the overlying water layer.

To assess the effect of this phenomenon on the main experimental parameters melt temperature and ablation front progression, two enveloping calculations were carried out. Case '1' employs the full initial corium charge until termination of the test which constitutes the upper bound for melt inventory. In contrast, case '2' constituting the lower bound,

employs a melt inventory which was reduced by 750 kg at the time of flooding. Since COSACO does not incorporate an ejection model, the mass was taken out of the mass balance at the time the melt was flooded.

Fig. 4.2-3a/b compare the calculated temperatures with the experimental data for both cases.

For case '1' as well as for case '2', the calculated behaviour of melt temperature is in good agreement with the experimental observation. In particular, the temperatures are predicted to decrease only modestly during the test. In terms of absolute temperature, case '1' overpredicts the temperature of the phase following flooding by ~100°C, while the results of case '2' are well in line with the experimental temperature.

The temperature during the initial phase is slightly overpredicted, due to the calculated high initial solid fraction in the melt, see Fig. 4.2-6. The high content of solids causes an initial heat-up to reduce the thermal resistances for transferring the decay heat to the concrete and for removing heat from the melt free surface.

The final transient after a sharp power reduction at 325 min is quantitatively inconsistent with the experimental data. This is attributed to eruptive events during the high power phase which reduced the melt mass involved in the experiment and thus affected the transient cool-down of the melt. COSACO does not include a corresponding melt ejection model.

The predicted decrease of liquidus temperature is attributed to the continuous dilution of the core oxides with concrete decomposition products.
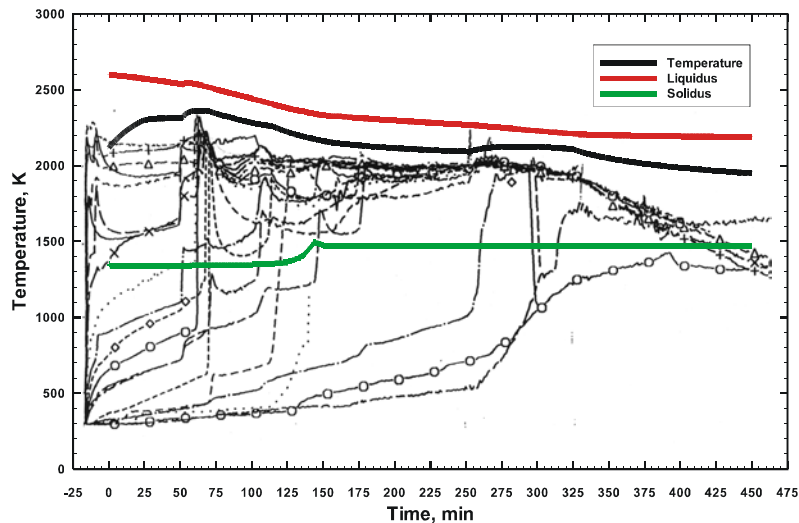

Fig. 4.2-3a: *M3b - Predicted melt temperature for case '1'*
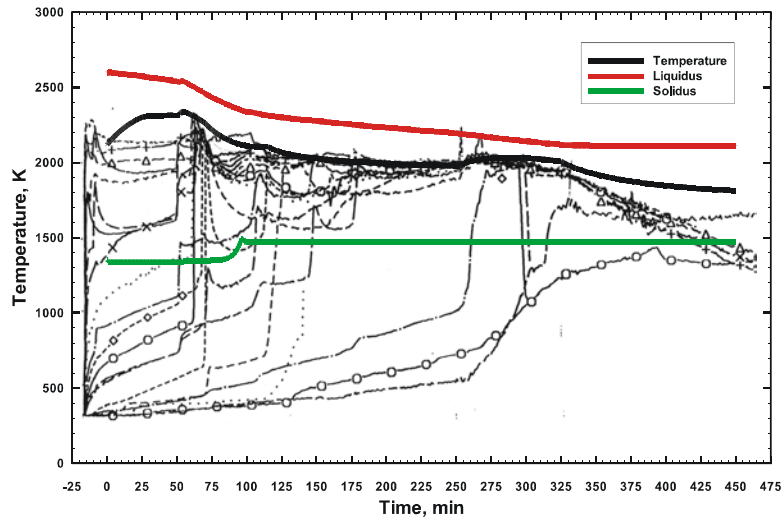
Fig. 4.2-3b: *M3b - Predicted melt temperature for case '2'. 0 min indicates the start of concrete ablation*

The general difference of temperature between case '1' and case '2' is attributed to the greater dilution of the refractory UO_2-ZrO_2 component by concrete decomposition products during the ongoing MCCI for case '2'. As is evident from Fig. 4.2-4, for same ablation depths corresponding to equal amounts of concrete mixed with the melt, a lower liquidus temperature and consequently, a lower melt temperature arises.
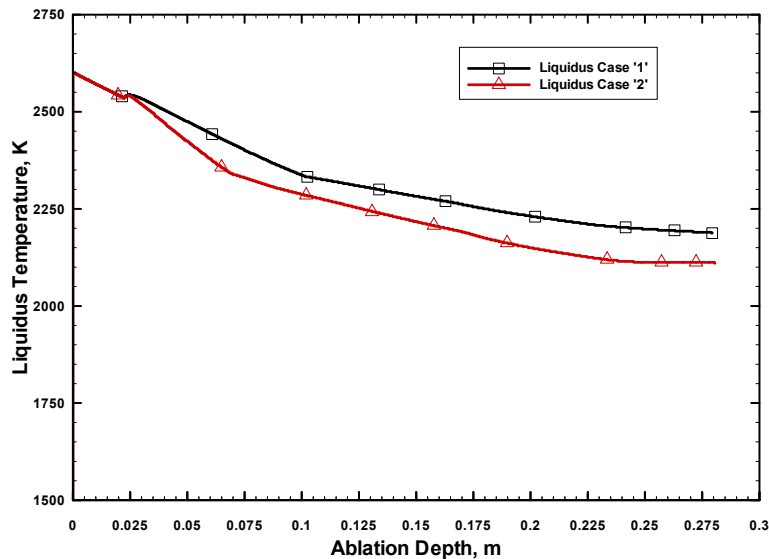
Fig. 4.2-4: *M3b – Calculated liquidus temperature vs. ablation depth for case '1' and case '2'*

However, the melt temperature difference between the two cases does not correspond to the difference between the liquidus temperatures. While at e.g. 250 min the predicted difference of the liquidus temperatures amounts to 76 K, the difference between the melt temperatures is equal to 116 K. This effect is attributed to the solidification behaviour which has changed disproportionally to the liquidus temperature and thus has resulted in decreasing the melt temperature over the expected level. Fig. 4.2-5 reflects this change by comparing the

solidification behaviour represented by the volumetric solid fraction as a function of temperature for the two cases. The melt compositions correspond to the state immediately before power increase.
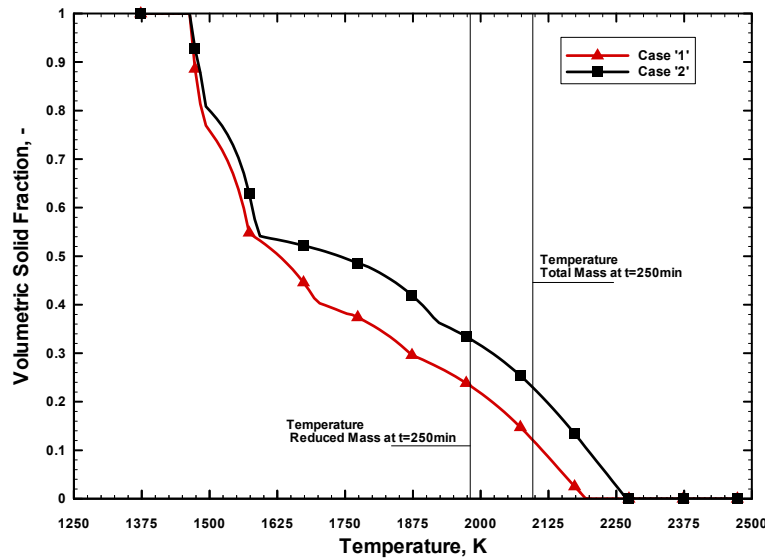

Fig. 4.2-5: *M3b – Calculated volumetric solid fraction vs. temperature of the melt compositions at t=250 min for case '1' and case '2'*

Aside from the solidification behaviour, Fig. 4.2-5 also indicates the melt temperature at 250 min which is 2100 K for case '1' and 1984 K for case '2'. Notably, both temperatures correspond to equal volumetric solid fractions of ~23%. Consequently, if the solidification curves were not diverging but parallel, the temperature difference would correspond to the difference of liquidus temperature.

The important result that the resulting solid fractions are similar, indicates that the volumetric solid fraction is not governed by the composition of the melt. The determining parameter will be identified based on assessing the time-dependent evolution of the volumetric solid fraction.

Fig. 4.2-6 presents the volumetric solid fraction and the resulting equivalent crust depths at the melt/concrete interface and at the melt upper surface. For the given initial melt temperature of ~2100 K, the total volumetric solid fraction is calculated to be 75%, while the volumetric solid fraction in the bulk amounts to ~50%. Assuming the correctness of these values, the initial state of the M3b melt is almost solid. The total volumetric solid fraction of the melt declines to 25% until power increase at 250 min irrespective of the corium mass present in the test. During the same period, the solid fraction of the bulk reduces to 6%.

Doubling of the power gives rise to almost isothermal melting of the solid phases. Both, the solid fraction of the bulk as well as the total fraction decline by ~50% to 3% and 13%, respectively. After power reduction at 325 min, the solid fraction attains again the value before the power was increased.

The consequences of the power increase indicate that the volumetric solid fraction is significantly affected by the power supply to the melt. For both cases, a reduction of 50% is predicted which corresponds to the power increase in similar order. Further, the high

predicted similarity for both cases supports the assumption that the solid fraction develops fairly independently of the melt composition.
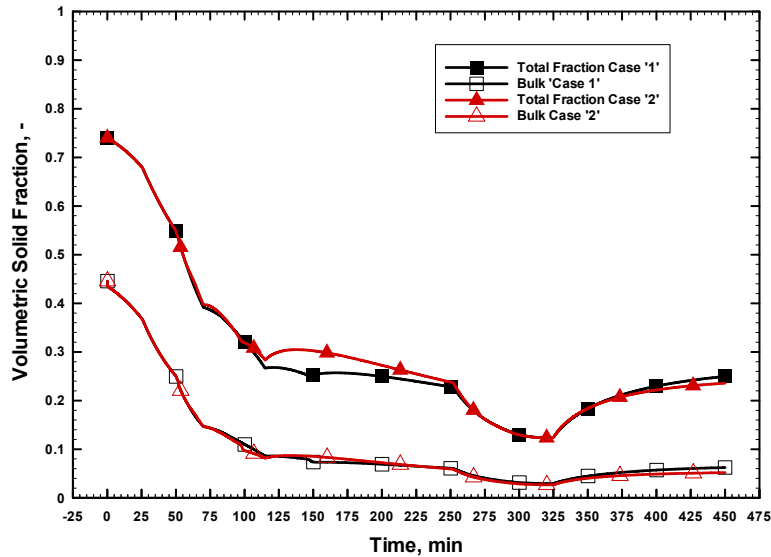

Fig. 4.2-6a: *M3b – Calculated total volumetric solid fraction and volumetric solid fraction of the bulk for case '1' and case '2'*
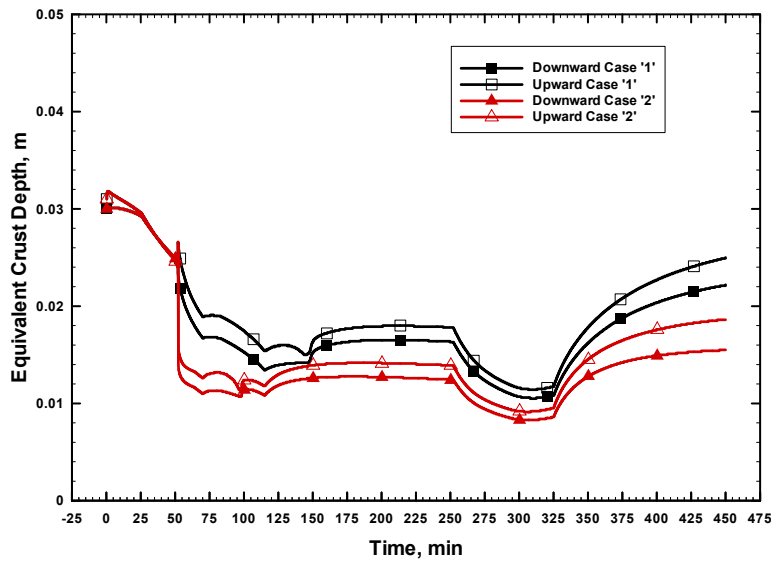

Fig. 4.2-6b: *M3b – Calculated equivalent crust depth at the melt upper surface (upward) and at the melt/concrete interface (downward) of case '1' and case '2'*

The initial equivalent crust depth amounts to ~3 cm at both, the upper melt surface and at the melt/concrete interface. In accordance with the decline of solid fraction, the crusts melt down from ~1.7 cm to 1.1 cm for case '1' and from 1.3 cm to 0.9 cm for case '2' following the power increase after 250 min into the test.

However, while the solid fraction is independent of the initial mass of corium and thus is independent of the melt composition, the equivalent crust depth for case '2' is generally lower

than for case '1'. This is consistent with the lower melt temperature which requires a lower crust depth to pass the same heat flux to the ablating concrete surface.
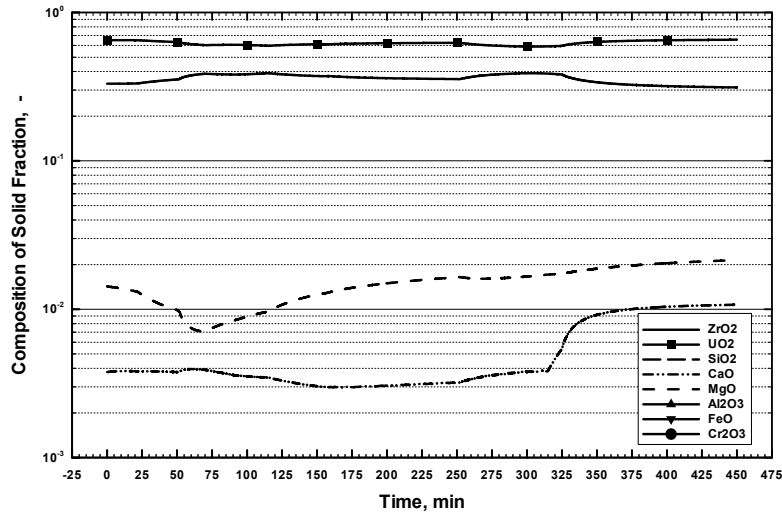

Fig. 4.2-7: *M3b - Predicted composition of the solid traction vs. time for case '1'*

Fig. 4.2-7 shows that the melt solid fraction almost entirely consists of the refractory components UO_2 and ZrO_2. Correspondingly, the low melting concrete decomposition products are predominantly found in the liquid phase.

Finally, the predicted evolution of melt front progression into the concrete is compared with the test results.
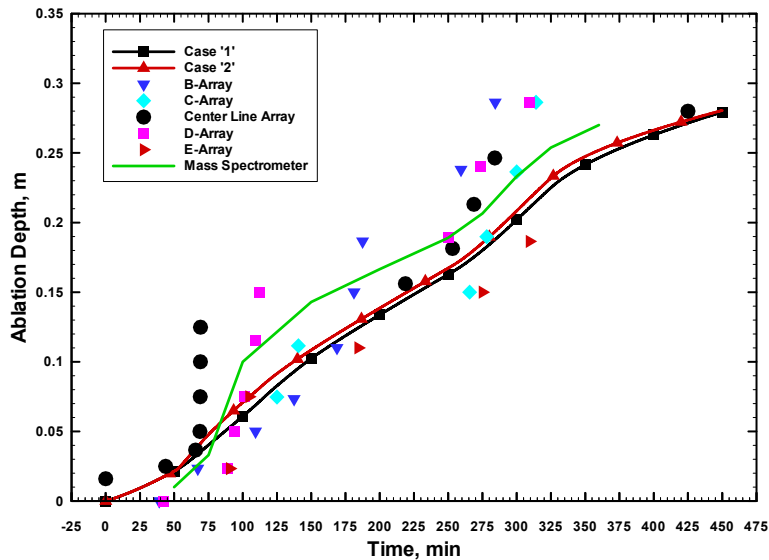

Fig. 4.2-8: *M3b - Calculated ablation depth for case '1' and '2' in comparison with the experimental results obtained from various thermocouple arrays cast into the concrete and from mass spectrometer analyses of the flow of released MCCI gases. The mass spectrometer data represents the average ablation front progression, while the thermocouple arrays reveal the local inhomogeneities. 0 min indicates the start of concrete ablation.*

In agreement with the experimental results, both calculations yield a final ablation depth of ~28 cm, see Fig. 4.2-8. Further, the overall evolution of the predicted ablation depth is in adequate agreement with the test data. This is attributed to the consistency between the predicted and experimentally observed upward/downward power distribution. The results also point to an independence of the heat flux distribution from the melt composition.

In conclusion, the validation against M3b indicates that melt temperature and ablation depth as obtained from COSACO are well in line with the experimental outcome. Further, the validation has identified that the volumetric solid fraction and the ablation front progression develop independent of the melt composition. Instead, the power variation in M3b suggests that the volumetric solid fraction correlates with the power deposited in the melt.

These specific characteristics will be further evaluated by validating COSACO against the MACE test M4.

4.2.2   MACE test M4

The composition of the ~480 kg heavy melt charge which represents fully oxidised corium of a PWR and which was initially present on the concrete basemat is listed in Tab. 4.2-2.

Component	wt%
UO_2	57.2
ZrO_2	28.7
SiO_2	6.7
CaO	1.3
MgO	0.06
Al_2O_3	0.39
Cr	5.65

Tab. 4.2-2: *Initial composition of the melt used in M4*

The concrete used to fabricate the $0.5x0.5m^2$ large basemat contained the following constituents:

Component	wt%
CaO	13.35
MgO	0.62
Al_2O_3	3.83
SiO_2	66.0
CO_2	10.6
H_2O	5.6

Tab. 4.2-3: *Composition of siliceous concrete as used in M4*

The input power was 280 kW initially and declined stepwise to ~100 kW during the first 75 min into the test, see Fig. 4.2-9.
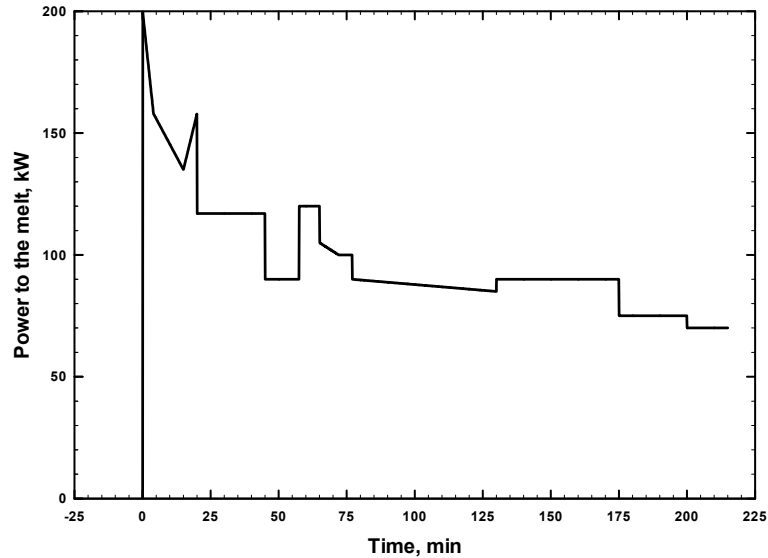
Fig. 4.2-9: *M4 – Power to the melt vs. time*

The heat losses into the sidewalls stayed in the range between 5-15 kW for the entire test. Due to flooding of the melt free surface at 23 min, 120 kg corium were determined to be quenched by the overlying water pool and, accordingly, removed from the MCCI zone. Equivalent to the M3b analysis, two calculations were conducted to examine the influence of melt mass on the predicted melt temperature for the M4 test.

Fig. 4.2-10a/b compare the calculated melt temperature with the experimental results for the full amount of corium initially present in the test (case '1') and for a melt mass being reduced by 120 kg at the time of flooding (case '2').
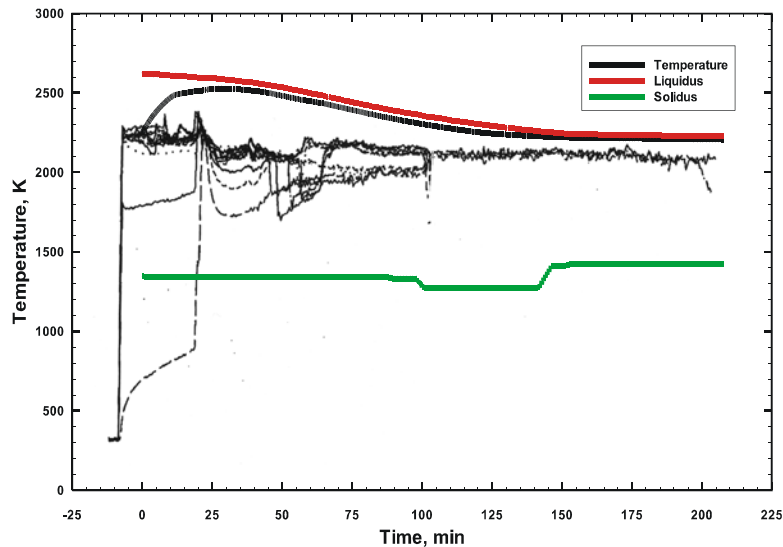

Fig. 4.2-10a: *M4 - Melt temperature prediction for case '1' in comparison with the experimental result*
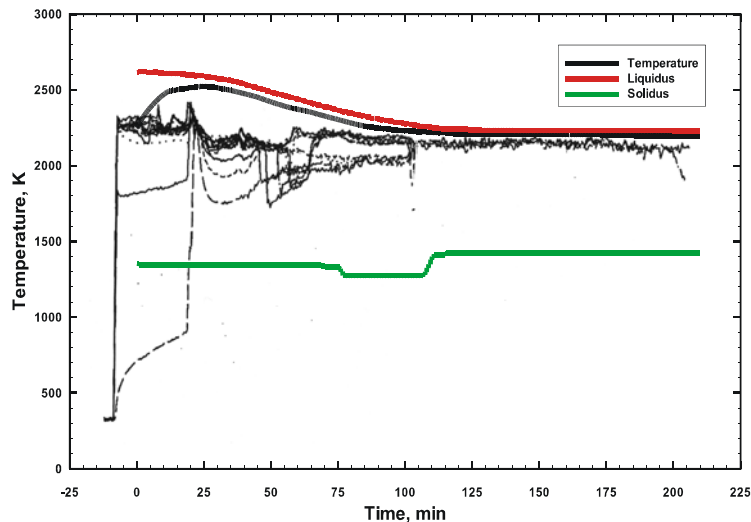
Fig. 4.2-10b: *M4 - Melt temperature prediction for case '2' in comparison with the experimental result*

Similar to the M3b analysis, the calculation employing the lower melt inventory during the phase following flooding yields a lower melt temperature. During this phase, the calculated temperature of case '1' slightly deviates from the experimental result by 50 K, while case '2' overpredicts the temperature by 100 K. The initial course of calculated temperature is not coincident with the experimental data for both cases. The calculated temperature rise is attributed to the high initial solid fraction and is similar to the results of the M3b analysis.

On the other hand, it is worth noting that the measurements of thermocouple arrays which recorded melt temperatures until 50 min into the test, are considered to be highly suspect by the experimenters, as during posttest examination no evidence of these arrays was found there where they were initially positioned. Thus the recorded temperatures from these thermocouples most likely do not represent the actual temperature response.

After attaining quasi-steady conditions, the predicted behaviour of melt temperature is in good agreement with the observed characteristics. In particular, the analyses show that the melt does not cool down, which is in correspondence with the experimental results.

Contrary to M3b, the predicted melt temperature levels off at quite similar values for both cases. Examination of Fig. 4.2-11 indicates that after the ablation depth exceeds a certain threshold, the liquidus temperature does not decline further but remains constant. This behaviour is consistent with the phase diagram of mixtures of core oxides and siliceous concrete, see Fig. 3.4-7 which exhibits a horizontal liquidus line over a wide range of concrete concentration.
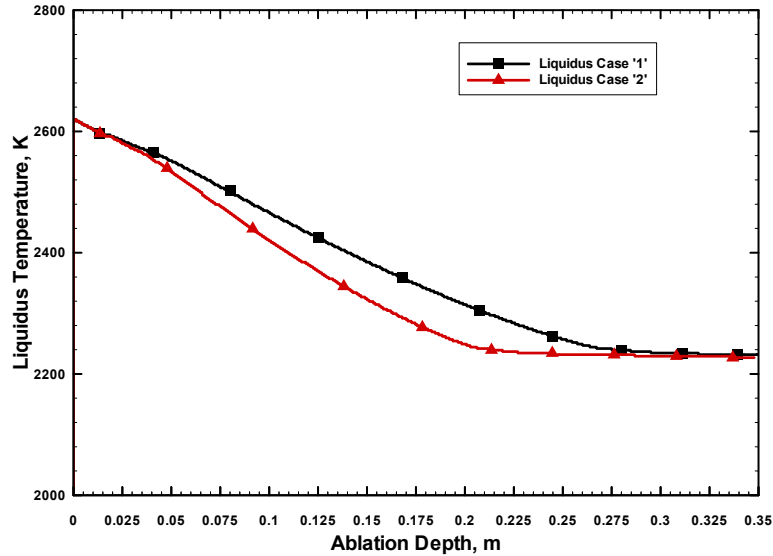
Fig. 4.2-11: *M4 - Liquidus temperature vs. ablation depth for case '1' and case '2'*

Since both cases exceed this threshold, it is evident that the end-state temperature level becomes almost independent of the initial mass. However, the case involving the reduced melt inventory achieves the end state temperature level earlier than case '1'.

In terms of solid fraction, Fig. 4.2-12a indicates that the predicted total volumetric solid fraction of M4 amounts to 70% initially, while the volumetric solid fraction in the bulk constitutes about 50% of that value. During the initial 50 min of the test, the total volumetric solid fraction falls to 10% independent of the case considered and remains constant at this value for the remainder of the experiment. In terms of the bulk, the solid fraction at steady state is about 3%.

Equivalent to M3b, COSACO predicts almost identical volumetric solid fractions for both cases. This observation supports the conclusion from the post test calculation of M3b, that the volumetric solid fraction is independent of the type of the melt. The equivalent crust depth amounts to 3 cm initially and declines to <1 cm, see Fig. 4.2-12b.

Relative to the M3b results, the predicted solid fraction and corresponding crust depth are consistently lower for M4, though the power supply in M3b was generally higher than in M4. This is in apparent contradiction to what was preliminarily concluded from analysing M3b, namely that the solid fraction is governed by the power supply. However, the conclusion was drawn on the basis of the same concrete area. Since, however, M3b and M4 involve different dimensions, the following rationale applies to closer characterise the effect of power supply.

Within the phase in which the power was constant at 215 kW, the solid fraction predicted for M3b fluctuates around ~25%. In comparison, for M4 the solid fraction is determined to be 10% for the period in which the power supply was between 90 and 100 kW. Though the absolute power supply of M3b is more than twice that of M4, the power density, i.e. the power transferred to the melt divided by the concrete surface, amounts to about 400 kW/m^2 for M4 and 155 kW/m^2 for M3b. The ratio between the power densities of M4 and M3b, 2.58,

is almost equal to the inverse of the corresponding ratio between the solid fractions, which is 0.4. Hence, the power density is considered to dominate the volumetric solid fraction.
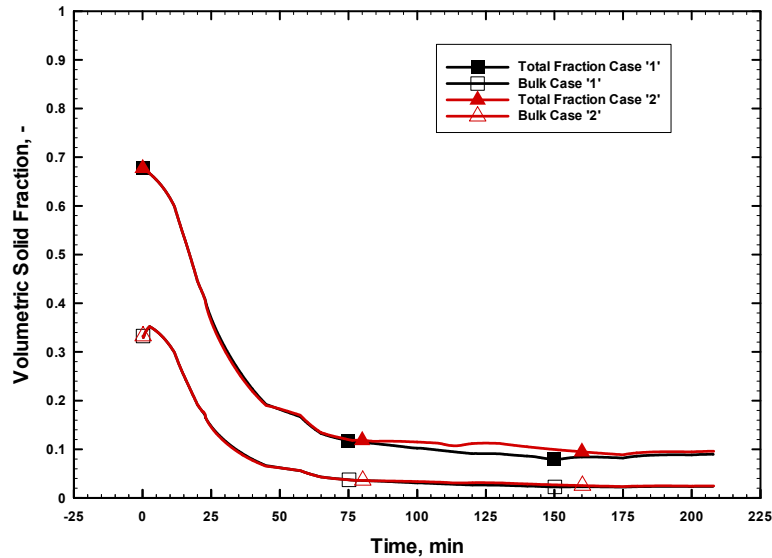

Fig. 4.2-12a: *M4 – Calculated volumetric solid fraction of case '1' and case '2'*
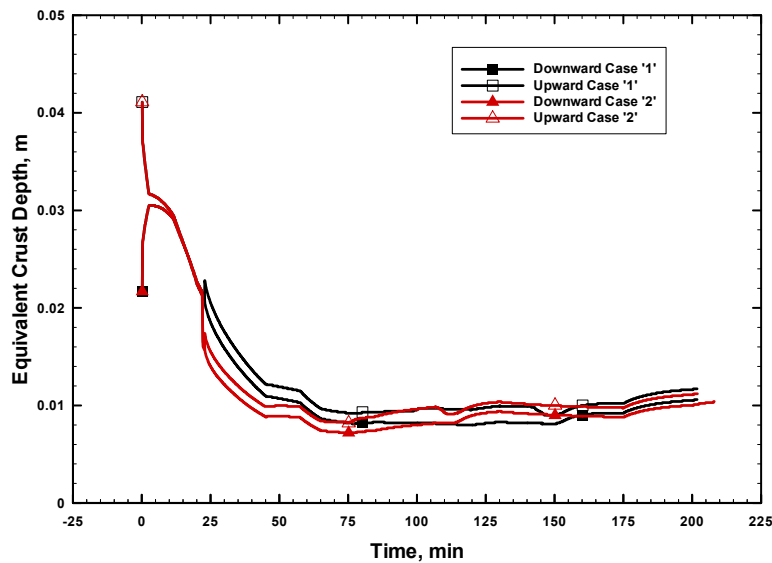

Fig. 4.2-12b: *Calculated equivalent crust depth at the melt upper surface (upward) and at the melt/concrete interface (downward) of case '1' and case '2'*

Fig. 4.2-13 compares the calculated ablation depth with the experimental data. The predicted evolution and the terminal depth are in adequate agreement with the test results for both cases, as is clear from this figure. This result supports the tentative conclusion from the M3b analyses, that the ablation depth is largely independent of the melt composition. Further, it indicates that the modelling of MCCI as pursued in COSACO yields the experimentally observed heat flux distribution.

In comparison with the M3b test, the ablation rate observed in M4 is significantly higher. This is attributed to the far higher power density applied in M4. In particular, the power densities of 155 kW/m^2 and 400 kW/m^2 resulted in calculated average ablation rates of $1.03 \cdot 10^{-5}$ m/s and $2.8 \cdot 10^{-5}$ m/s for M3b and M4, respectively.
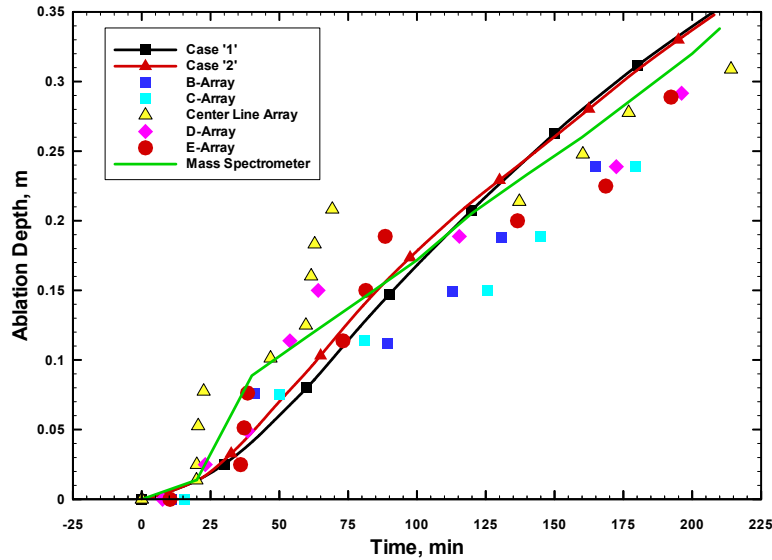

Fig. 4.2-13: *M4 - Calculated ablation depth for case '1' and '2' in comparison with the experimental results obtained from various thermocouple arrays cast into the concrete and from mass spectrometer analyses of the flow of released MCCI gases. The mass spectrometer data represents the average ablation front progression, while the thermocouple arrays reveal the local inhomogeneities. 0 min indicates the start of concrete ablation.*

4.2.3   Relevance of the validation against the MACE tests

The validation of COSACO against the MACE tests M3b and M4 reveals that the chosen modelling approach is adequate to represent molten core concrete interactions involving oxidic melts without applying adjustable parameters.

Firstly, the code adequately predicts concrete ablation for both experiments. This result implies that the modelling of heat flux distribution is suitable to predict the effect of different power densities. More precisely, the modelling of the mutual dependency of thermal hydraulic characteristics and thermo-chemical aspects yields heat flux distributions along the heat-removing boundaries of the pool which are consistent with the experimental findings.

Considering the EPR, one can conclude that COSACO is capable of providing adequate predictions of melt front progression into the concrete including the effect of a change of the surface/volume ratio of the melt as well as of the decay heat. The code thus allows to parametrically investigate the consequences of different amounts of melt involved in the initial melt pour, i.e. to identify the expected self-adjusting characteristic of the MCCI.

Due to the capability of the code to predict the heat flux distribution, benefit can be taken from the true physical characteristics of the lower parts of the RPV and the MCCI pool to

form coherent system connected by radiant heat transfer to verify the temporary melt retention. In combination with the parametric variation of the initial amount of melt, such coherence is expected to strongly contribute to make plausible that the temporary melt retention functions independently of scenario-specific melt release sequences from the reactor pressure vessel.

Secondly, the code prediction is in agreement with the experimental observations that oxidic melts only cool down slightly. This suggests that in combination with adequately predicting the ablation front progression, COSACO is capable of providing the thermochemical state of the melt and, in particular, the volumetric solid fraction, as a relevant initial condition for melt spreading. The solid fraction is of specific interest, since it significantly influences the melt viscosity according to Eq. 3.7-18. Therefore, a low volumetric solid fraction is essential for successful spreading.

In consequence, if it is demonstrated that the melt as it is released from the reactor pit principally exhibits a low volumetric solid fraction which translates into a low viscosity, melt spreading is not of concern.

In this respect, the analysis of M3b and M4 identified the following important property: the MCCI exhibits a tendency to yield similar solid fractions for a given power supply independent of the initial core oxide fraction, or, more generally, of the melt composition. The credibility of the melt retention concept benefits from such characteristics, in the sense that melt spreading does not depend on specific melt compositions which must be definitely attained. This further implies that a successful relocation of melt into the spreading compartment is also achieved if the composition of the concrete changes intentionally or accidentally.

Rather than being a function of composition, both, the analyses of M3b and M4 indicate that the volumetric solid fraction closely correlates with the power density. For the EPR, it is hence expected that the geometrical constraint of the reactor pit formed by the protective shielding restricts the formation of solid phases for a given decay power and a given amount of melt. Provided, that the goal of the temporary melt retention to collect the entire core melt inventory, can be fulfilled, the amount of melt and thus, the surface/volume ratio is only expected to vary in a narrow range. In consequence, the solid fraction at the time of spreading is predominantly a function of the decay heat.

However, before extrapolating these properties to the EPR, the validation of the code against tests with metallic melts has to be performed.

4.3 CORESA 2.1 and SURC4 experiments

2.2.1   CORESA 2.1 experiment

The purpose of the CORESA 2.1 experiment [Steinwarz 2002, Häfner 2001] was to investigate the ablation behaviour of LCS concrete during the interaction with highly superheated steel melts under transient conditions in a 2D geometry. The composition of LCS concrete is equal to that used in the M3b test, see Tab. 3.3-2.

The melt composition of the initial melt load of 740 kg is given in Tab. 4.3-1. The initial temperature of the melt amounted to 2000°C.

Component	wt%
Fe	77.5
Cr	10.5
Ni	7.1
Si	2.5
C	2.4

Tab. 4.3-1: *Composition of the melt used in the CORESA 2.1 test*

Since only the energy stored in the melt was available for concrete ablation, i.e. no power was supplied to the melt, the geometry was chosen with the aim to achieve a sufficiently high ultimate ablation depth. Therefore, the tests employed L-shaped profiles, as they offer a smaller concrete surface exposed to the melt than a cylindrical crucible entirely fabricated of concrete. These profiles were embedded in a cylindrical crucible fabricated of sintered MgO-bricks, see Fig. 4.3-1.
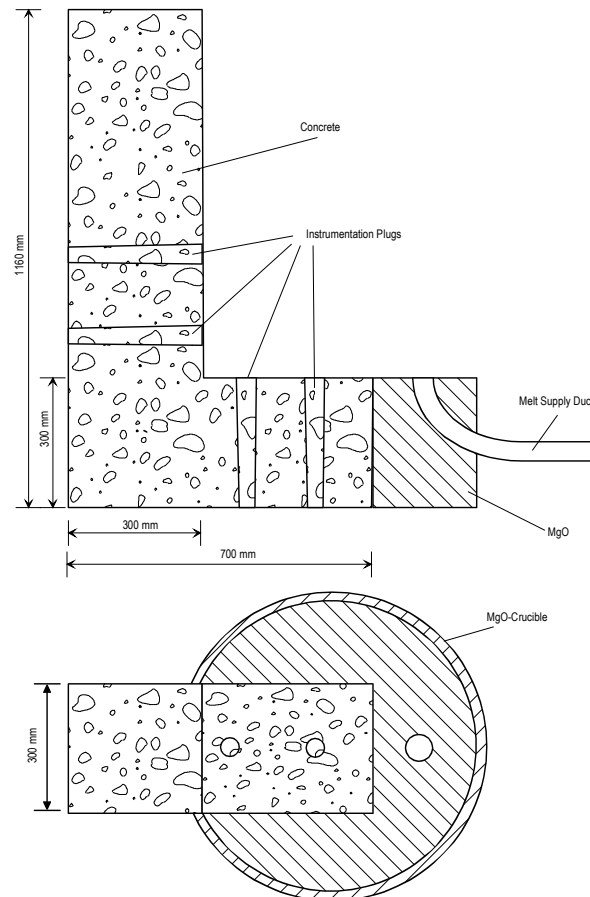

Fig. 4.3-1: *Concrete profile as used in the CORESA 2.1 experiment*

The L-profile is approximated employing the geometry model of COSACO, which is based on cylinder coordinates. The approximation is based on the equivalence between the heat-transferring surfaces, i.e. the melt/concrete interfaces and the melt free surface, of the experiment and of the calculation. Fig. 4.3-2 depicts the approximate geometry. The chosen

radius of 2.57 m only yields a low increase in the surface due to concrete ablation in radial direction. Specifically, assuming complete ablation in radial direction, the surface enlarges by 0.03 m² from 0.26 m². The total concrete volume arising from the geometry model amounts to 0.147 m³, while that of the L-profile equals 0.14 m³.
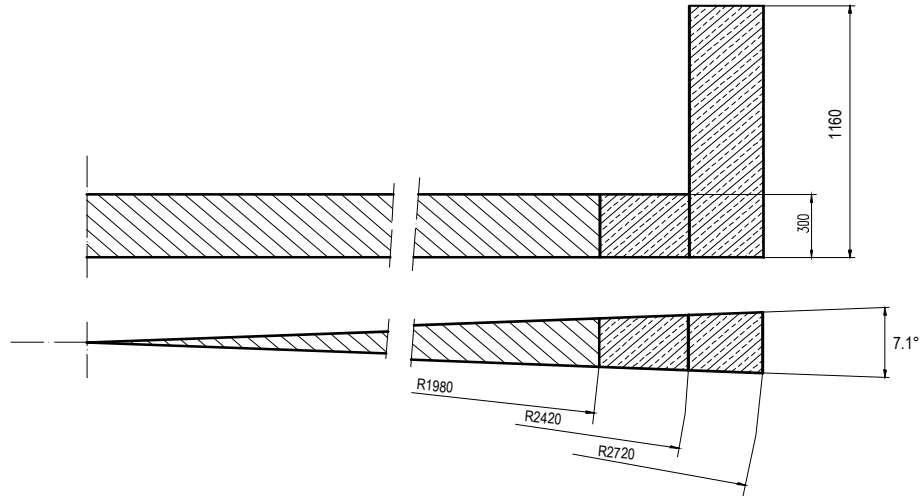

Fig. 4.3-2: *Approximate representation of the test geometry*

The melt also transports heat to the MgO-sidewalls in addition to the concrete. These losses were estimated using the 1D thermal conduction code WALTER [Fischer 2002]. The sidewalls were modelled using the material properties of MgO given in Tab. 4.3-2.

Property	Value
ρ	3030 kg/m³
k	3.7 W/mK
c	1000 J/kgK

Tab. 4.3-2: *Thermophyiscal properties of MgO-bricks [Wülfrath 1999]*

The heat transfer coefficient at the melt/sidewall interface was taken high, i.e. 10^4W/m²K, which results in limiting of the heat losses by the thermal conductivity of the sidewalls. The calculated losses are presented in Fig. 4.3-3 for the relevant time frame.
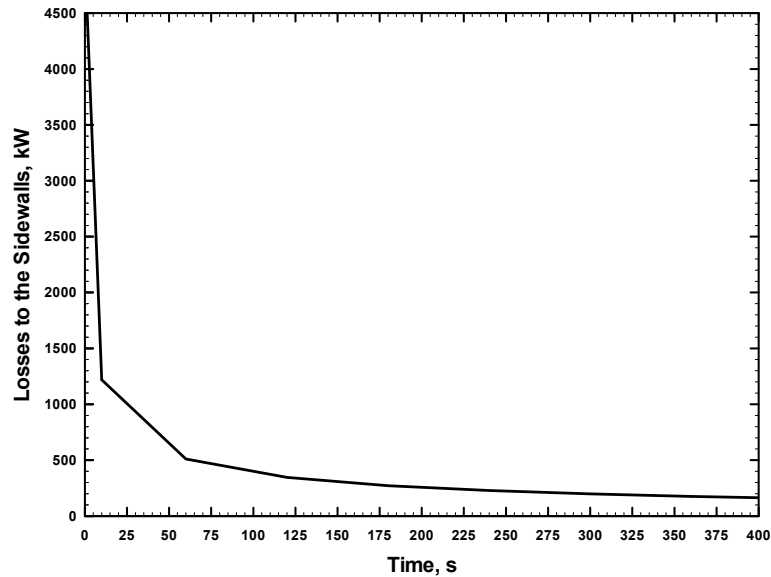
Fig. 4.3-3: *Estimated sidewall heat losses for the CORESA 2.1 test*

To simulate the formation of a light oxidic slag layer consisting of concrete decomposition products atop the metallic melt, the layered mode was used to represent the MCCI pool.

Fig. 4.3-4 presents a comparison between the predicted and measured ablation depth in downward and sideward direction. The experimental data were inferred from thermocouple arrays cast into the vertical and horizontal concrete walls of the L-profile. Since COSACO models an isotropic heat flux distribution resulting in same horizontal and vertical ablation rates, the horizontal ablation front progression also represents that in vertical direction.
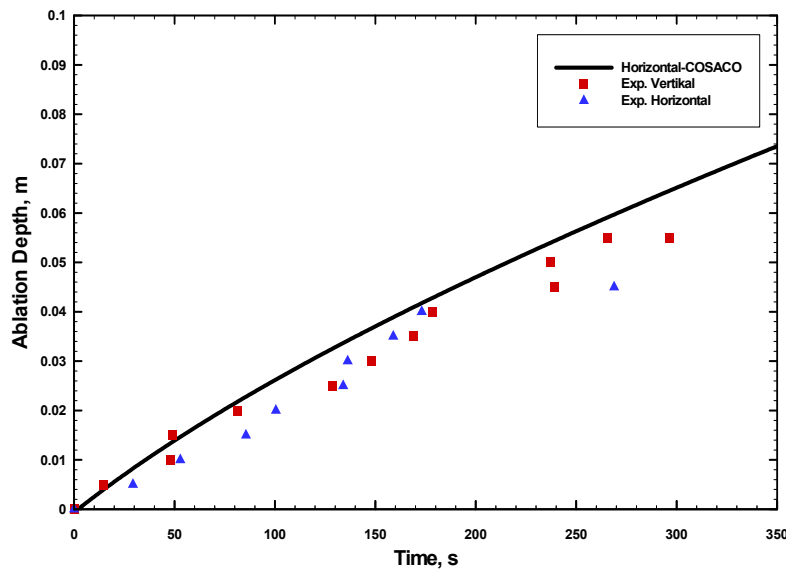

Fig. 4.3-4: *Comparison of calculated and measured evolution of ablation depth for the CORESA 2.1 test*

Fig. 4.3-4 indicates that the calculated ablation behaviour in both directions is well in-line with the experimental outcome. Notably, the prediction agrees with the experimental

observation that the ablation rate is almost constant despite the significant transient cool-down of about 400°C the melt underwent within the considered period of 350 s.

The ablation rate is overpredicted during the later stages of the experiment. This is attributed to incipient solidification processes in the melt which are not modelled in COSACO due to their insignificance with respect to the EPR.

The predicted evolution of temperature is in reasonable agreement with the test results, see Fig. 4.3-5. Further, the behaviour of both, calculated temperature and ablation front progression is consistent with the experimentally observed one.
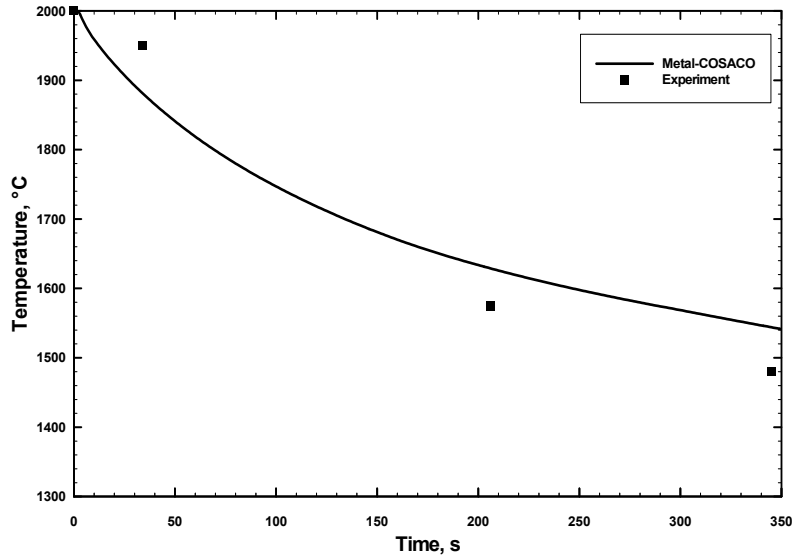

Fig. 4.3-5: *Comparison of calculated and measured evolution of temperature for the CORESA 2.1 test*

2.2.2   SURC4 experiment

The objective of the SURC4 experiment [Copus 1989] was to investigate the processes during the interaction between molten steel and basaltic concrete under dry conditions in a 1D geometry. Fig. 4.3-6 depicts the test section, while the composition of basaltic concrete is listed in Tab. 4.3-3.
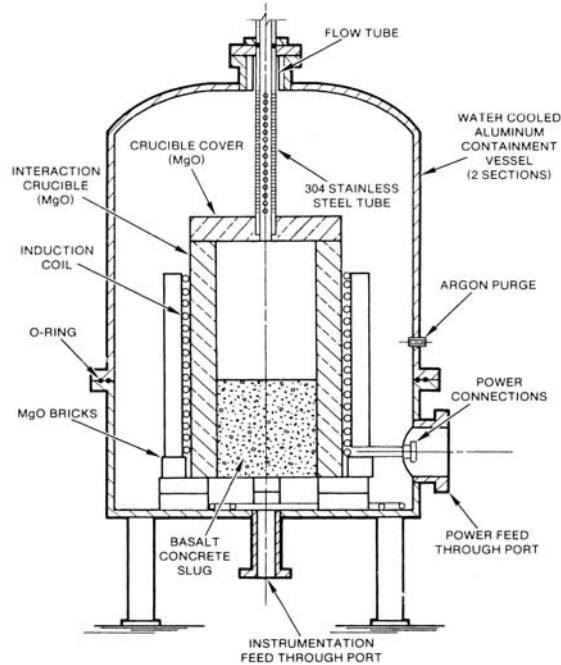
Fig. 4.3-5: *Test section of the SURC 4 experiment*

Component	wt%
CaO	9.6
Al_2O_3	9.1
Fe_2O_3	6.8
MgO	6.7
SiO_2	59.8
CO_2	1.6
H_2O	6.4

Tab. 4.3-3: *Composition of basaltic concrete as used in the SURC 4 test*

The melt was generated using 200 kg stainless steel which consisted of 72 wt% Fe, 19 wt% Cr, 8.5 wt% Ni and 0.5 wt% Si.

As part of this test, metallic Zr was added to the melt to investigate condensed phase chemistry. An amount of 20 kg of Zr was delivered instantaneously into the metallic melt through the crucible lid after a constant ablation rate was reached at 119 min. The melt pool temperatures were measured by thermocouples cast in the crucible basemat. The basemat had a diameter of 0.4 m. The power to the melt was 62 kW throughout the entire test except during a power shut down between 124 min and 132 min, see Fig. 4.3-7. The estimated heat losses into the sidewalls amounted to approximately 29 kW for the complete duration of the test.
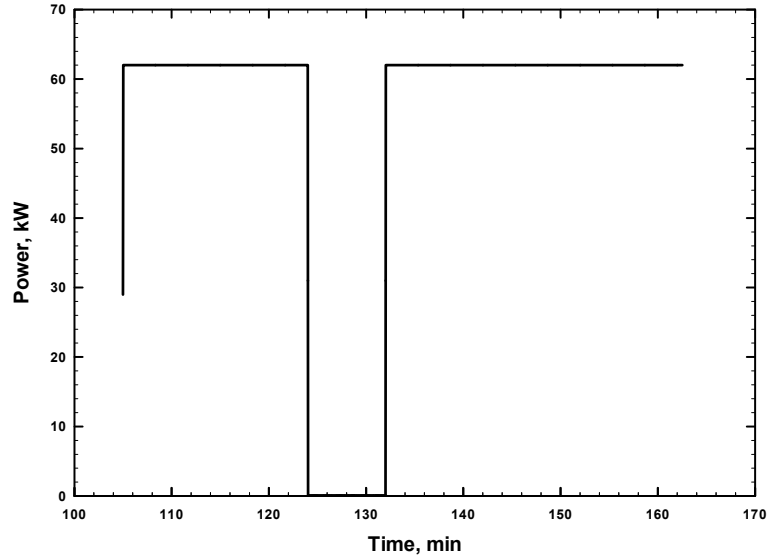
Fig. 4.3-7: *Power to the melt vs. time for the SURC 4 test*

Equivalent to the CORESA test, the layered option was used to simulate the formation of a light oxidic slag layer predominantly consisting of concrete decomposition products atop the metallic melt.

Figs. 4.3-8 and 4.3-9 show a comparison of the calculated and experimental results for melt temperature and erosion depth. Concerning melt temperature, the calculation results are in general good agreement with the experimental outcome.
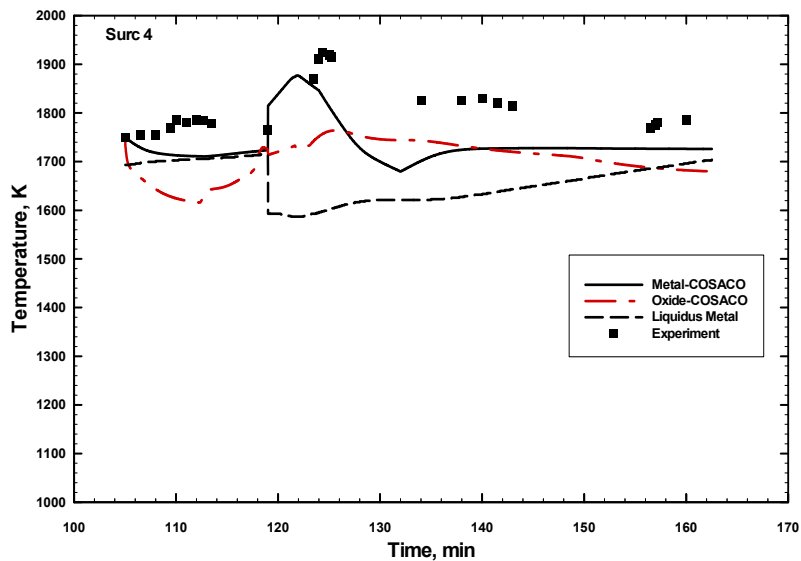

Fig. 4.3-8: *Comparison of calculated and measured evolution of temperature for the SURC 4 test*
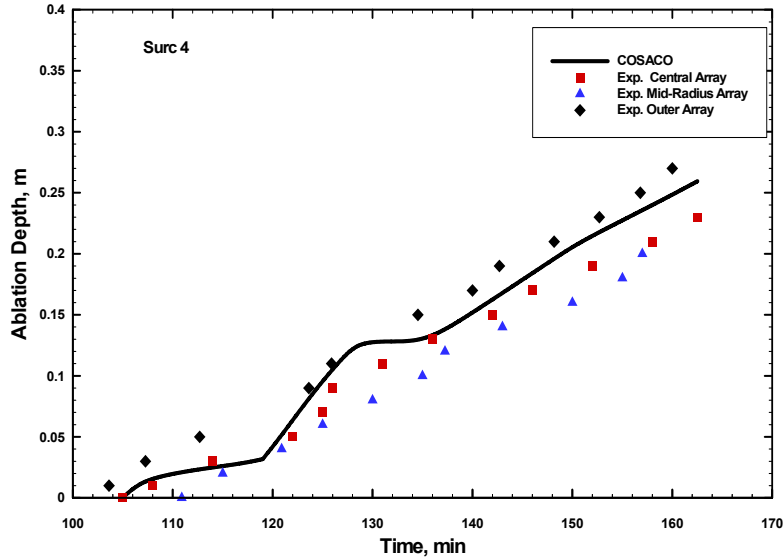
Fig. 4.3-9: *Comparison of calculated and measured ablation depth for the SURC 4 test*

The evolution of temperature during the initial and final phase as well as the temperature effect due to adding Zr could be predicted within a range of 50 K. Similarly, the calculated ablation characteristics are also in line with the experimental outcome, aside from a slight overprediction of ablation rate during the phase the power was lost.

In summary, the validation against the tests with metallic melts indicates that the modelling of heat transfer at the melt/concrete interface equally applies to transient conditions as in CORESA 2.1 as well as to rather quasi-steady conditions as prevailing in SURC 4. Therefore, COSACO is also suited to analyse interactions between concrete and metallic melts in the reactor pit of the EPR.

In addition, the validation results for both, tests with oxide and metal melts show that the applied quasi-steady state approach and with it the use of thermochemical equilibrium is adequate to model molten core concrete interactions.

Chapter 5

Analysis of the temporary melt retention in the reactor pit of the EPR

5.1 Objective and general approach

The specific task of this chapter is to assess the temporary melt retention in the reactor pit of the EPR. The objectives of the melt retention in the reactor pit are fulfilled, if the ability of the reactor pit

(i)   to accumulate most of the core melt inventory prior to the destruction of the gate that blocks the access to the melt discharge channel

(ii)   to achieve a unification of melt characteristics at the time of gate destruction independent of the melt discharge sequence and of the initial state of the melt

can be demonstrated.

An important issue for this assessment is to identify the masses of the oxidic and metallic melts which form while the core degrades, the corresponding initial conditions as well as the melt discharge sequence into the reactor pit. The melt release sequence is particularly important to assess whether the melt retention phase in the reactor pit enables to collect the corium, while the examination of the melt characteristics at the onset of melt spreading is influenced by all above contributors.

One approach to tackle the relevant aspects of melt release from the RPV would be to rely on predictions from integral codes such as MAAP 4 [MAAP 1994], SCDAP/RELAP5 [Allison 1993] or MELCOR [Gauntt 1998]. Aside from the amount of melt and the melt's initial temperature, they provide a melt release sequence from the reactor pressure vessel specifically depending on the scenario leading to the core melt accident. However, due to the lack of experiments investigating the late phases of in-vessel accident progression, the lower head failure models incorporated in these codes greatly depend on user-specified inputs with a wide range of possibilities. Consequently, code predictions regarding the accident progression in the lower head differ substantially [Ahn 1999].

Aside from these uncertainties, the influence of thermal radiation emitted from the MCCI pool on the lower head failure sequence cannot be assessed using these codes, given the inaccuracy of the integrated MCCI code packages to appropriately model the prevailing phenomenology of the MCCI. The latter aspect is important since the heat losses at the free

surface may constitute a significant fraction of the decay heat generated in the MCCI zone. It is evident that this heat contributes progressively to diminishing the lower head's mechanical integrity and eventually, to reducing the time frame to release the core melt inventory entirely into the reactor pit.

Instead of relying on specific melt release sequences obtained from the before-mentioned codes, it is hence advisable to build the verification of the accumulation function on a generalised melt release sequence. This sequence is based on an integral approach for the vessel failure mode and on the coupling of the RPV lower head and the MCCI pool by thermal radiation. Nevertheless, the in-vessel codes provide valuable information on the state and on the integral amount of the melt as well as on the in-vessel Zr-oxidation level. This aspect is relevant to make plausible that the MCCI establishes normalised, i.e. defined melt physical characteristics which are also favourable with regard to a successful spreading transient, independent of the melt characteristics at the time of discharge from the RPV.

Thus, the specific systematic for demonstrating the retention function of the reactor pit follows two distinct paths to examine individually the specific objectives:

(i)   Melt accumulation

        This part investigates melt accumulation using the generalized melt release sequence. The investigation combines a criterion for global vessel failure of the RPV and its internals with a parametric variation of the melt mass initially released into the reactor pit. The melt remaining in the vessel only discharges into the reactor pit after the global failure criterion is achieved. Hence, the generalized melt release sequence consists of two melt pours. Further, the onset of MCCI is varied to investigate the effect of a change of decay power on melt accumulation.

(ii)   Melt conditioning

        Calculations are conducted employing a specimen melt release sequence obtained from MAAP 4. In combination with varying the Zr-oxidation level, this set of calculations is particularly valuable to prove the independence of the melt characteristics from the in-vessel Zr oxidation level at the time of gate failure.

In conclusion, the verification strategy aims at demonstrating that the temporary melt retention exhibits inherent characteristics which makes its function independent of the existing broad spectrum of scenarios initiating the core melt accident, and correspondingly, of the resulting melt states and melt release modes.

Chap. 5.2 describes the modelling of melt accumulation and of melt conditioning as well as corresponding assumptions. Chap. 5.3 then highlights the obtained results, while Chap. 5.4 describes the conclusions on the temporary melt retention.

5.2 Modelling approach

5.2.1 Modelling of melt conditioning

This section specifically concerns the influence of in-vessel fuel cladding oxidation level on the melt characteristics at the time of gate failure. The oxidation level represents the portion of Zr oxidised in-vessel related to the total Zr-inventory in the core. For the purpose of this study, three calculations are conducted employing oxidation levels equal to 30%, 40% and 70%. The upper and lower limits of this variation constitute the maximum expected range of in-vessel oxidation levels as predicted with MAAP 4 [Azarian 1999], while 40% is assumed to be the reference level. This value is also employed for the cases investigating melt accumulation.

The underlying melt release sequence, see Fig. 5.2-1, as used for this analysis was obtained from a MAAP 4 analysis of an LBLOCA.
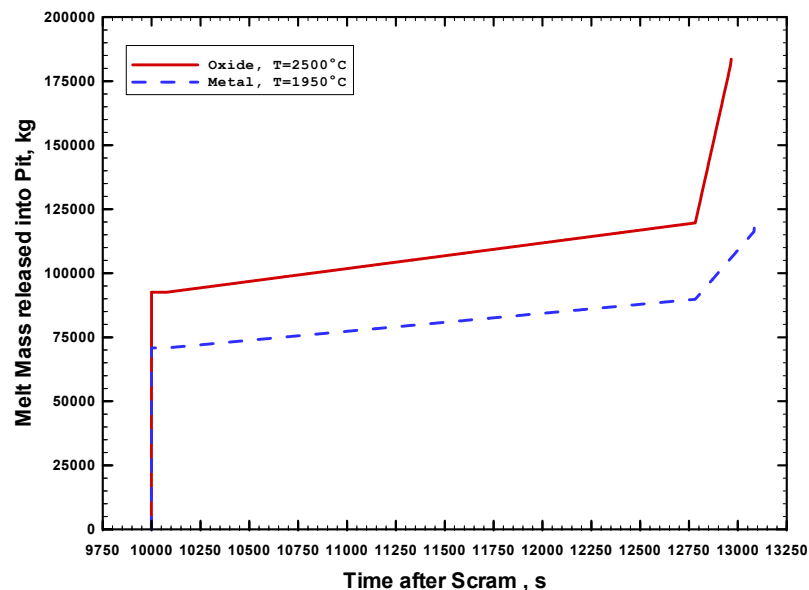
Fig. 5.2-1: *Two-step melt discharge from the RPV as obtained from a MAAP 4 analysis of LBLOCA [Azarian 1999]*

According to that sequence, about 120 t of metallic melt and 185 t of oxidic melt are released into the reactor pit within ~50 min.

Tab. 5.2-1 lists the composition of the oxidic and metallic core melt inventory. Due to the good solubility of Zr in $(U,Zr)O_2$ melts [Farmer 1999a], most of the Zr is present in the oxidic melt.

Case	Oxidation Level	Oxidic Melt [kg]			Metallic Melt [kg]			
		UO_2	ZrO_2	Zr	Fe	Cr	Ni	Zr
Standard-30-L	30%	141700	15700	24400	92000	13150	8700	2710
Standard-40-L	40%	141700	20920	20900	95200	13600	9000	2320
Standard-70-L	70%	141700	36600	10450	104500	14950	9900	1160
Standard-40-M	40%	141700	20920	20900	95200	13600	9000	2320

Tab. 5.2-1: *Total core melt inventory and corresponding cases to be investigated. The number in the nomenclature of cases denotes the in-vessel Zr-oxidation level, the final letter indicates representation of the molten pool by stratified layers (L) or by a mixed melt (M)*

The decay heat level in the oxide melt rises in proportion to the amount of UO_2 released into the pit while that in the metallic melt rises in proportion to the amount of released iron. This assumption also applies to all cases concerning melt accumulation.

Throughout this study, the molten pool is assumed to consist of stratified layers. The reasoning is that mixing due to molten pool agitation by MCCI gases is not considered effective because of the assumed formation of a crust at the oxide-metal interface due to the high temperature difference of initially 550 °C between the two phases and the high density difference of initially ~2000 kg/m^3. Thus, the downward MCCI is governed by the oxidic melt unless its density falls below that of the metal melt. This event initiates the modelling of a layer inversion which relocates the metallic melt underneath the oxidic one and at the same time mixes the slag layer with the oxide.

However, to also assess the effect of postulated mixing, one supplementing calculation is conducted using the mixed model of COSACO on the basis of the melt initial conditions of the reference case Standard-40-L.

5.2.2 Modelling of melt accumulation

Instead of a predetermined melt release, the modelling of melt accumulation makes use of a generalised melt release sequence which specifically takes into account that the MCCI pool and the lower structures of the RPV form a coherent system connected by radiant heat transfer. It starts from the situation as assumed in Fig. 5.2-2.
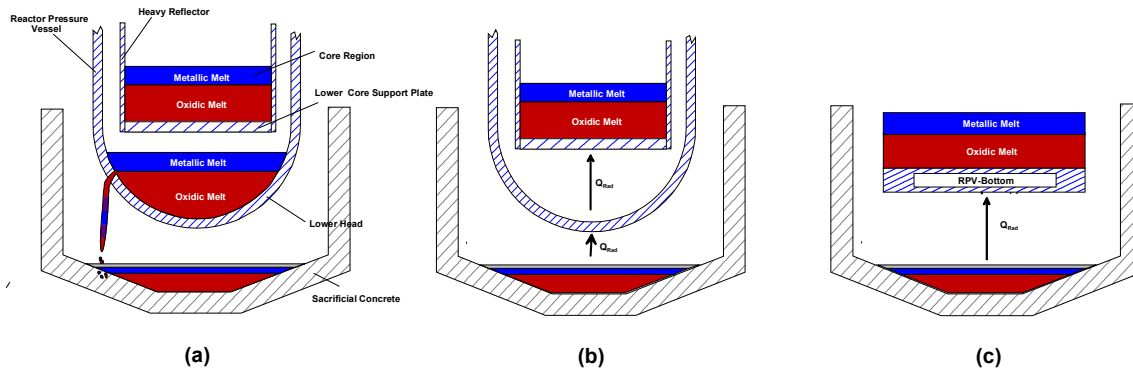
Fig. 5.2-2: *Modelling of melt release from the reactor pressure vessel*

Contrary to current operating PWRs, the core of the EPR is enclosed by a heavy reflector of substantial thickness. Thus, similar to core melt sequences studied for the AP 600 [Theofanous 1997], it is assumed that the melted core forms a pool on the lower support plate before melt-through of the heavy reflector takes place. After a first melt relocation, the rest of the pool discharges gradually into the lower head as the failure location widens by continued melting of the heavy reflector.

Ultimately, the molten core forms two melt pools, where one is located in the lower head, while the rest of the melt is trapped by the heavy reflector and the core support plate, see Fig. 5.2-2a. The lower head is subject to the highest heat flux density at an angle of $\sim 70°$-$75°$ along the azimuth of the lower head [Sehgal 1999]. Therefore, the failure location is also in that region. In terms of the first pour, it is thus assumed that the melt located above this location discharges into the reactor pit and initiates the MCCI.

The prediction of the amount of melt being in the lower head and correspondingly, of that initially released into the pit, entails significant uncertainties. The approach to envelope these uncertainties bases on a parametric variation of the amount of melt initially present in the pit. Specifically, the initial oxidic and metallic melt masses are varied between 40% and 80% of the mass obtained from the MAAP 4 calculation, see Fig. 5.2-1 and Tab. 5.2-1. The lower bound of 40% constitutes a reduction of 10 percentage points relative to that of the first release predicted by MAAP 4. At the same time, it is assumed that the melt located in-vessel rests entirely on the lower core support plate, see Fig. 5.2-2b.

Further, this variation yields different surface/volume ratios of the melt initially present in the pit, and is therefore expected to demonstrate the self-adjusting characteristics of the temporary melt retention.

Following the assumption that all in-vessel melt rests on the lower support plate, the lower head and the lower support plate are concentrated into a single equivalent mass, thereafter called RPV-bottom, see Fig. 5.2-2c. The RPV-bottom weighs ~ 51 Mg, to which both structures contribute in a similar proportion. This mass is assumed to be homogeneously heated by thermal radiation emitted from the MCCI pool and by a fraction of decay heat generated in-vessel according to the following equation,

$$\frac{d(m_{BT}e_{BT})}{dt} = \dot{Q}_{rad} + \dot{Q}_{SP} \qquad\qquad (5.2\text{-}1)$$

Both RPV structures are combined to a single RPV-bottom due to the strong coupling of these structures by thermal radiation.

The radiation term of Eq. 5.2-1 is evaluated using the corresponding model implemented in COSACO. Consistent with the analyses accompanying the FOREVER experiments [Sehgal 1999], the emissivity of the RPV-bottom is taken as 0.9. The slag and oxidic melt emissivities are both taken as 0.95 according to pyrometric temperature measurements performed in the COMAS large scale spreading tests with prototypic oxidic corium, e.g. [Steinwarz 1999a].

If a certain, temperature-dependent criterion is achieved, the RPV-bottom is assumed to fail. Upon failure, the remaining fraction of the oxidic and metallic melt is discharged into the reactor pit. Also, the RPV-bottom adds to the MCCI pool with failure temperature and corresponding specific enthalpy as determined from the ternary Fe-Cr-Ni composition of the metal melt, see Tab. 5.2-1.

The generalised melt release sequence thus consists of two distinct melt pours: the first one initiates the MCCI, while the second one terminates the melt release from the RPV and accordingly, melt accumulation. In reality, however, also multiple melt releases or even continuous melt discharge modes are conceivable, which result in a successive increase in melt mass in the reactor pit. This situation is addressed by varying the initial mass of the initial pour between 40% and 80% of the total mass in combination with the second pour which establishes an upper limit for all potentially preceding melt releases. Therefore, the parametric variation of initial mass in combination with the ultimate failure criterion forms an envelope of the possible melt release modes.

Following the principal idea behind modelling of melt accumulation, the next chapters provide the information relevant to evaluate this model. Chap. 5.2.2.1 describes the contributions of heating by the melt located in-vessel, Chap. 5.2.2.2 gives an estimate on the initial temperature of the RPV-bottom and the integral failure criterion is developed in Chap. 5.2.2.3. Chap. 5.2.2.4 summarises the matrix of investigations.

5.2.2.1   Heating by the melt located in-vessel

Following the assumption that the melt located in-vessel rests on the lower support plate, the heating of the plate can be determined using the heat flux distribution for heat-generating pools in rectangular geometry. The following heat transfer correlations [Steinberner 1978] are widely used to quantify the heat fluxes at the molten pool boundaries, i.e. at the pool free surface, the heavy reflector and the lower support plate.

$$Nu_{up} = 0.345 Ra'^{0.233} \qquad\qquad (5.2\text{-}2)$$

$$Nu_{dn} = 1.389 Ra'^{0.049} \qquad\qquad (5.2\text{-}3)$$

$$Nu_{rd} = 0.85 Ra'^{0.19} \qquad\qquad (5.2\text{-}4)$$

where the Nu numbers and the internal Raleigh- number are of the form,

$$Nu = \frac{hl}{k_M} \qquad\qquad (5.2\text{-}5)$$

$$Ra' = \frac{\rho_M c_M g \beta_M \dot{q}''' l^5}{k_M{}^2 \mu_M} \tag{5.2-6}$$

The characteristic length is the molten pool height.

Assuming steady-state conditions, the overall energy balance for the molten pool yields,

$$\dot{Q}_{DH,Ox} = h_{dn} \Delta T_{SP} A_{SP} + h_{rd} \Delta T_{HR} A_{HR} + h_{up} \Delta T_S A_S \tag{5.2-7}$$

and thus, the decay heat transferred to the lower core support plate and correspondingly, to the RPV-bottom is,

$$\dot{Q}_{SP} = \frac{h_{dn} A_{SP}}{h_{dn} A_{SP} + h_{rd} A_{HR} + h_{up} A_S} \dot{Q}_{DH,Ox} \tag{5.2-8}$$

The particular form of Eq. 5.2-8 implies crust formation at the molten pool boundaries which establishes equal boundary conditions and thus identical driving temperature differences.

Property	Value
ρ	8600 kg/m^3
η	0.006 Pa•s
β	4.64x10^{-5}K^{-1}
k	2.6 W/mK
c	510 J/kgK

Tab. 5.2-2: *Properties of a molten oxidic pool for an oxidation level of 40%*

For the melt properties given in Tab. 5.2-2 and for a pool diameter of 4.05 m, the decay heat transferred to the lower support plate is depicted in Fig. 5.2-3 as a function of the total decay heat in the oxidic melt (i.e. in-vessel and ex-vessel) and of the particular melt fraction located in-vessel.

According to that figure, the fraction transferred to the lower support plate varies between ~1-1.6% of the total decay heat released in the oxidic melt. It is worth noting that the above estimate is conservative in terms of heating of the RPV-bottom, since it assumes that all melt located in-vessel rests on top of the lower support plate. In contrast, in the likely case of melt partition between the support plate and lower head, the decay heat generated by the melt located in the lower head would contribute entirely to the heating of the RPV-bottom. Already 10 Mg of oxidic melt located in the lower head having a composition corresponding to an oxidation level of 40%, contributes ~5.5% of the total decay heat to heating the RPV-bottom.

Therefore, in the likely case of two melt pools, above model considerably underestimates the direct heating of the RPV-bottom by in-vessel melt. Hence, the results obtained from the investigation of melt accumulation can be considered as conservative.
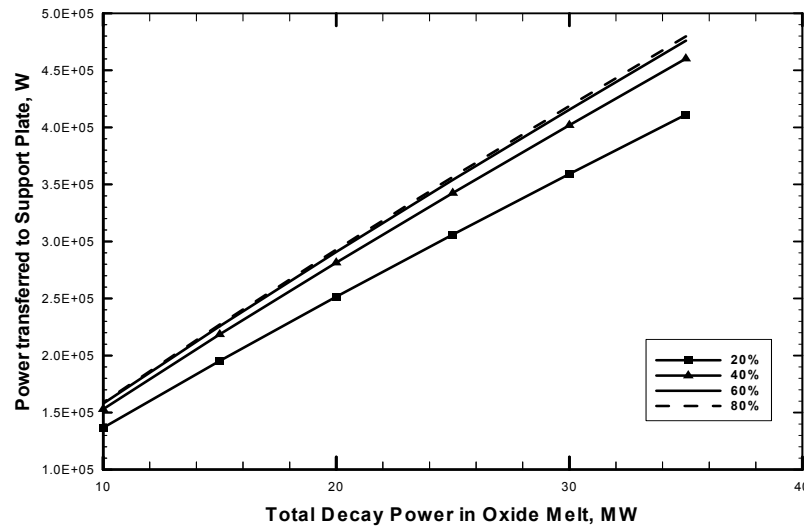
Fig. 5.2-3: *Heating of the lower support plate by in-vessel core melt as a function of total decay power in the oxide for various fractions of oxidic melt located in-vessel. The time-dependent behaviour of the decay heat in the oxidic melt can be obtained from Fig 5.2-5.*

5.2.2.2   Initial temperature of the RPV-bottom

A further assumption concerns the initial temperature of the RPV-bottom at the start of MCCI. This temperature determines the amount of energy to be absorbed by the RPV-bottom until achieving failure temperature.

The following estimate to determine the initial temperature uses MAAP 4 calculations performed to investigate the potential of in-vessel melt retention for the EPR by flooding the reactor pit with water [Cognet 1998]. The assumed scenario initiating the severe accident is an LBLOCA which is identical with that used to predict the sequential melt release given in Fig. 5.2-1. Therefore, the in-vessel processes, e.g. the sequence of core-melt relocation from the core zone into the lower head are identical for both analyses, as the assumption of RPV outside cooling by water only affects the failure of the lower head.

Consequently, Cognet's analysis can be used to estimate the initial temperature of the RPV-bottom. Qualitatively, the estimate starts from the mass of melt which relocates from the core zone into the lower head until its failure. This mass correlates with a certain amount of decay heat which heats the RPV-bottom. Correspondingly, a temperature rise results, from which the initial temperature is finally deduced.

The first task for quantifying the initial temperature is to assume the time of failure of the lower head. Assuming the failure time is required as the investigation of outside cooling yielded the highly debatable result that the lower head remains intact. A plausible assumption for the failure time is the onset of melt release given in Fig. 5.2-1, i.e. 9960 s, since the scenario used in both analyses is the same.

In contrast, the start of relocation from the core zone into the lower head can be directly inferred from Cognet's analysis which yielded 5960 s after scram. Between the start of melt

relocation and failure of the lower head, the average mass of oxidic corium present in the lower head was predicted to be 105 Mg, including 91.5 Mg UO_2.

Given mass and time interval, the decay heat produced in the lower head until vessel failure is predicted by weighting the total decay heat generated by the oxidic melt with the ratio between UO_2 located in the lower head and the total UO_2 mass of 142 Mg. Thus, about 65% of the decay heat is generated in the particular oxidic melt which is located in the lower head.

Aside from heating the lower support plate plus lower head, the phase between first melt relocation and vessel failure involves evaporation of ~20 Mg of residual water. Consequently, the amount of energy consumed to evaporate the residual water has to be subtracted from the decay heat generated in this time span.

The resulting energy balance for the sequence from initial melt relocation into the lower head until RPV failure is of the form,

$$m_{BT}\left(e_{BT,9960s} - e_{BT,5960s}\right) + m_W \Delta e_W = 0.64 \int_{t=5960s}^{t=9960s} \dot{Q}_{DH,Ox} d\tau \qquad (5.2\text{-}9)$$

where $\dot{Q}_{DH,Ox}$ is inferred from the curve in Fig. 5.2-5 representing the decay heat in the oxidic melt and Δe_W is the latent heat of water.

The energy balance yields a rise in specific enthalpy of the RPV-bottom by 603 kJ/kg. This translates into a heat-up by 750 K, using 780 J/kgK as the mean specific heat of the steel in the temperature interval between 300 K and 1500 K. Assuming a low initial temperature of 120°C, the temperature of the RPV-bottom at the onset of MCCI amounts to ~880°C.

To account for uncertainties in the above estimate, 800°C will be used as initial temperature throughout the analysis.

5.2.2.3   Criterion for vessel failure

The temperature at which failure takes place is determined by the ultimate strength at which the RPV steel looses its integrity for the given mechanical load. Since the primary system of the EPR is assumed to be depressurised in case of a core melt accident, only the weight of the core melt and of the combined RPV/lower head mass contribute to the stress that ultimately results in creep-induced failure.

However, the related load-bearing cross-section to determine the weight-induced stresses cannot be quantified due to the inherent uncertainties associated with predicting the lower head failure mode.

Consequently, instead of using a stress-based criterion, it is more appropriate to assume that global failure occurs when the temperature-dependent ultimate strength of the steel practically vanishes. High temperature tensile data are given in [Chavez 1994] for US American SA106 B carbon steel and in [Thinnes 1994] for US American SA533B1 steel for temperatures up to 1100 K and 1473 K, respectively. The first type is similar to that specified for the AP600, while the second was used to fabricate the vessel of Three Mile Island unit II. Fig. 5.2-4 plots the data in comparison with German vessel steel 20 MnMoNi 55.
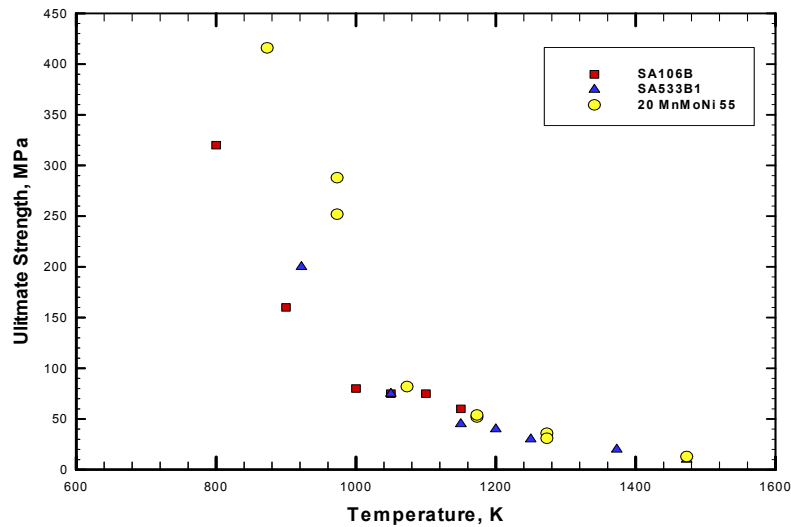
Fig. 5.2-4: *Ultimate strength of SA 106 B, SA 533B1 and of German steel 20 MnMoNi 55 7*
          [Senski 2002]

Extrapolating the data to zero ultimate strength yields a temperature of 1573 K corresponding to ~1300°C. This temperature is equivalent with the assumption for the loss of ultimate strength given in [Theofanous 1995]. The lower head would probably fail at temperatures below 1300°C due to the significant creep which evolves at such temperature level and which results in a steady reduction of the load-bearing cross-section.

5.2.2.4   Melt initial conditions and investigated cases

In terms of the Zr-oxidation level, the reference level of 40% is used. The compositions of the metallic and oxidic melts correspond to that oxidation level and are given in Tab. 5.2-1. The initial temperature of the oxidic melt is taken as the liquidus temperature, which amounts to~2500°C. The metal melt temperature is assumed to be 1550°C which constitutes a superheat of ~100 °C relative to the liquidus temperature of RPV steel. A similar temperature of the metallic melt was predicted by an analysis conducted by [Artnik 1996], who investigated the potential for in-vessel melt retention by RPV outside cooling for a 1300 MWe class PWR.

The oxidic and metallic melt masses initially released into the reactor pit are concurrently varied between 40-80% of the total melt masses. The total oxidic core melt mass amounts to 180 Mg which equals the value given in Tab. 5.2-1. In contrast, the total metallic core melt mass of 69 Mg used for this analysis is a-priori inconsistent with the information in Tab.5.2-1. However, as the RPV-bottom is assumed to fall into the reactor pit upon failure, the total metallic mass actually discharged into the pit is the sum of the metallic core melt and the RPV-bottom, i.e. 120 Mg. This mass is again in consistence with that given in Tab. 5.2-1-1 and used to investigate melt conditioning.

Due to the consistence in both, melt mass and composition, the present cases are also used to further evaluate melt conditioning.

Aside from the initial melt mass, the time of first melt release is varied to investigate the influence of decay heat generated in the MCCI pool on the failure time of the RPV-bottom and the retention time in the pit. This variation is equivalent to take into account different initiating scenarios, e.g. LBLOCAs and SBLOCAs.

In particular, the times of first melt release after scram selected for this study are 10000 s and 86000 s. The early starting point is consistent with an LBLOCA, whereas the late one corresponds to an SBLOCA. In terms of decay heat, the later onset corresponds to a reduction of ~30% compared to the earlier onset, due to the rapid decline of decay heat during the first hours after scram, see Fig. 5.2-5.

Equivalent to the analysis investigating melt conditioning, these calculations are also conducted assuming a layered configuration as the governing assumption for modelling the MCCI pool configuration.

In addition, to investigate the sensitivity of this assumption, two calculations are performed assuming that the MCCI gases intimately mix the oxidic and metallic melt. To this end, the initial and boundary conditions of the layered cases showing the lowest safety margin for both, early and late melt release, are used. Hence, the analyses in the layered mode had to be completed first to identify these particular cases.

Tab. 5.2-3 shows the matrix of calculations.

Case Nr.	Initial melt mass [% relative to total core melt mass from MAAP]	Time of first melt release [s after scram]	Layered Mode (L) Mixed Mode (M)
40%E-L	40	10000	L
40%L-L	40	86000	L
60%E-L	60	10000	L
60%L-L	60	86000	L
80%E-L	80	10000	L
80%L-L	80	86000	L
80%E-M	80	10000	M
80%L-M	80	86000	M

Tab. 5.2-3: *Matrix of calculations. The initial number indicates the initial mass, the first letter the time of first melt release (Early/Late), the second letter Layered or Mixed mode calculations.*

As is evident from Tab. 5.2-3, the mixed mode cases use the melt's initial conditions of the cases 80%E-L and 80%L-L which have been identified as the most critical ones with respect to safety margin, see Fig. 5.3-10.

Apart from the specific modelling and from corresponding assumptions and boundary conditions related to investigating melt conditioning and accumulation, general boundary conditions which apply to either topic need to be defined, i.e. decay heat and geometry. This is the task of Chap. 5.2.3.

5.2.3   General boundary conditions

5.2.3.1   Decay heat

The course of decay heat in the oxide and metal melt for a core thermal power of 4250 MW_{th} is presented in Fig. 5.2-5 for the relevant time frame. The data is consistent with the assumption of a release of 30% of volatile fission products into the containment atmosphere and with a ratio of about 85:15 for the initial distribution between oxide and metal melt.
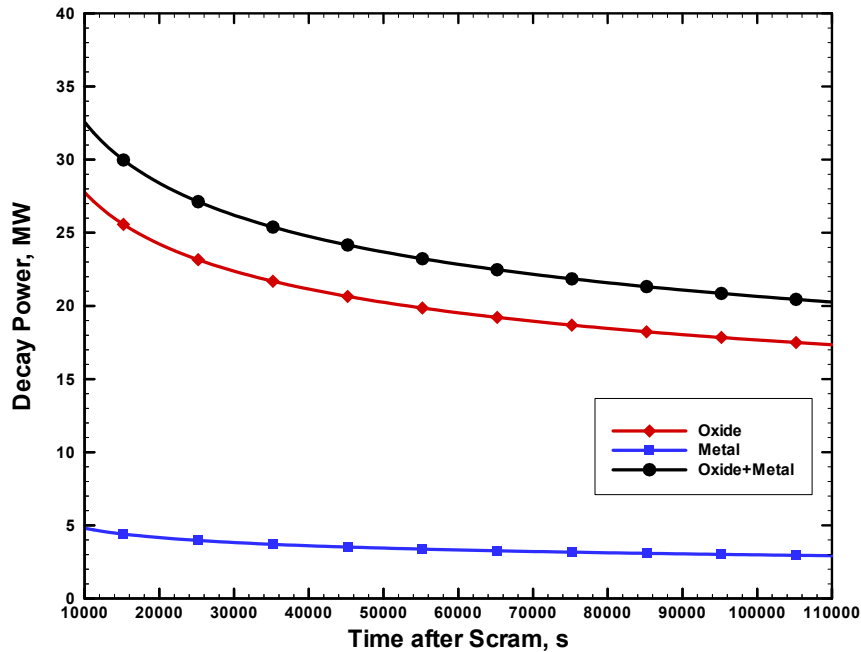

Fig. 5.2-5: *Decay heat in the oxide and metal melt. 0 s represents the scram of the reactor*

5.2.3.2   Geometry

The geometry of the reactor pit as used for the analysis is depicted in Fig. 5.2-6 in combination with the geometry model of the RPV-bottom to determine the radiant heat transfer. Further, it reveals the contours of the RPV and of the lower core support plate as well as the initial melt free surface locations as a function of melt mass. The location of the RPV-bottom corresponds to the centre of gravity of the lower head and lower core support plate.

Apparently, the lower head may be immersed in the melt, the extent of which depends on the amount and gas content in the melt as well as the strains that develop in the RPV steel. Such direct contact increases the heat transfer in comparison to thermal radiation. Nevertheless, radiant heat transfer is assumed to be the prevailing heat transfer mechanism throughout the entire MCCI sequence.
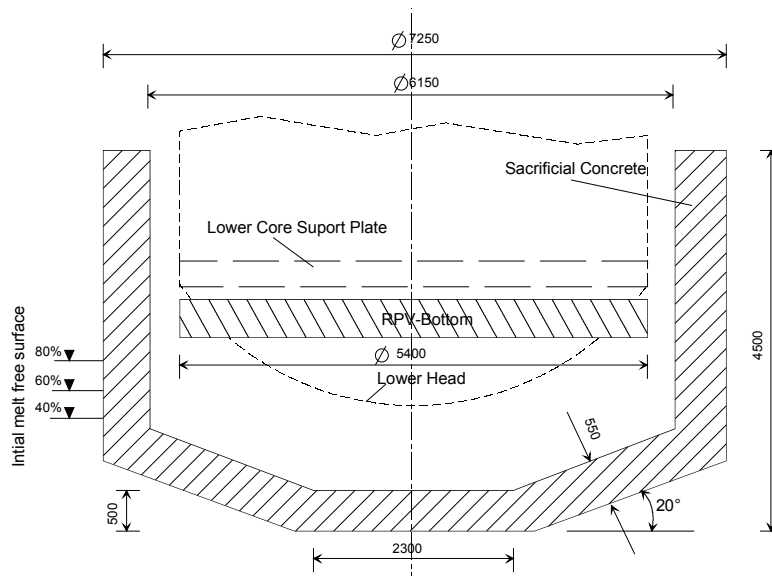
Fig. 5.2-6: *Geometry of the reactor pit*

5.3 Results

5.3.1 Discussion of the reference case Standard-40-L

Before comparing the results of the individual cases, the reference case Standard-40-L is described separately to provide an insight in the general characteristics of the MCCI phase, highlighting the relevant events and their consequences for the molten pool behaviour. This description is instructive for interpreting the results of the rest of the cases which are presented as composite plots in the perspective of the melt retention goals.

The characteristic events of this case are (i) the complete oxidation of the initial inventory of U/Zr metal at 11000 s into the accident, (ii) the effects related to the second melt discharge according to the release sequence depicted in Fig. 5.2-1, (iii) the layer inversion at 15900 s and (iv) complete ablation of the 50 cm thick layer of sacrificial concrete mounted on top of the melt gate at 16100 s.

Fig. 5.3-1 shows the evolution of temperature for the oxide, metal and slag layer during the MCCI phase. It shows that the temperature of the oxidic melt closely follows the liquidus temperature. Similar results arose from post test calculations of the M3b and M4 experiments which were described in Chap. 4.2. The metallic melt temperature is predicted to be about 500°C lower than that of the oxidic melt for the entire length of the MCCI in the reactor pit. Following the second melt discharge at 12780 s involving the addition of sub-stochiometric oxidic melt, the temperature of the oxide rises. This rise is attributed to exothermic chemical reactions of Zr and U contained in the sub-stochiometric oxidic melt with the concrete decomposition products that have accumulated in the period between the two melt releases. In addition, mixing of 2500°C hot oxidic in-vessel melt with the oxidic melt in the reactor pit having a temperature of 2400°C contributes to the temperature rise occurring at this instant.
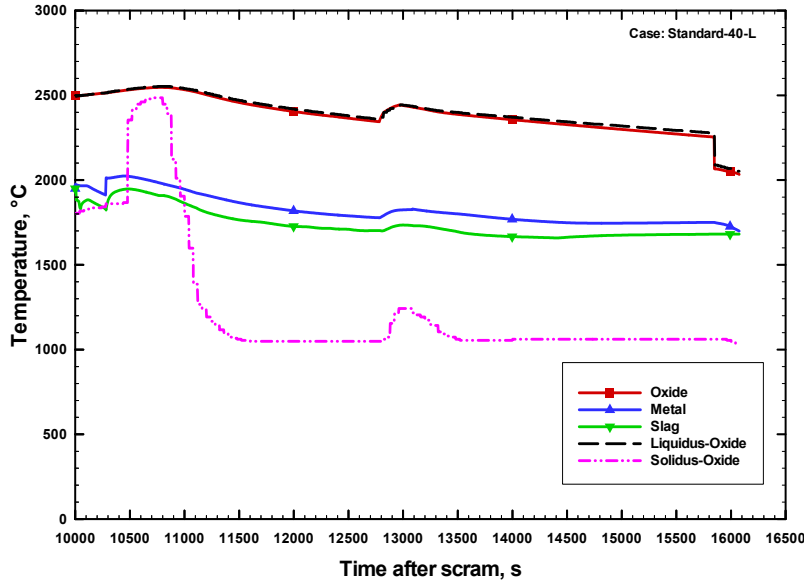
Fig. 5.3-1: *Temperature prediction for the oxide, metal and slag melt*

The increase in liquidus temperature is attributed to the increase in concentration of core oxides as a consequence of chemical reactions which at the same time reduce the concentration of the liquidus-decreasing concrete oxides. Apart from the overall history of oxide composition during the MCCI, Fig. 5.3-2 also shows this effect.
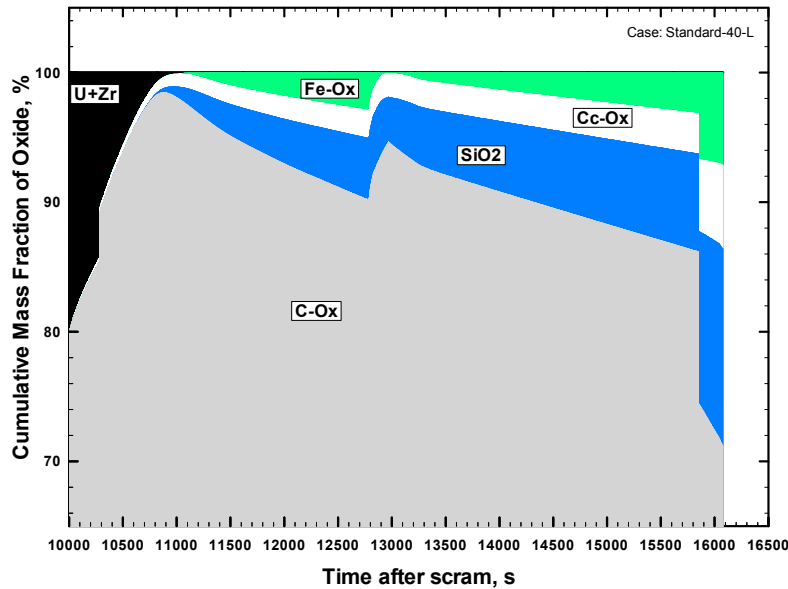

Fig. 5.3-2: *Composition of the oxidic melt for an initial Zr-oxidation level of 40%. C-Ox denotes UO_2+ZrO_2, Cc-Ox $Al_2O_3+CaO+MgO+Cr_2O_3$ and Fe-Ox Fe_2O_3+FeO*

Also visible from Fig. 5.3-2 is the complete oxidation of the initial U/Zr-metal inventory fairly early into the MCCI sequence. Remarkably, even the second melt release at 12780 s does not result in a new accumulation of U/Zr-metal in the melt.

Shortly before the end of the MCCI at 15850 s, a layer inversion is predicted, which arises as the density of the oxidic melt falls below that of the metallic melt, see Fig. 5.3-4 and which mixes the relative to the oxide cooler slag layer with the oxidic melt. The consequences are a steep decline in the oxide temperature by 200 K, see Fig. 5.3-1 and a strong increase in concentrations of iron-oxides, silica and concrete oxides at the expense of the core oxide concentration, see Fig. 5.3-2. Accordingly, the liquidus temperature also decreases substantially. Ultimately, at the termination of the temporary melt retention at 16100 s, the core oxide concentration in the oxidic melt only amounts to ~72%. Conversely, the accumulation of 28% of non-core oxides is sufficient to decrease the liquidus temperature by ~500°C relative to fully oxidised corium and to reduce the oxide density from 8520 kg/m^3 to 5150 kg/m^3, see Fig. 5.3-4.

In terms of melt front progression into the concrete, the calculation indicates that the concrete layer of 50 cm thickness mounted on top of the melt gate is completely ablated at ~16100 s, see Fig. 5.3-3. Before layer inversion, when the axial ablation is governed by the oxidic melt, the ablation rate is steady at ~5.5-7$\cdot$10^{-5} m/s, except for the period of the second melt discharge. The period following layer inversion is characterised by rapid erosion of the remaining 7 cm concrete with an average velocity of ~3.1$\cdot$10^{-4} m/s, due to its interaction with initially superheated metallic melt.
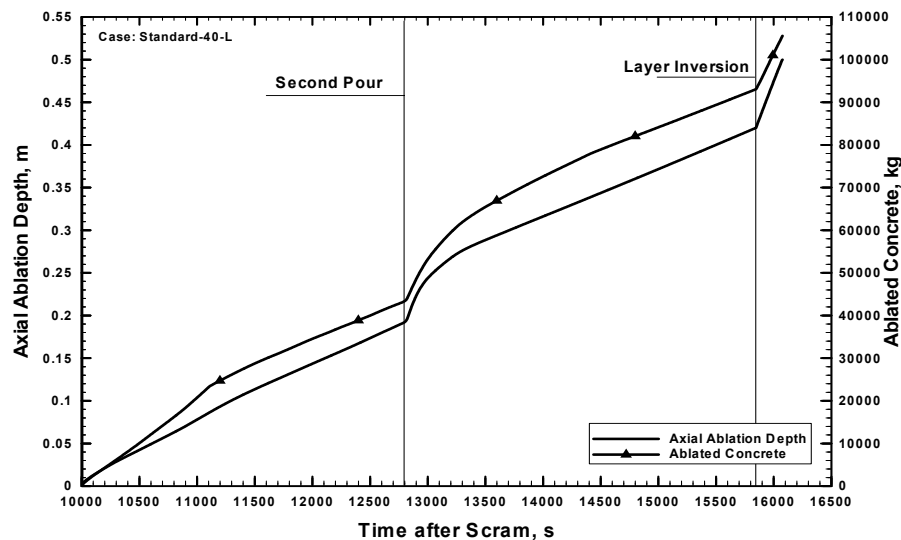

Fig. 5.3-3: Axial ablation depth and total mass of ablated concrete

Such high erosion rate is typical for the transient phase of an MCCI involving superheated metallic melt, as was experimentally observed e.g. in the CORESA-tests, see Fig. 3.6-1.

The ablated mass of concrete amounts to ~105 Mg. In contrast to an unconfined MCCI in existing plants, the amount of concrete which can be ablated during the temporary melt retention is limited to approximately this amount, due to the geometrical constraint of the reactor pit established by the refractory shielding.

Due to continuous dissolution of light concrete decomposition products, the density of the oxidic melt almost steadily declines from 8520 kg/m^3 initially to 6180 kg/m^3 at the time of

layer inversion, see Fig. 5.3-4. The layer inversion further decreases the density to 5200 kg/m^3 due to mixing of the oxidic melt with the light slag layer having a density of 3200 kg/m^3.
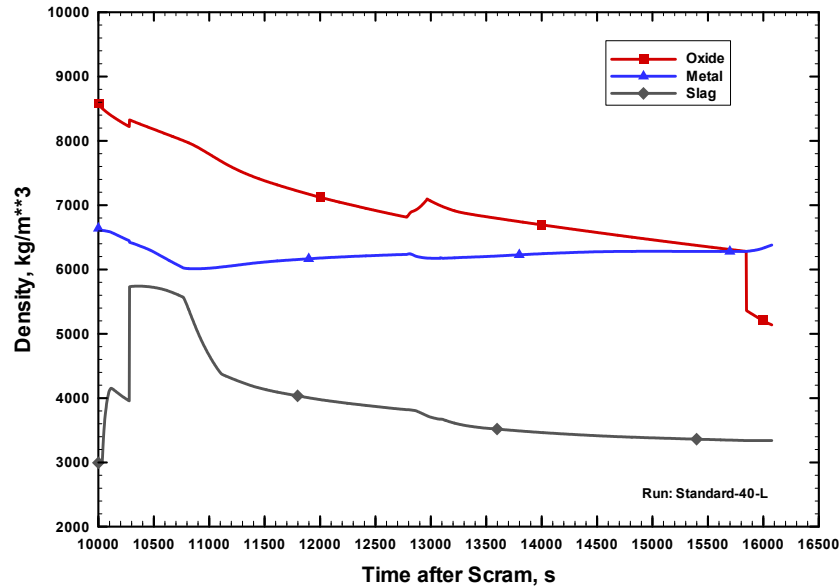

Fig. 5.3-4: *Density of the oxide, metal and slag melt*

Fig. 5.3-5 presents the volumetric solid fraction of the oxidic melt.
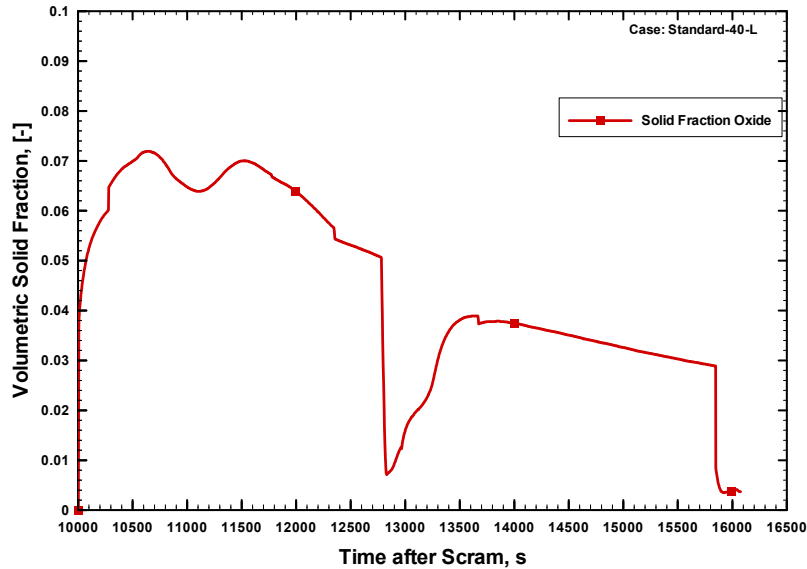

Fig. 5.3-5: *Volumetric solid fraction of the oxidic melt*

In general, the volumetric solid fraction shows a continuous decline over the course of the MCCI from 7% initially to 3% at the time of layer inversion. This behaviour is attributed to the decrease of the melt's surface/volume ratio due to the continuous melt release from the RPV according to Fig. 5.2-1, and a corresponding filling-up of the reactor pit. Therefore, the heat flux, i.e. the decay power related to the melt surface, increases. In response, the solid fraction decreases which is consistent with the findings of the validation of COSACO against the MACE tests.

The continuous decline is disrupted by the second melt discharge at 12780 s which leads to a substantial remelting of solid phases. This effect correlates with the temperature rise occurring at this point which evolves from mixing in-vessel melt with the oxidic melt of the MCCI pool.

The volumetric solid fraction translates into equivalent crust depths at the surfaces of the oxide pool as depicted in Fig. 5.3-6.
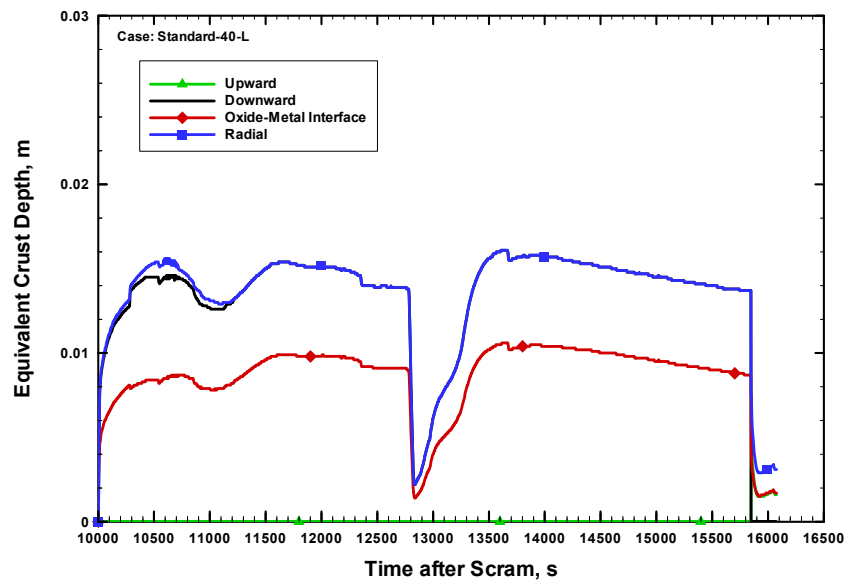

Fig. 5.3-6: *Equivalent crust depth at the heat sinks of the oxidic melt*

The crust depth at the bottom and at the radial oxide/concrete interface remains almost constant at 1.5 cm except for the phase of the second pour. The generally lower crust thickness of ~1 cm at the oxide/metal interface indicates that the heat flux into the metal layer is less than that into the ablating concrete surface. This is attributed to the driving temperature difference which is higher between the melt and the ablating concrete surface than between the oxide and metal layer.

Fig. 5.3-7 depicts the contours of the ablated concrete walls. Clearly visible is the focussing effect induced by the metallic melt. As a result, the metallic melt penetrates faster into the sacrificial concrete than the oxidic melt and thus contacts the refractory shielding significantly before the MCCI in the reactor pit terminates. As the shielding is assumed to be resistant against melt attack, melt front progression stops upon contact.

Practically, the shielding material has to withstand the corresponding thermo-chemical loads following contact with superheated metallic melt. A promising candidate material for such application is ZrO_2, whose stability was extensively evaluated under representative conditions in the CORESA programme. Corresponding tests revealed that the material remained unaffected in the presence of highly superheated metallic melt having a temperature in excess of 2000°C for the entire test duration of ~16 h [Steinwarz 2002].

In this respect, the stability of the refractory shielding is supported by the predicted relatively moderate temperature of the metallic melt of ~1800°C which prevails for almost the entire duration of the temporary melt retention, see Fig. 5.3-1.
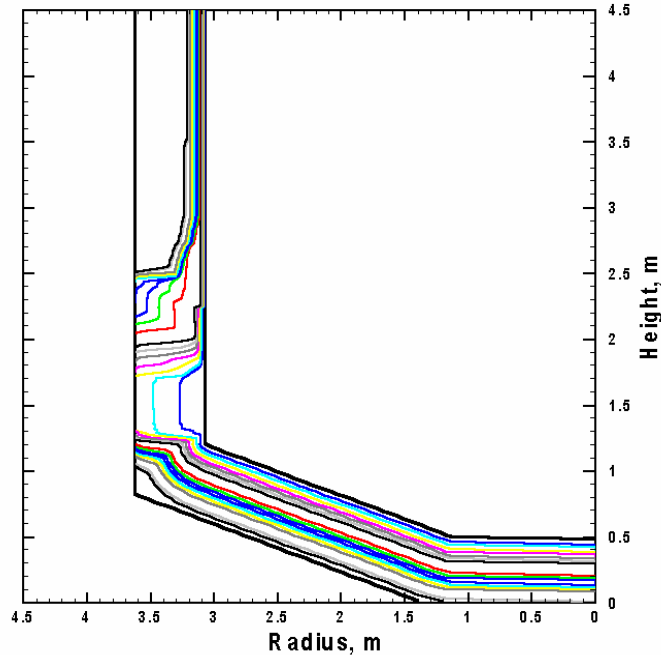
Fig. 5.3-7: *Composite plot of erosion profiles, the contour line acquisition interval is 400 s.*

In conclusion, the results for this case show that the full melt inventory can be collected in the pit with sufficient margin before the melt contacts and opens the gate. The conditions for spreading of the melt are favourable due to the low content of solid phases and the resulting low viscosity at the end of the MCCI.

5.3.2   Accumulation of the core melt inventory in the reactor pit

This chapter presents the results relevant to examining the ability of the reactor pit to accumulate the core melt inventory. Melt accumulation is considered successful, if the in-vessel core melt inventory can be collected in the reactor pit sufficiently before the MCCI pool attains contact with the melt gate. Therefore, it is essential to evaluate the melt front progression into the concrete in axial direction relative to the failure of the RPV-bottom which corresponds to the discharge of the residual in-vessel melt inventory into the reactor pit.

Fig. 5.3-8 compares the axial ablation depth vs. interaction time for the melt accumulation cases executed in the layered mode with the reference case of melt conditioning, Standard 40-L.

Relative to this, Fig. 5.3-8 also depicts the results obtained for the melt accumulation cases conducted in the mixed mode, i.e. 80%E-M and 80%L-M, to demonstrate the influence of postulated mixing of the oxidic and metallic melt on the melt accumulation characteristics of the reactor pit.
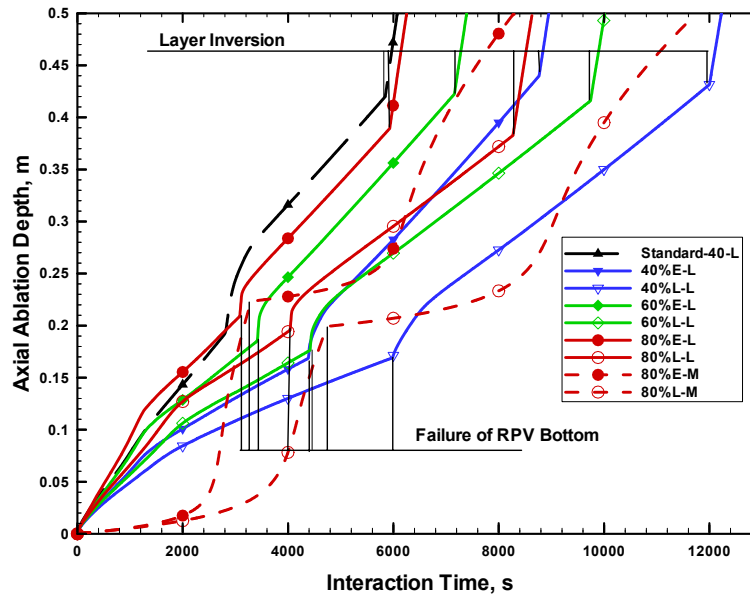
Fig. 5.3-8: Composite plot of ablation front histories in axial direction

As the most important result, the analysis predicts a failure of the RPV-bottom before the melt reaches the melt gate for all cases, despite substantial differences in the melt-concrete interaction time. The latter is attributed to the variation of the melt decay heat level and of melt initial mass in the pit.

In terms of influence of decay heat, the duration of the temporary melt retention evolving from a low power scenario is ~35% longer compared to a high power scenario for equal amounts of initial melt. This correlates well with the decrease of decay power by ~34% when the onset of melt retention is shifted from 3 h to 24 h.

The initial amount of melt affects the duration of the temporary melt retention in so far, as an increasing mass results in decreasing the surface/volume ratio and thus in increasing the power density at the melt/concrete interface. In particular, the analysis yields 3100 s and 4400 s for the cases 80%E-L and 40%E-L, respectively, to achieve failure of the RPV-bottom. These durations were obtained for initial melt-wetted concrete surfaces of 43.5 m^2 for the case 80%E-L and 33.5 m^2 for the case 40%E-L. The ratio of 0.7 between the obtained durations approximately corresponds to the inverse of the ratio between the initial surfaces, i.e. 0.77.

The cases conducted in the mixed mode are characterised by an initially low erosion rate due to the initially large fraction of solidified oxide of >90%, see Fig. 5.3-14 which results from mixing of the oxidic melt with comparably cold metallic melt. Consequently, a considerable fraction of the solidified melt must remelt before concrete ablation rate can speed up. In contrast to the corresponding layered mode cases, this effect prolongs the MCCI. Despite this predicted increase, failure of the RPV-bottom takes place at about the same erosion depths as for the corresponding layered cases 80%E-L and 80%L-L. Remarkably, a comparison between the entire set of cases yields the same result, independent of the predicted considerable differences in interaction time, see Fig. 5.3-8, due to the different initial melt masses, levels of decay heat and molten pool configurations.

Apparently, as the RPV-bottom and the MCCI pool form a coherent system, achieving the failure criterion and triggering the second melt discharge is a function of erosion depth rather than of interaction time.
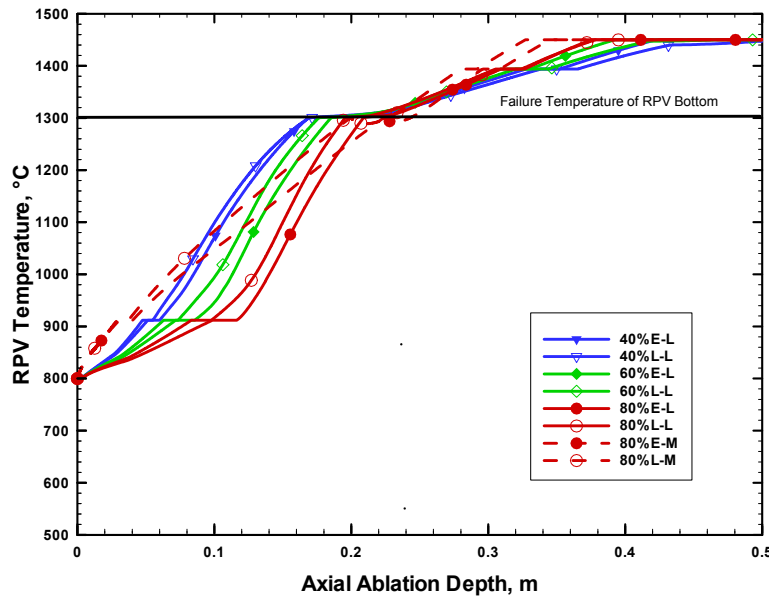

Fig. 5.3-9: *RPV temperature vs. axial ablation depth for all cases specifically examining melt accumulation*

As Fig. 5.3-9 shows, the criterion for failure of the RPV-bottom is achieved at an axial ablation depth between ~18 and 22 cm for all investigated cases. Moreover, for a given initial melt mass, the influence of the actual decay heat level is not significant.

This important result is attributed to the following phenomenon. Failure of the RPV-bottom takes place after it has absorbed a constant amount of energy. The time needed to absorb this amount is governed by the radiant heat flux. Specifically, for a decreasing heat flux as a consequence of a declining decay heat level in the melt, the time to achieve the failure temperature of the RPV-bottom increases. In parallel, the heat flux at the melt/concrete interface also decreases. Due to the isotropic heat flux distribution, both heat fluxes reduce in roughly the same proportion. Therefore, failure of the RPV-bottom always takes place at similar axial ablation depths independent of the actual decay heat level.

Fig. 5.3-10 converts the ablation results presented in Fig. 5.3-8 into safety margins. In the context of melt accumulation, the safety margin relates the residual axial concrete depth at the failure of the RPV-bottom to the overall layer thickness of 50 cm, i.e.

$$SF = \left(1 - \frac{\delta_{Cc,res}^{MG}}{0.5}\right) \cdot 100\% \tag{5.3-1}$$

According to Fig. 5.3-10, the safety margin is in the range from 55% to 65% for all investigated cases. It slightly decreases with increasing amount of melt initially present in the reactor pit, while it gradually increases for late first melt releases. The increase in safety margin is attributed to the decline in ablation rate due to the lower decay heat, which results in

a gradual increase in heat transport in upward direction at the expense of that in downwards direction.

The safety margin obtained for the case Standard-40-L, for which the melt release sequence was calculated with MAAP 4, has a similar value. However, given the uncertainties involved in obtaining the release sequence, this result should be rather regarded as a rough indication than as supplementing evidence.
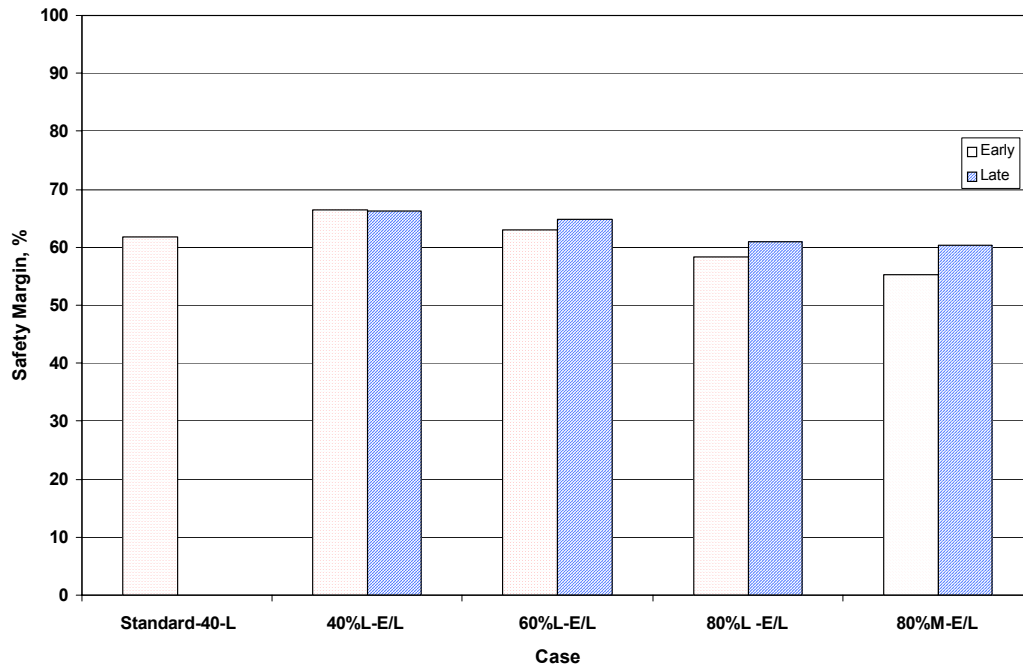

Fig. 5.3-10: *Safety margin of the melt accumulation cases compared with the melt conditioning case Standard-40-L*

In summary, these are high safety margins regarding accumulation of the core melt inventory in the reactor pit. This is especially true if one considers that heating of the RPV-bottom by core melt located in-vessel is considerably underestimated.

The following chapter discusses how the obtained margins translate into homogenisation and conditioning of the melt at the time of spreading.

5.3.3   Melt homogenisation

The unification of melt properties is instrumental for designing and validating the long-term melt stabilisation in the spreading compartment. In this context, the liquidus temperature is of importance, as it influences the temperature level at which the long-term stabilisation takes place. At the same time, it is of equal significance that the melt exhibits characteristics which are favourable for the succeeding spreading transient.

In this manner, this chapter first compares the melt composition at the end of the MCCI which is the essential indicator for the melt characteristics and in particular, the liquidus temperature. However, the liquidus temperature alone is not sufficient to evaluate the spreadability of the melt. Therefore, this chapter additionally examines melt temperature, resulting volumetric solid fraction and the solidification behaviour of the melt.

The properties of the metallic melt are only of secondary importance, since they do not exhibit a significant variation with composition and since there is no potentially negative influence on spreading or long-term stabilisation.
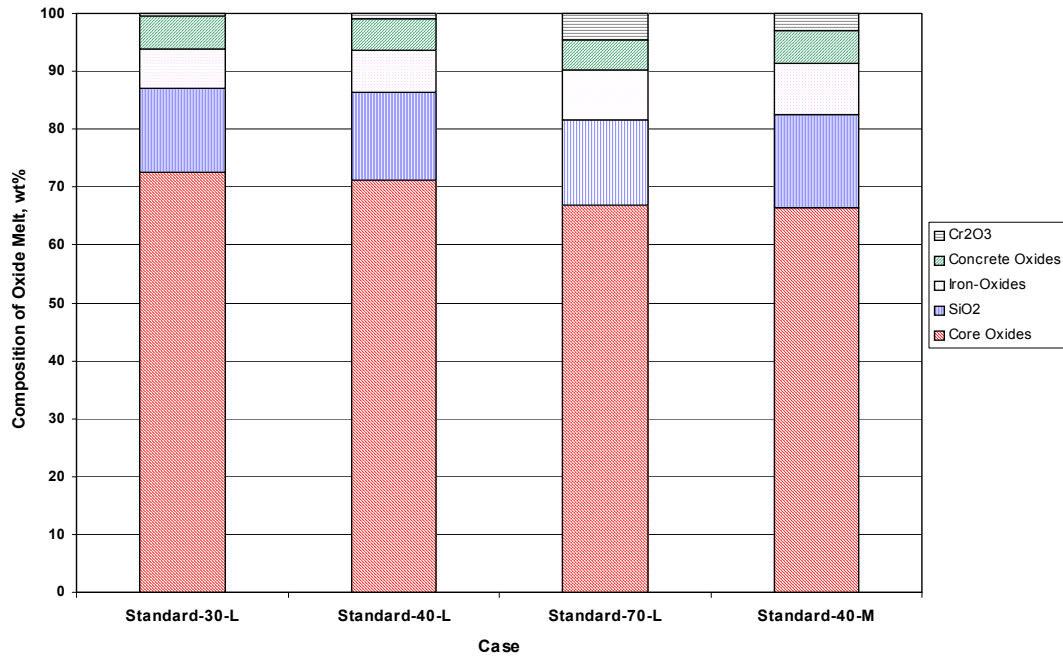

Fig. 5.3-11a: *Composition of the oxidic melt obtained from the cases examining melt conditioning*
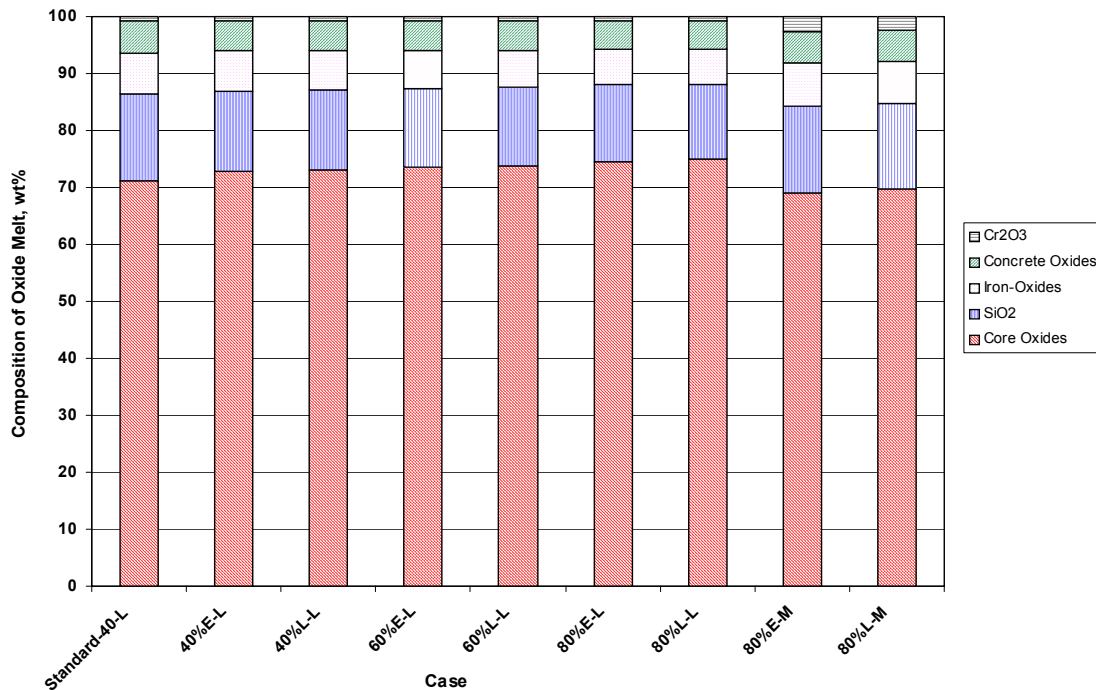

Fig. 5.3-11b: *Composition of the oxidic melt obtained from the cases analysing melt accumulation in comparison with the reference case Standard-40-L. Core Oxides combine UO$_2$ and ZrO$_2$, Concrete oxides Al$_2$O$_3$, CaO, MgO and Iron Oxides FeO and Fe$_2$O$_3$*

Fig. 5.3-11a/b present the melt composition for both, the cases examining melt conditioning and melt accumulation.

The figures show a variation of melt composition with respect to core oxides from ~66-74%, SiO_2 from ~13-16%, iron-oxides from ~6-9% and concrete oxides around ~5.5%. Notably, U and Zr metal are predicted to be completely oxidised for all cases under consideration.

The final content of non-core oxides increases with increasing in-vessel oxidation level due to the initially lower amount of metallic U and Zr in the melt. Conversely, the Cr_2O_3 content rises due to the now larger amount of concrete decomposition products, i.e. Fe_2O_3, H_2O and CO_2, available to oxidise Cr in the metal melt. The increase in non-core oxides in the melt with increasing initial melt mass is attributed to the greater initial volume which expands the melt-wetted interacting concrete surface of the side walls and thus increases the integral amount of concrete ablated during the MCCI sequence.

In conclusion, an adequately homogenised melt composition arises at the end of the MCCI.

Given the melt compositions, the next task is to investigate to what extent the terminal melt states are similar and favourable for melt spreading. To this end, the resulting terminal liquidus temperatures as well as melt temperatures and volumetric fractions are compared on the basis of their time-dependent evolutions to demonstrate the homogenising character of the temporary melt retention.

Fig. 5.3-12a/b show the evolution of liquidus temperature for different melt release sequences, oxide-metal mixing conditions and oxidation levels. In terms of the analyses conducted in the layered mode, the main events disrupting a continuous decline are the second pour leading to a steep increase and the layer inversion which acts in the opposite direction. In contrast, the slope of liquidus temperature is continuously downwards in the mixed mode.

Despite the substantial deviations in evolution, the predicted liquidus temperatures at the termination of temporary melt retention fit into a band of 100 K width for the variation of in-vessel Zr-oxidation, while for the cases investigating melt accumulation, the difference between highest and lowest temperature amounts to ~50 K.

In addition to the low variation the low absolute temperature of ~2050°C at the end of the MCCI, see Figs. 5.3-13a/b, reduces the radiant heat losses to the overlying ambient and the conduction losses into the substrate during the spreading transient. In contrast, spreading of in-vessel melt as given in Tab. 5.2-1, would, dependent on the in-vessel Zr-oxidation level, take place at about 2500°C.
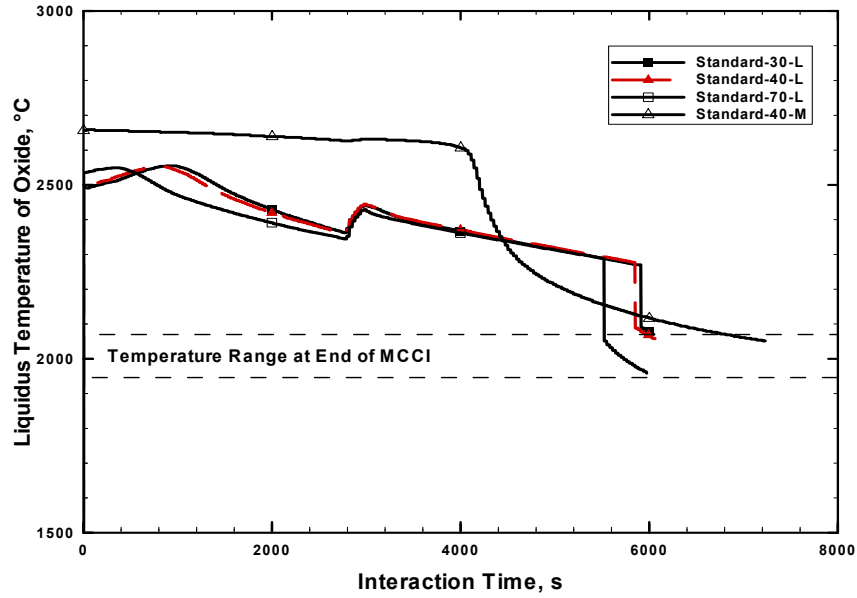
Fig. 5.3-12a: *Liquidus temperature vs. time obtained from the cases examining melt conditioning*
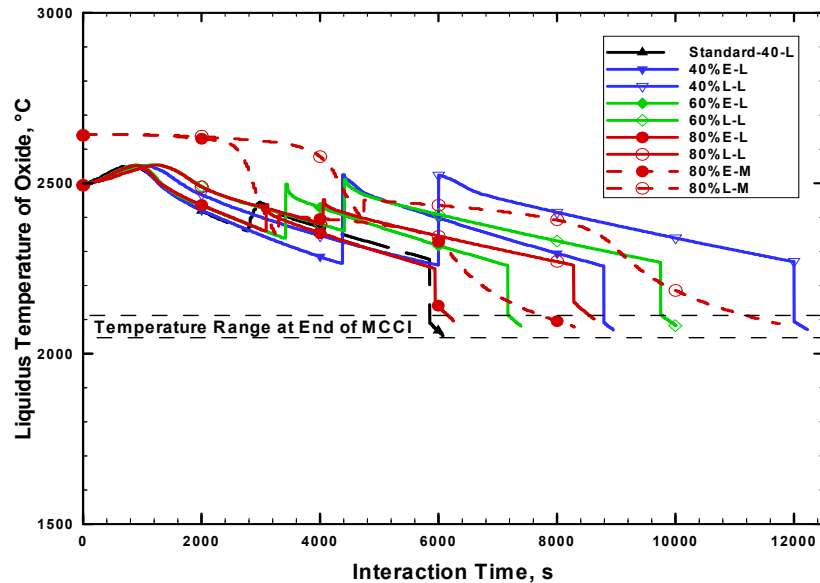
Fig. 5.3-12b: *Liquidus temperature vs. time obtained from the analysis examining melt accumulation in comparison with the results of the reference case Standard-40-L*

The oxidic melt temperatures evolve in parallel with the liquidus temperatures, as a comparison of Figs. 5.3-12a/b and 5.3-13a/b indicates.

The maximum subcooling denoting the temperature reduction relative to the liquidus, is only ~25°C at the end of the MCCI sequence. Such low degree of subcooling points to favourable initial conditions for spreading.
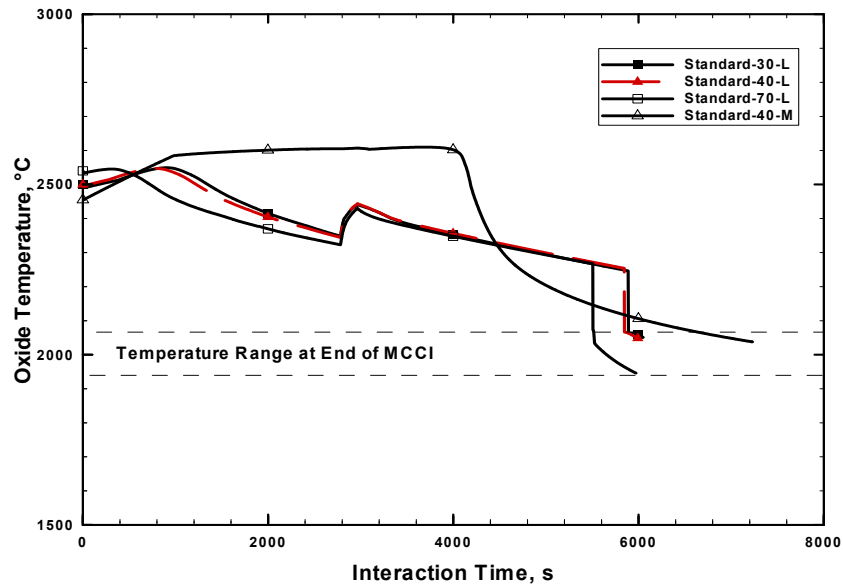
Fig. 5.3-13a: *Temperature of the oxidic melt obtained from the analysis investigating melt conditioning*

Fig. 5.3-13b: *Temperature of the oxidic melt for the cases analysing melt accumulation in comparison with the results of the reference case Standard-40-L*

This indication is reconfirmed by evaluating the volumetric solid fraction which is depicted in Fig. 5.3-14a for the cases investigating melt conditioning and in Fig 5.3-14b for the cases examining melt accumulation. Essentially, the predicted terminal volumetric solid fraction varies between 3-5% for all cases, despite substantial differences arising in the course of the temporary melt retention.

This important result can be explained by the volumetric fraction vs. time for a variation of initial melt mass as shown in Fig. 5.3-14b. As is evident, the volumetric solid fraction arising during the initial phase lasting until failure of the RPV-bottom, decreases with increasing initial melt mass. At the same time, the surface/volume ratio of the melt also decreases in

accordance with the geometrical characteristics of the reactor pit. Therefore, the decay heat which increases with initial melt mass for a given time, distributes over relatively smaller surfaces and hence, higher power densities at the melt surfaces result. In consequence, the volumetric solid fraction decreases which is in accordance with the principal findings of the code validation against the MACE tests.

Fig. 5.3-14a: *Evolution of volumetric solid fraction of the oxidic melt obtained from the cases investigating melt conditioning*
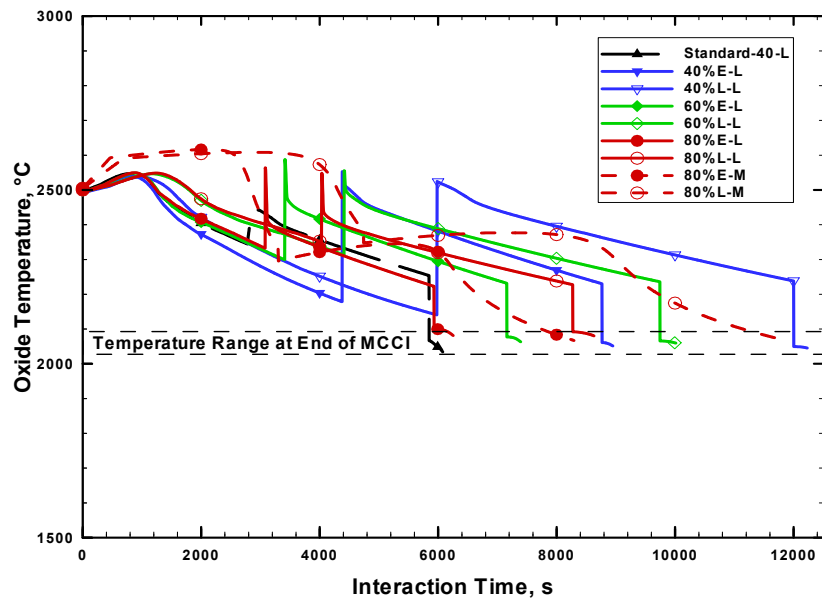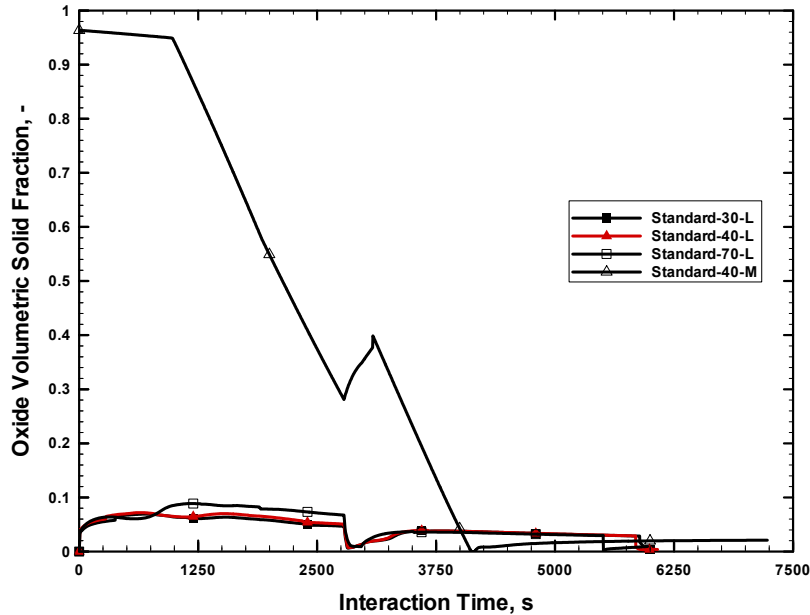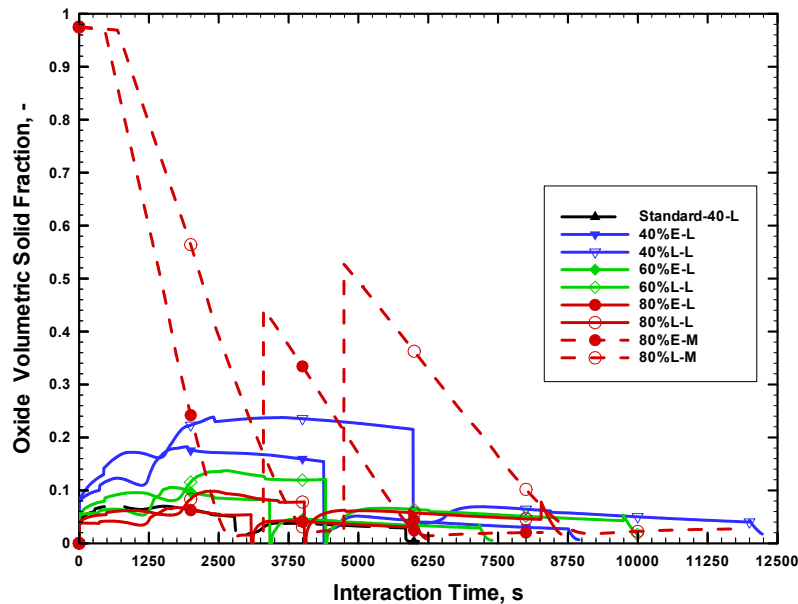

Fig. 5.3-14b: *Evolution of volumetric solid fraction of the oxidic melt for the cases examining melt accumulation in comparison with the results obtained for the reference case Standard-40-L*

Since the MCCI in the reactor pit of the EPR is confined to a well-defined geometry due to the refractory shielding, the surface/volume ratio is effectively limited. This constraint translates into almost identical terminal volumetric fractions which only vary with the time-dependent decay heat.

In the mixed mode, the volumetric solid fraction is initially very high but quickly decreases due to melt reheating. The high solid fraction predicted for the incipient phase is attributed to mixing of oxidic in-vessel melt being at ~liquidus temperature with relatively cold metallic melt. The same effect arises whenever a mixture of oxidic corium and metallic melt is discharged into the MCCI pool following failure of the RPV-bottom.

Case	Viscosity, Pa·s
Standard-30-L	0.028
Standard-40-L	0.03
Standard-70-L	0.04
Standard-40-M	0.035
40%E-L	0.029
40%L-L	0.034
60%E-L	0.027
60%L-L	0.03
80%E-L	0.026
80%L-L	0.029
80%E-M	0.03
80%L-M	0.034

Tab. 5.3-1: *Terminal viscosities of the individual oxidic melts as determined with the viscosity model given in Chap. 3.7.3.*

The low volumetric solid fractions result in low viscosities, see Tab. 5.3-1, at the end of the temporary melt retention which is an essential initial condition for a successful spreading transient.

However, the melt may cool down and, consequently, the volumetric fraction may rise during the spreading transient. Therefore, it is instructive to examine the solidification behaviour of the individual terminal melt compositions given in Fig. 5.3-11 to verify that the melt properties are not intolerably diminished during melt spreading.

To this end, Fig. 5.3-15a/b depict the volumetric solid fraction vs. temperature of the individual melt compositions. For comparison, Fig. 5.3-15c shows the volumetric fractions obtained for 30%, 40% and 70% oxidised in-vessel corium. All solid fractions were determined with the COSCHEM database.

The figures indicate that a favourable homogenisation is also achieved in terms of solidification behaviour of the terminal melt compositions. Therefore, the spreading behaviour of the various melts is also similar. In comparison with the solidification behaviour of unconditioned in-vessel corium, the conditioned melts solidify within a much broader range involving a greatly reduced slope of solid fraction vs. temperature. The fundamental advantage of this effect is that it makes the spreading process fairly robust against cooling of the melt. This contrasts to in-vessel melt which only tolerates a low temperature drop during

spreading. Therefore, the temperature at which immobilisation of the melt is expected, is correlated with the melt initial temperature at the beginning of the spreading transient.

The immobilisation criterion developed for viscosity-limited spreading employs the volumetric solid fraction as a function of temperature to determine a threshold value at which the predicted viscosity goes to infinity and thus the melt immobilises. Equivalent to the modelling of concrete decomposition, see Chap. 3.3.2, the threshold value is taken equal to 50%.

As Figs. 5.3-15a/b show, the 50%-criterion is reached in a narrow temperature band for all investigated cases and varies only with the postulate of a mixed or layered melt.

The various melts are predicted to immobilise between 1450°C and 1600°C, while the initial spreading temperature is almost constant at ~2050°C. Thus, the oxidic melt must cool down by ~450°C before immobilisation takes place. In contrast, in-vessel melt does not tolerate any significantcool-down, assuming that this melt escapes from the RPV at liquidus temperature.

Such an allowable temperature drop is favourably high, as a comparison with an EPR-specific spreading analysis by [Wittmaack 2002] indicates. This analysis predicted a termination of the spreading transient involving a complete emptying of the pit and complete coverage of the spreading area within 1 min. The reduction of temperature of the oxidic melt during this time was less than ~50°C.
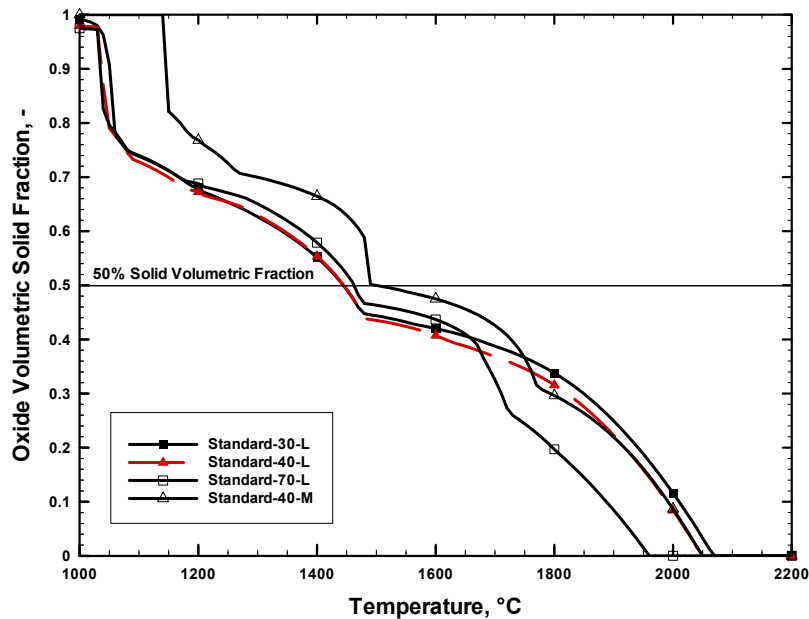
Fig. 5.3-15a: *Volumetric solid fraction vs. temperature of the individual terminal oxide compositions obtained from the cases investigating melt conditioning*
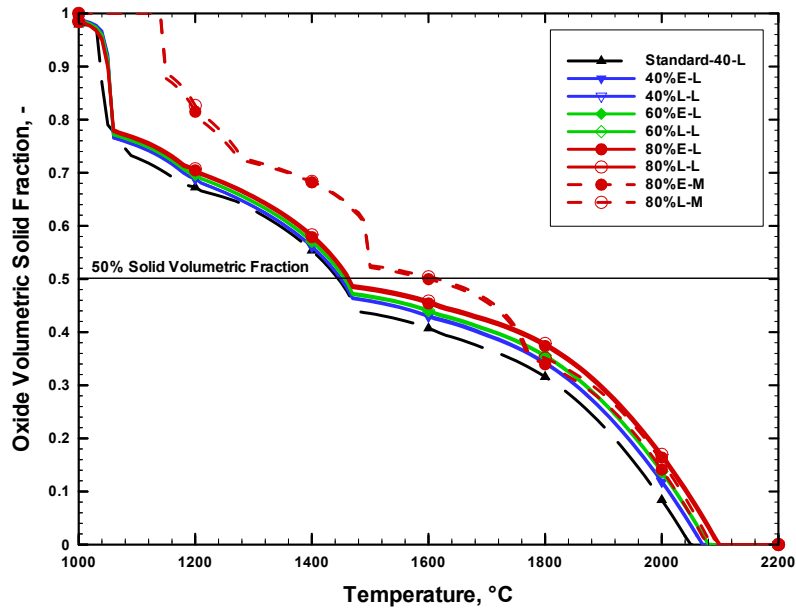
Fig. 5.3-15b: *Volumetric solid fraction vs. temperature of the individual terminal oxide compositions for the cases investigating melt accumulation in comparison with the solidification behaviour of the reference case Standard-40-L*
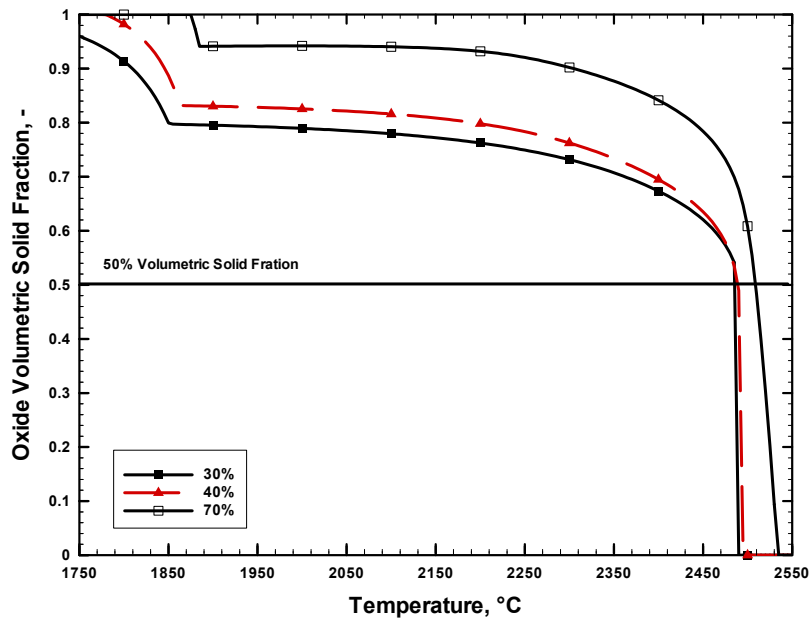
Fig. 5.3-15c: *Volumetric solid fraction vs. temperature of in-vessel corium having oxidation levels of 30, 40 and 70%.*

5.4 Conclusions from the analysis

The analysis of the temporary melt retention shows that the two principal objectives of the reactor pit can be adequately fulfilled independent of the scenario initiating the core melt accident. In particular, the analysis has identified two inherent characteristics as regards melt accumulation as well as melt homogenisation and conditioning for spreading.

In terms of melt accumulation, the specific cylinder-like geometry of the reactor pit leads to self-adjusting characteristics with respect to the duration of the retention period. For decreasing initial amounts of melt in the reactor pit, the surface/volume ratio increases and consequently, the resulting heat flux densities and corresponding ablation rates decrease. This effect extends the time window for accumulating the rest of the melt, whereas it shortens with increasing initial amounts. This consequence is in consistence with the requirements on melt accumulation which reduce with increasing amounts of initial melt and vice versa.

While the outlined self-adjusting characteristics already significantly contribute to a successful melt accumulation, its combination with the effect due to the coherence of the MCCI pool and the RPV reinforces and ultimately ensures it. Specifically, in a thermodynamic sense the RPV, the melted, heat generating core, as well as the surrounding concrete form an adiabatic system. The decay heat either heats the RPV and its internals including the core, or results in decomposition of the surrounding concrete. After being partially released into the pit, the melt forms an MCCI pool which steadily widens in radial and axial direction. The pool reaches the melt gate only after a sufficient amount of decay heat has been provided to ablate the concrete. Based on the following aspects,

(i)   the heat fluxes at the melt/concrete interface and at the free surface of the MCCI pool are similar due to the isotropy induced by the agitation of the melt pool by MCCI gases

(ii)   the radiant heat flux at the free surface is predominantly transferred to the lower head and lower core support plate

it is evident that, at the time the gate is contacted, similar integral amounts of decay heat were used to ablate the concrete and to heat the core support plate and the lower head. However, the energy required for ablating the well-defined amount of concrete is principally higher than that needed to heat the core support plate and lower head to failure temperature. Therefore, these structures always fail and thus release the residual core melt before the melt arrives at the gate. This holds true independent of the actual decay heat level. Therefore, the temporary melt retention functions successfully independent of the scenario initiating the severe accident.

With respect to the effect of failure time, it is instructive to characterise the conditions for achieving an isotropic heat flux distribution. As Fig. 3.6-2 reveals, the deviation from isotropy decreases with superficial gas velocity. In contrast, heat transfer in upward direction is increasingly favoured for decreasing superficial gas velocities. The superficial gas velocity itself closely correlates with the ablation rate, and thus, with the decay heat in the melt. Consequently, for late initial failure times of the RPV corresponding to low decay heat levels, the heat flux distribution favours heat transport in upward direction. As this promotes the heat-up of the lower parts of the reactor pressure vessel at the expense of axial melt front progression, the margins to accumulate the melt further increase.

Another important result concerns the state of the molten pool at the end of the retention phase in the pit. The analysis predicts that the spreadability of the melt is favourable because of the low volumetric solid fraction arising at the time of spreading. Further, the composition

of the melt is predicted to be fairly insensitive towards a change of the investigated parameters such as in-vessel oxidation level, melt release mode and RPV failure time.

These principal findings are attributed to the specific design measures integrated in the reactor pit, which are

(i)   the refractory shielding separating the structural concrete from the sacrificial concrete

(ii)   the melt gate

Both measures restrict the melt front progression in either radial or axial direction and therefore limit the amount of ablatable concrete, which ensures a homogenised melt composition. At the same time, the rigid geometrical boundary also limits the surface/volume ratio of the melt which in turn restricts the volumetric solid fraction.

The characteristic of the temporary retention to yield almost equal melt compositions has a high relevance for verifying the long-term melt stabilisation in the spreading compartment since all the relevant melt properties, like viscosity, solidification behaviour as well as the energy content of the melt at the time of spreading achieve a well-determined state.

Therefore, the use of sacrificial concrete to temporarily retain the core melt in the reactor pit proofs to be an efficient means to decouple the long-term stabilisation measures in the spreading compartment from the inherent uncertainties associated with in-vessel accident progression and failure modes of the RPV.

Chapter 6
Summary

The core melt retention concept of the EPR involves a temporary melt retention in the reactor pit to establish conditions which are well-suited to transfer the core melt from an undefined and uncoolable state into a coolable configuration involving well-defined melt characteristics. The coolable configuration arises after spreading the melt on area of 170 m^2 lateral to the reactor pit.

The principal objectives of the temporary retention are (i) to accumulate the core melt in the case of successive melt releases from the RPV and in parallel (ii) to unify the variety of possible in-vessel melt states and to (iii) condition the melt prior to spreading.

The reactor pit incorporates a layer of specifically developed sacrificial concrete through which the core melt erodes. The stability and thickness of the concrete layer determines the erosion duration and thus the time window to accumulate the melt. The requirements on the concrete are addressed by the concrete composition which consists of iron ore (largely Fe_2O_3) to condition the melt, and of siliceous pebble (largely SiO_2), Portland-cement and water to establish sufficient stability.

The strategy to use concrete as sacrificial material is based on the expectation that the MCCI exhibits self-adjusting characteristics. This means that the velocity of melt front progression into the concrete adjusts to the decay heat level and to the volume/surface ratio of the melt. The effect would be a successful melt accumulation independent of scenario-specific melt release sequences.

At the same time, it is expected that the MCCI yields melt conditions which are favourable regarding melt relocation into the spreading compartment.

These expectations exclusively rested on experimental observations, as the existing models offer only limited ability to quantify above inherent characteristics and moreover, to transfer them to reactor conditions.

Therefore, the computer code COSACO was developed. The fundamentally new philosophy behind the modelling pursued in this code is a consistent description of the thermochemical behaviour and of the heat transfer characteristics of the oxidic melt.

Specifically, the heat transfer modelling of oxidic melt obeys the pertinent characteristics of solidification of multi-component melts as observed in industrial applications, e.g. moulding.

Accordingly, the melt is modelled to predominantly solidify and to deposit as a crust at the cold boundaries of the pool instead of in the volume as was assumed in the existing models. Crust formation commences during the incipient phase of MCCI when the melt temperature falls below the liquidus line.

However, contrary to moulding, the MCCI exhibits a unique phenomenon which is the continuous mixing of the melt pool with relatively cold concrete decomposition products. As a result, solidification also takes place in the volume aside from crust formation at the boundaries of the melt pool. This phenomenon is addressed in COSACO. Correspondingly, solid phases are modelled to stay in the volume, where they increase the viscosity and thus lead to retarding the heat transfer through the melt/crust interface.

The composition of the solid phases reflects to the precipitation characteristics of multi-component systems during cooling. In terms of oxidic core melts, this means that the refractory components UO_2 and ZrO_2 solidify first followed by the lower melting concrete decomposition products. Accordingly, to a first approximation the temperature at the melt/crust interface correlates with the liquidus line.

Eventually, combination of crust-limited heat removal combined with the effect of viscosity increase results in a limitation of heat extraction out of the melt pool already at a high temperature level and therefore effectively restricts cooling of the melt. Even more importantly, the modelling eliminates the need for adjustable parameters due to correlating the solidification behaviour with the heat transfer characteristics. In conclusion, COSACO constitutes a new phenomenological approach to describe the behaviour of MCCI involving oxidic melts.

The model development is accompanied by a detailed evaluation of the thermochemical behaviour of the melt which involves the solidification characteristics as well as chemical reactions that take place during the MCCI. In terms of the EPR, these reactions are predominantly exothermic and thus contribute to the MCCI as an additional heat source. Equally important, they affect melt composition which constitutes a relevant parameter for examining melt unification and conditioning at the time of spreading.

The specific modelling of the thermochemical phenomena addresses the prevailing real solution behaviour of the considered multi-component melts. To this end, the real solution database COSCHEM is implemented into the modelling logic of COSACO employing the implementable equilibrium solver CHEMAPP. The data stored in COSCHEM is essentially based on the real solution database TDBCR 99. This approach enables to determine a consistent thermochemical state of the melt for non-idealised conditions involving all relevant melt components. Accordingly, complex chemical reactions become predictable simultaneously with phase transitions arising following a change of state.

The modelling of the melt pool configuration takes into account two situations. In the case of a stratified configuration, phases having an oxidic character either concentrate in an oxidic or in a slag layer, while the metallic phases accumulate in a metallic layer. These thermochemically immiscible layers are connected by mass and energy transfer. In addition, a mixed model was developed to study the consequences of postulated gas-induced mechanical mixing on the temporary melt retention.

Following the development, COSACO was validated against representative MCCI experiments involving oxidic and metallic melts. In terms of experiments conducted with oxidic melts, the MACE tests M3b and M4 were selected, both of which employed prototypic, UO_2-containing melt. While the melt initial conditions were similar, the tests used different types of concrete, i.e. limestone common sand vs. siliceous and involved different scales and different power levels and histories. Therefore, they are well-suited to support the identification of the expected inherent characteristics involved in the MCCI.

For both tests, the calculated ablation depth was found to be in the range of the local inhomogeneities observed in the experiments which indicates that the calculated heat flux distribution is consistent with that of the experiment. At the same time, the deviation of calculated temperature from the experimental result is generally less than 5% throughout the duration of the test. This result further implies that the prediction is in agreement with the experimental observation that oxidic melts only cool down slightly.

Transferred to the EPR, these results reveal the following:

(i)   COSACO is able to provide adequate predictions of melt front progression into the concrete including the effect of a change of the surface/volume ratio of the melt as well as of the decay heat. The code thus allows to parametrically investigate the consequences of different amounts of melt involved in the initial melt pour. Moreover, the adequacy of COSACO with respect to predicting the heat flux distribution allows to treat the RPV lower head and the MCCI pool underneath as a combined system linked by radiant heat transfer.

(ii)   Due to adequately reproducing absolute melt temperature as well as its corresponding behaviour, COSACO is considered well-suited to predict the thermochemical state of the melt including the volumetric solid fraction. This parameter is of importance as it influences viscosity and thus, the spreading behaviour of the melt.

In terms of tests with metallic melts, the CORESA 2.1 and SURC 4 experiments were employed to validate the code. These tests examined the MCCI characteristics for LCS and basaltic concrete in 2D and 1D geometry, respectively. While the CORESA 2.1 test specifically investigated concrete ablation under transient conditions, the SURC 4 experiment involved metallic Zr to study the general response of the MCCI. The deviation between predicted and measured temperature ranges from 5-10% for both tests. Equivalent to the tests conducted with oxide melts, the calculated course of ablation depth is in the range of the local variations that arose during the experimental conduct.

In conclusion, the validation results suggest that COSACO is appropriate to evaluate the temporary melt retention in the reactor pit.

The strategy for examining the temporary melt retention is decoupled from specific scenario-dependent melt release sequences. The idea behind is to demonstrate that the temporary melt retention works independent of the scenario initiating the severe accident.

In this manner, a generalised sequence of melt release from the RPV is modelled which correlates with the MCCI in the reactor pit. Specifically, a parametric variation of the melt mass initially poured into the reactor pit and of the onset of the MCCI is conducted to identify

and to demonstrate the effect of the self-adjusting characteristics and to address the effect of varying decay heat on the temporary melt retention. In parallel, modelling of the release sequence takes into account the inherent characteristic of the MCCI pool in the reactor pit to establish a coherent system with the bottom structures of the RPV due to exchange of radiant heat. Consequently, these structures are not only heated by the melt located inside, but also from the outside by thermal radiation. Both contributions lead to integral failure of the lower structures after exceeding a criterion based on the ultimate strength of the RPV steel as a function of temperature. The thermo-mechanical failure triggers the second melt pour which results in discharging the residual in-vessel melt into the reactor pit and which completes melt accumulation.

Examination of the analyses shows that independent of whether 40% or 80% of the total melt mass initially discharge into the reactor pit, failure of the lower structures of the RPV takes place at almost identical ablation depths, though these depths are reached after significantly different times. In particular, the second pour results at times at which the residual thickness of the concrete layer on top of the melt gate still amounts to about 50% of the initial value.

This important result is attributed to the combined effect of the self-adjusting characteristics and heating of the lower structures of the RPV. The ablation front progression decreases with decreasing melt mass and with decreasing decay heat and thus determines the duration of melt retention. On the other hand, in order to contact the melt gate, the energy required to ablate the fixed amount of concrete placed on top remains identical. Equivalently, the energy which must be incorporated in the lower structures of the RPV to achieve failure is also constant. The nearly isotropic heat flux distribution along the boundaries of the pool including the melt free surface results in an approximately constant ratio between ablation rate and heating rate of the lower structures of the RPV independent of initial mass and level of decay heat. Therefore, the second pour takes place in a narrow band with respect to ablation depth, while it involves a significant spread with respect to retention time. Accumulation of the core melt inventory thus functions independent of scenario-specific melt release sequences.

An important prerequisite to appropriately unify and condition the melt characteristics for spreading involves the oxidation of the chemically aggressive metallic core melt components Zr and U, the concentration of which is fairly indeterminate in the core melt. This uncertainty is addressed by a parametric variation of the in-vessel oxidation level within the upper and lower limits of 70% and 30%, respectively. The analyses reveal that due to the highly oxidising characteristics of the concrete aggregates Fe_2O_3 and of SiO_2 towards these components, the concentration of both metals completely vanishes already during the incipient phase of the MCCI sequence. Following oxidation, concrete decomposition products continuously accumulate in the oxide melt. Eventually, almost identical melt compositions and masses at the termination of the temporary melt retention result almost independent of the in-vessel oxidation level and melt release sequence. This unification is attributed to the well-defined geometry, to which the MCCI in the reactor pit is confined by the refractory shielding and by the melt gate. Therefore, the amount of ablatable concrete is fixed. Hence, the energy content, thermal properties and thermochemical characteristics of the melt released into the spreading compartment attain a well-determined state.

Despite a substantial variation involving much higher values during the MCCI, the analyses show that the volumetric solid fraction varies between 3-5% at the end of the temporary melt retention and is thus almost independent of the melt's initial state and release sequence. These low values are attributed to the geometrical confinement established by the refractory shielding in combination with achieving complete accumulation. The confinement restricts the size of the melt/concrete interface, while a complete melt accumulation results in a low surface/volume ratio compared to the phase when only a part of the melt is present in the pit. Consequently, relatively high power densities arise following complete melt accumulation which yield sufficiently low final volumetric solid fractions and thus low viscosities which imply good initial conditions for melt spreading.

Further, mixing of the oxidic melt with sacrificial concrete widens significantly the solidification range relative to unconditioned in-vessel melt. This effect is highly beneficial with respect to spreading, as it allows a significant cool-down of the melt during the spreading process without approaching critical conditions.

Therefore, the use of sacrificial concrete to temporarily retain the core melt in the reactor pit proofs to be a viable means to unify the variety of possible initial melt states and release sequences from the RPV as an essential prerequisite for a successful long-term melt stabilisation.

Chapter 7
Literature

[Adroguer 1999]

Adroguer, B. et al., '*Corium Interactions and Themochemistry*',FISA 99 EU research in reactor safety, Luxembourg, 29.11-1.12.1999 EUR 19532 EN

[Ahn 1999]

Ahn, K.I., Kim. D.H., Kim, S.B., Kim, H.D., '*A comparative study on the reactor lower head models employed in the current severe accident computer codes*', Proceedings of the NURETH 9 Conference, San Francisco, Ca., October 3-8, 1999

[Allison 1993]

Allison, C.M. et al., '*SCDAP/RELAP5/Mod3.1 Code Manual, Volume II: Damage Progression Model Theory*', Technical Report NUREG/CR-6150 USA, 1993

[Alsmeyer 1992]

Alsmeyer, H. et al., '*Beta Experiments on Zirconium Oxidation and Aerosol Release during Melt-Concrete Interaction*', Proc. Second OECD CSNI Specialist Meeting on Molten Core Debris-Concrete Interactions, Karlsruhe 1992, KfK 5108, NEA/CSNI/R(92)10

[Artnik 1995]

Artnik, J., F. Funke., F. Kretzschmar, H. Schmidt, '*Machbarkeitsuntersuchung zur Außenkühlung des Reaktordruckbehälters bei schweren Störfällen mit Kernzerstörung an einem innovativen Siedewasserreaktor mittlerer Leistung*', Abschlußbericht, BMFT 15NU0949, 1995

[Artnik 1996]

Artnik, J., Caroli, C., Cenerino, G.; Parozzi, F., Pini, A., Sairanen, R., Turland, B.D., '*Molten pool behavior calculations for reactor cases*', Proceedings of the FISA 95 EU research on severe accidents, EUR16896

[Azarian 1999]

Azarian, G., '*Personal communication with G. Azarian, Framatome Paris*', Spring 1999, Also published in Nie, M., '*Application of sacrificial concrete for the retention and*

conditioning of molten corium in the EPR core melt retention concept', Proceedings of the OECD Workshop on Ex-vessel Debris coolability, Karlsruhe 15.-18. November 1999. FZKA 6475, Mai 2000

[Bargel 1988]
Bargel, H.-J., Schulze, G., *'Werkstoffkunde'*, VDI-Verlag GmbH, Düsseldorf, 1988

[Bhansali 1987]
Bhansali, A.S., A.K. Mallik, '*CALPHAD 11'*, 1987 (105)

[Biloni 1996]
Biloni, H. Boettinger, W.J., *'Solidification'*, in R.W. Cahn, P. Haasen, Physical Metallurgy, Volume 1, North Holland, 1996

[Bittermann 2001]
Bittermann, D., Krugmann, K., Azarian, G., *'EPR accident scenarios and provisions'*, Nuclear Engineering and Design 207 (2001) pp. 49-57

[Blottner 1979]
Blottner, F.G., *'Hydrodynamics and Heat Transfer Characteristics of liquid Pools with Bubble Agitation'*, NUREG/CR-0944, SAND79 1132, 1979

[Bonnet 1999]
Bonnet, J.M., *'Thermal hydraulic phenomena in coirum pools for ex-vessel situations: The BALI experiment'*,Proceedings of the OECD Workshop on Ex-Vessel Debris Coolability, Karlsruhe, Germany, 15-18 November, 1999, FZKA 6475

[Brandes 1983]
Brandes, E.A., Ed., *'Smithells Metals Reference Book'*, 6th Edition, Butterworths 1983

[Brettschuh 2001]
Brettschuh, W., '*The SWR 1000: A nuclear power plant concept with boiling water reactor for maximum safety and economy of opertation*', Proceedings ICONE 9, Nice 2001

[Chavez 1994]
Chavez, S.A., Korth, G.E., Harper, D.M., *'High temperature tensile and creep data for Inconel 600, 304 stainless steel and SA 106B carbon steel'*, Nuclear Engineering and Design 148 (1994) 351-363

[Cheynet 1992]
Cheynet, B., Barbier, J.N., Chevalier, P.Y., Rivet, A., Fischer, E., '*GEMINI: Gibbs Energy MINImizer for complex equilibria determination*', CALPHAD XXI, Jerusalem, Israel, June 14-19 1992, Calphad 16 (4) 339, 1992.

[Chevalier 1999]
Chevalier, P.Y.,*'TDBIV - TDBCR - Thermodynamic Databases for Nuclear Chemistry – Documentation'* ,EU 4th Framework Programme INV-CIT(99)-P039, September 1999

[Cognet 1998]
Cognet, G., Gandrille, P., '*In-vessel core melt retention by RPV outside cooling for high power PWR. MAAP 4 analysis on a LBLOCA scenario without SI'*, Proceedings Workshop on

In-Vessel Core Debris Retention and Coolability, Garching, Germany, March 3-6 1998, Nuclear Safety NEA/CSNI/R(98)/18

[Cole 1984]
Cole Jr, R.K. et al, '*CORCON-Mod2: A Computer Program for Analysis of Molten Core Concrete Interactions*', NUREG/CR-3920, SAND 84-1246, August 1984

[Copus 1989]
Copus, E. R. et al., '*Core-Concrete Interactions using molten steel with Zirconium on a basaltic basemat: The SURC-4 Experiment*', Sandia National Laboratories, NUREG/CR-4994, SAND90-1022, Apr. 1989

[Copus 1992]
Copus, E.R., Blose, R.E., Brockmann, J.E., Simpson, R.B., Lucero, D.A., '*Core Concrete Interactions Using Molten Urania With Zirconium on a Limestone Concrete Basemat – The SURC 1 Experiment*', NUREG/CR-5443 Sand90-0087, 1992

[Dantzig 1999]
Dantzig, J.A., 'Modeling Solidification Processes using FIDAP', Cryst. Res. Tochnol. 34, 1999, pp. 417-424

[Dinsdale 1991]
Dinsdale, A.T., '*SGTE data for pure elements*', Calphad, 15, Vol. 4, pp. 317-325, 1991

[Eppinger 2001]
Eppinger, B. et al., '*Simulationsexperimente zum Ausbreitverhalten von Kernschmelzen: KATS-8 bis KATS-17*', Forschungszentrum Karlsruhe, FZKA 6589, März 2001

[Eriksson 1990]
Eriksson, G., Hack, K, '*Chemsage - A computer program for the calculation of complex chemical equilibria*', Metallurgical Transactions B, Vol. 21B, Dec. 1990

[Farmer 1990]
Farmer, M.T. et al, '*Corquench: A Model for Gas Sparging-enhanced, Melt-Water, Film-Boiling Heat Transfer*', ANS Winter Meeting on the thermal Hydraulics of Severe Accidents, Washington D.C., November 1990

[Farmer 1992]
Farmer, M.T., Spencer, B.W., Armstrong, D.R., *'MACE Test M1B Data Report'* Reactor Engineering Division, Argonne National Laboratory, ACE-TR-D6

[Farmer 1997]
Farmer, M.T. et al, '*Mace Test M3b Data Report Volume 1*', MACE-TR-D13, EPRI TR-108806, November 1997

[Farmer 1999]
Farmer, M.T. et al, '*Mace Test M4 Data Report*', MACE-TR-D16, August 1999

[Farmer 1999a]
Farmer, M.T., Spencer, B.W., Aeschlimann, R.W. *'Liquidus/Solidus and Zr Solubility Measurements for PWR and BWR Core Melt Compositions'*, Proceedings of the OECD Workshop on Ex-Vessel Debris Coolability, Karlsruhe, Germany, 15-18 November, 1999, FZKA 6475

[Firnhaber 1992]
Firnhaber, M., Alsmeyer, M., '*BETA V5.1 Experiment on melt concrete Interaction – Comparison Report*', OECD NEA NEA/CSNI/R(92)9, April 1992

[Fischer 2002]
Fischer, M., Hellmann, S., Nie, M., *'Experimentelle Untersuchungen zur Wechselwirkung von Corium-Schmelzen mit Schutz- und Opferschichten (CORESA)'*, Abschlußbericht Vorhabens-Nr. 1501211, Berichts-Nr. NGES4/2002/de/0187A, Oktober 2002

[Fischer 2003]
Fischer, M., *'Severe accident mitigation and core melt retention in the European Pressurized Reactor (EPR)'* Proceedings 11th International Conference on Nuclear Engineering, ICONE 11, Tokyo, Japan, April 20-23 2003

[Flemings 1974]
Flemings, M.C., '*Solidification Processing*', Mc-Graw-Hill Series in Materials Science and Engineering, 1974

[Foit 1995]
Foit, J.J. et al., *'The Wechsl-Mod3 Code: A Computer Program for the Interaction of a Core Melt with Concrete includiong the long Term Behavior'*, FZKA 5522, February 1995

[Foit 1995a]
Foit, J.J., Miassoedov, A., *'Modeling of Viscosity and Heat Transfer of Complex Oxidic Melts in WECHSL'*, Forschungszentrum Karlsruhe, Wissenschaftliche Berichte FZKA 5507

[Frohberg 1994]
Frohberg, M., *'Thermodynamik für Werkstoffingenieure und Metallurgen* 'Deutscher Verlag für Grundstoffindustrie, Leipzig Stuttgart 1994

[Gauntt 1998]
Gauntt, R.O., Cole, R.K. et al., *'MELCOR Computer Code Manuals'*, NUREG/CR6119, Sandia National Laboratoy, USA, 1998

[GTT 1999]
GTT-Technologies, *'CHEMAPP – The thermochemistry library for your software*', GTT-Technologies, Herzogenrath, Germany, 1996-1999

[Häfner 2001]
Häfner, W., '*Experimentelle Untersuchungen von Corium-Schmelzen mit Schutz- und Opferschichten (CORESA)'*, Abschlussbericht Projekt-Nr. 1501210, Berichts-Nr. BF-40.092-8, Oktober 2001

[Hohorst 1990]
SCDAP/RELAP Mod2 Code, Volume 4: *MATPRO - a Library of Material Properties for Light Water Reactor Accident Analysis*, NUREG/CR-5273, Vol. 4, Feb. 1990

[Horvath 1970]
Horváth, A., 'Physikalisch-*Chemische Berechnungen in der Metallurgie'*, Akadémiai Kiadó, Verlag der Ungarischen Akademie der Wissenschaften, Budapest 1970.

[IAEA 1995]
IAEA, *'Design and Development Status of Small and Medium Reactor Systems 1995'*, IAEA TECDOC-881

[Kutateladze 1978]
Kutateladze, S.S., Malenkow, I.G., *'Boiling and Bubbling Heat Transfer under the conditions of free and forced convection'*, 6th Int. Heat Transfer Conference, Toronto 1978

[Lafarge 2001]
Lafarge aluminates, *'Technical Data Sheet of SECAR 71'*, www.lcainc.com

[Levin 1975]
Levin, E.M., McMurdie, H.F., *'Phase Diagrams for Ceramists'*, The American Ceramic Society, 1975

[MAAP 1994]
MAAP 4, *'Modular Accident Analysis Program for LWR plants'*, Code Manual Vols. 1-4, Prepared by Fauske & Associates, Inc., Burr Ridge, IL, USA, May 1994

[Marsh 1980]
B. D. Marsh,'*On the Crystallinity, Probability of Occurrence, and Rheology of Lava and Magma'*, Contrib. Mineral. Petrol. 78 (85-98) 1981.

[Peehs 1979]
Peehs, M., Skokan, A., Reimann, M., '*The Behavior of Concrete in Contact with Molten Corium in the Case of a Hypothetical Core Melt Accident'*, Nuclear Technology **46**, pp. 192-198, 1979

[Ramaciotti 1999]
Ramaciotti, M., '*Étude du Comportement Rhéologique de Mélanges issus de l'Interaction Corium/Béton',* Thèse Docteur de l'Université de Provence (Aix-Marseille I), 24. Septembre 1999

[Roche 1994]
Roche, M.F., Steidl, D.V., Leibowitz, L., Fink, J.K., Sehgal, B.R., *'Viscosity of Corium Concrete Mixtures at High Temperatures'*, ACE-TR-C37, February 1994

[Rohsenow 1973]
Rohsenow, W.M., Hartnett, J.P.,'*Handbook of Heat Transfer'*, McGraw-Hill Book Company, 1973

[Schäffler 1986]
Schäffler, H., '*Baustoffkunde*', Vogel-Fachbuch, Kamprath-Reihe Technik, 4., überarbeitete Auflage, Würzburg, 1986

[Scheil 1942]
Scheil, E., '*Z. Metallk.*', <u>34</u>, pp 70, 1942

[Schulz 1975]
Schulz, B. '*Thermal conductivity of composites*', Proceedings of the International Conference on Composite Materials, Vol. 2., 1975

[Sehgal 1999]
Sehgal, B.R., Nourgaliev, R.R., Dinh, T.N., '*Characterization of heat transfer processes in a melt pool convection and vessel-creep experiment*', Proceedings of the NURETH 9 Conference, San Francisco, Ca., October 3-8, 1999

[Seiler 1996]
Seiler, J.M., '*Phase Segregation Model and molten Pool Thermal-Hydraulics during Core-Concrete Interaction*', Nuclear Engineering and Design 166 (1996) pp 256-267

[Senski 2002]
Senski, G. '*Personal communication to G. Senski, Erlangen, June 2002*', Data obtained from experiments investigating the ultimate strength of RPV-steel at high temperatures'. Documented in '*Haubner, Keim, 'Hochtemperatur-Zugversuche am 20 MnMoNi 5 5*' Siemens Versuchsbericht KWU S 512/92/063, Dezember 1992

[Spencer 1991]
B.W. Spencer, et al., '*MACE Scoping Test*' ,MACE-TR-D03; Argonne Nat. Lab., June 1991

[Stedman 1990]
Stedman, S.J., Evans, J.R.G., Woodthorpe, J., '*Rheology of composite ceramic injection moulding suspensions*', Journal of Material Science, <u>25</u>, pp. 1833-1841, 1990

[Steinberner 1978]
Steinberner, U., Reineke, H.-H., '*Turbulent Buoyancy Convection Heat Transfer with Internal Sources*', Proceedings Sixth International Heat Transfer Conference, Toronto, Canada, August 1978

[Steinwarz 1999]
Steinwarz, W.; Häfner, W.; Alkan, Z.; Fischer, M., '*Großexperimente mit repräsentativer Kernschmelze im Hinblick auf die Beherrschung eines Kernschmelzunfalls*'; Atomwirtschaft (atw), Heft 07, Juli 1999

[Steinwarz 1999a]
Steinwarz, W., et al., '*Investigations on the phenomenology of ex-vessel core melt behavior*', project final report, European Commission, 4th Framework programme on nuclear fission safety, EXV-COMAS(99)-D27, October 1999

[Steinwarz 2002]
Steinwarz, W., Koller, W., Dyllong, N., *'Experimentelle Untersuchungen zur Wechselwirkung von Corium-Schmelzen mit Schutz- und Opferschichten (CORESA)'*, Abschlußbericht Vorhabens-Nr. 1501212, Berichts-Nr. SNT-AB-2002-01, Februar 2002

[Szekely 1963]
Szekely, J, *'Mathmatical Model for Heat or Mass Transfer at the bubble-stirrred Interface of two immiscible Liquids'*, Int. J. Heat and Mass Transfer, Vol. 6, pp. 417-422, 1963

[Theofanous 1995]
T.G. Theofanous, C. Liu, S. Additon, S. Angelini, O. Kymäläinen, T. Salmass, *'in-vessel coolability and retention of a core melt'*, DOE/ID-10460, Vol. 2, Juli 1995 (Draft)

[Theofanus 1997]
Theofanus, T.G., Yuen, W.W., Angelini, S., Sienicki, J.J., Freeman, K., Chen, X., Salmassi, T., *'Lower Head Integrity Under Steam Explosion Loads'*, JAERI-Conf 97-011

[Thinnes 1994]
Thinnes, G.L., Korth, G.E. Chavez, S.A., *'High temperature creep and tensile data for pressure vessel steels SA533B1 and SA508-Cl2'*. Nuclear Engineering and Design 148 (1994) 343-350

[Thompson 1997]
D.G. Thompson, et al., *'Compilation, analysis and Interpretation of ACE Phase C and MACE experimental data – MCCI Thermohydraulic results'* ACEX TR-C-14, Vol. 1; Argonne Nat. Lab. Nov. 1997

[Urbain 1987]
Urbain, G., *'Viscosity Estimation of Slags'*, Steel Research Vol. 58, pp. 111-116, 1987

[VDI 1984]
VDI, *'VDI-Wärmeatlas, Berechnungsblätter für den Wärmeübergang'*, VDI-Verlag GmbH, Düsseldorf, 1984

[Wallis 1969]
Wallis, G.B., *'One-dimensional two phase flow'*, Mc Graw-Hill Book Company, 1979

[Wittmaack 2002]
Wittmaack, R., *'Simulation of free-surface flows with heat transfer and phase transitions and application to corium spreading in the EPR'*, Nuclear Technology, Vol. 137 March 2002, pp. 94-212

[Wülfrath 1999]
Wüfrath Refractories, *'Technical Product Information on fired Magnesia Bricks Type PERMAG B80S'*, 24.09.1999, Wülfrath Refractories GmbH, Hilden (Germany)

[Wülfrath 2000]
Wülfrath, *'Personal communication with Wülfrather Feuerfest und Dolomitwerke GmbH & Co. KG'*, January 2000